5-2010

# GRAIN BOUNDARY PREMELTING AND ACTIVATED SINTERING IN BINARY REFRACTORY ALLOYS

Xiaomeng Shi
*Clemson University*, xshi@clemson.edu

# GRAIN BOUNDARY PREMELTING AND ACTIVATED SINTERING IN BINARY REFRACTORY ALLOYS

---

A Dissertation
Presented to
the Graduate School of
Clemson University

---

In Partial Fulfillment
of the Requirements for the Degree
Doctor of Philosophy
Materials Science and Engineering

---

by
Xiaomeng Shi
May 2010

---

Accepted by:
Dr. Jian Luo, Committee Chair
Dr. Eric Skaar
Dr. Igor Luzinov
Dr. Konstantin Kornev

# ABSTRACT

Quasi-liquid intergranular film (IGF) which has been widely observed in ceramic systems can persist into sub-solidus region whereby an analogy to Grain boundary (GB) premelting can be made.

In this work, a grain boundary (GB) premelting/prewetting model in a metallic system was firstly built based on the Benedictus' model and computational thermodynamics, predicting that GB disordering can start at 60-85% of the bulk solidus temperatures in selected systems. This model quantitatively explains the long-standing mystery of subsolidus activated sintering in W-Pd, W-Ni, W-Co, W-Fe and W-Cu, and it has broad applications for understanding GB-controlled transport kinetics and physical properties. Furthermore, this study demonstrates the necessity of developing GB phase diagrams as a tool for materials design.

Subsequently, Grain boundary (GB) wetting and prewetting in Ni-doped Mo are systematically evaluated via characterizing well-quenched specimens and thermodynamic modeling. In contrast to prior reports, the δ-NiMo phase does not wet Mo GBs in the solid state. In the solid-liquid two-phase region, the Ni-rich liquid wets Mo GBs completely. Furthermore, high-resolution transmission electron microscopy demonstrates that nanometer-thick quasi-liquid IGFs persist at GBs into the single-phase region where the bulk liquid phase is no longer stable; this is interpreted as a case of GB prewetting. An analytical thermodynamic model is developed and validated, and this model can be extended to other systems.

Furthermore, the analytical model was refined based upon Beneditus' model with correction in determining interaction contribution of interfacial energy. A calculation-based GB phase diagram for Ni-Mo binary system was created and validated by comparing with GB diffusivities determined through a series of controlled sintering experiments. The dependence of GB diffusivity on doping level and temperature was examined and compared with model-predicted GB phase diagram. The consistency between GB phase diagram and GB diffusivity was evidently observed.

This study revealed the existence of quasi-liquid IGF in Ni-Mo and re-confirmed our prior hypothesis proposed through work in Ni-W system. It also demonstrated further the necessity of a GB phase diagram as a new tool to guide the materials processing or design, such as selection of sintering aid and heat-treatment.

# DEDICATION

I dedicate this work to my wife and my family member, Mom, Dad and Grandma, in appreciation of their love, support and encouragement.

# ACKNOWLEDGEMENTS

I would like to take this opportunity to thank all the people who made this dissertation possible.

First of all, my deepest thanks go out to Dr. Jian Luo, my committee chair and major advisor for his significant support and guidance throughout my Ph. D work. Uncountable meaningful discussions and thorough explanation of my questions lead me to walk out of the cloud of puzzle and approach the goal of this work step by step. From the first step of modeling, initial establishment of quench furnace and SEM/HRTEM operation to building new models and paper drafting, he offered me sincere advice and tremendous encouragement. In addition, in pursuing the GEMS Award, Dr. Luo gave me in-depth education on proposal writing and critical suggestion on oral presentation. I present my true gratitude to Dr. Luo for his advice and help in my Ph. D work.

I am very grateful for the suggestions and inputs from my committee members: Dr. Eric Skaar, Dr. Igor Luzinov and Dr. Konstantin Kornev, from oral exam to pre-defense meeting. Additionally, special thanks go to Dr. JoAn Hudson and Dr. Haijun Qian in EM Lab for teaching me the operation of various EM facilities and Dr. Henry Rack for helping me in TEM specimen preparation. I extend my appreciation to all my group members: Hao Chen, Archana Kayyar and Kaveh Mechinchi Asi, for their help and support.

I also acknowledge Air Force Office of Scientific Research Grant No. FA9550-07-1-0125 in the High Temperature Aerospace Materials program (managed by Dr. Joan Fuller)" for financial support.

TABLE OF CONTENS

Page

Table of Contents (Continued)

Page

Table of Contents (Continued)

Page

Table of Contents (Continued)

Page

Table of Contents (Continued)

Page

LIST OF TABLES

List of Tables (Continued)

Table Page

LIST OF FIGURES

List of Figures (Continued)

Figure Page

List of Figures (Continued)

Figure Page

List of Figures (Continued)

Figure Page

List of Figures (Continued)

Figure Page

List of Figures (Continued)

Figure Page

List of Figures (Continued)

Figure Page

List of Figures (Continued)

Figure Page

# CHPATER ONE

# INTRODUCTION

Grain boundary (GB) or surface premelting in unary systems is a phenomenon whereby nanoscale quasi-liquid or liquid-like interfacial films are thermodynamically stabilized at $T < T_{melting}$. Although the surface premelting has been widely studied [1,2,3], the existence and importance of GB premelting are controversial. In particular, a 1989 hot-stage TEM experiment concluded that GB premelting did not occur until $0.999T_{melting}$ for pure Al [4], which greatly discourage further exploration in this field. However, in multicomponent systems, impurity-based quasi-liquid interfacial films can in principle be stabilized to much greater undercoolings. Somewhat consistently, impurity-based intergranular films (IGFs) have been widely observed in ceramic systems [5]. These quasi-liquid IGFs can be stabilized well below the bulk solidus lines [6], where an analogy to GB premelting can be provoked.

Solid-state (subsolidus) activated sintering refers to the phenomenon whereby the densification rates are significantly enhanced by adding minor impurities (sintering aids) when the temperature is still well below the bulk eutectic/peritectic temperature. The exact mechanism for subsolidus activated sintering remained a mystery for decades. In 1999, a study attributed activated sintering in $Bi_2O_3$-doped ZnO to the enhanced GB transport in quasi-liquid IGFs that are thermodynamically stabilized below the bulk eutectic temperature [6]. More recently, a HRTEM and Auger study in Ni-doped W

system indicated the stabilization of quasi-liquid IGFs well below the bulk eutectic temperature, thereby implying a similar activated sintering mechanism [7].

In a broad sense, these studies on activated sintering suggest that the bulk phase diagrams are inadequate for guiding the selection of sintering aids and recipes (or materials processing and material design in general) because these quasi-liquid IGFs can form well below the bulk solidus line where the bulk liquid phase is not yet stable; nonetheless, these quasi-liquid interfacial films result in subsolidus activated sintering phenomena that are phenomenologically similar to liquid-phase sintering. Furthermore, the formation of such liquid-like GBs (below the bulk solidus line) can also affect the creep, grain growth kinetics, and many other properties of the material [5].

In this thesis study, we have developed a quantitative thermodynamic model for predicting the stability of subsolidus quasi-liquid IGFs in binary metallic systems. We constructed a new kind "GB diagrams" as a new materials science tool for mechanism-informed materials design. We validated our model and computed "GB diagrams" via HRTEM, Auger, and controlled sintering experiments. We modeled both W-based and Mo-based binary refractory alloys. Our experimental work was mostly conducted in the Ni-doped Mo, where we also clarified several controversies regarding the solid-state GB wetting in this system.

This work may have broad scientific and technological impacts on other studies of materials properties [5] and geology [2,3], including various materials for energy applications [8]. Indeed, this nanoscale interfacial phenomenon not only controls the activated sintering (materials processing) [6,9,10,11], but also affects the mechanical

properties (such as, GB embrittlement [12] and high-T creep [13,14]), microstructure evolution (e.g. normal and abnormal grain growth) [12,15,16,17,18], chemical stability (e.g. oxidation and corrosion resistance) [19], electronic properties (*e.g.* ZnO-based varistor) [6,20,21], and liquid metal embrittlement (with important applications for nuclear reactors) [8].

Specifically, our detailed study of IGFs in refractory metals extends the observation and theory of this nanoscale interfacial phenomenon from ceramics to metals. Since the interfacial interactions in metals are generally less complicated, a quantitative thermodynamic model predicting IGF stability has been developed and verified by experiments in this thesis study. This model serves as a basis to establish a more complex model for IGFs in ceramics, where we may include other interfacial interactions, such as London dispersion forces and electrostatic forces.

A review of pertinent literature is given in Chapter 2. Chapter 3 details the experimental procedures. Subsequently, Chapter 4 discusses a model of doped W systems and its validation by comparison with prior sintering data. Chapter 5 describes a study of GB wetting and prewetting in Ni-doped Mo, which clarifies a few controversies in existing literature. Chapter 6 further extends and elaborates the thermodynamic model using the Ni-doped Mo as an example. Chapter 7 presents a systematic controlled sintering study of the Ni-doped Mo system to validate the model and computed GB diagram presented in Chapter 6. Chapter 8 describes a preliminary study of Mo-Si-B based alloys. Conclusions are drawn in Chapter 9.

References

[1] JS Wettlaufer. Impurity Effects in the Premelting of Ice Physical Review Letters 82 (1999) 2516.

[2] JG Dash, H Fu, JS Wettlaufer. The Premelting of Ice and Its Environmental Consequences Reports on Progress in Physics 58 (1995) 115.

[3] JG Dash, AM Rempel, JS Wettlaufer. The Physics of Premelted Ice and Its Geophysical Consequences Reviews of Modern Physics 78 (2006) 695.

[4] TE Hsieh, RW Balluffi. Experimental Study of Grain Boundary Melting in Aluminum Acta Metallurgica 37 (1989) 1637.

[5] J Luo. Stabilization of Nanoscale Quasi-Liquid Interfacial Films in Inorganic Materials: A Review and Critical Assessment Critical Reviews in Solid State and Material Sciences 32 (2007) 67.

[6] J Luo, H Wang, Y- Chiang. Origin of Solid State Activated Sintering in Bi2O3-Doped ZnO Journal of the American Ceramic Society 82 (1999) 916.

[7] VK Gupta, DH Yoon, HM Meyer III, J Luo. Thin Intergranular Films and Solid-State Activated Sintering in Nickel-Doped Tungsten Acta Materialia 55 (2007) 3131.

[8] PJ Desre. A mechanism for the stress independent grain boundary penetration of a metal by a liquid metal. Application to the metallic couple Al-Ga Scripta Materialia 37 (1997) 875.

[9] JH Brophy, LA Shepard, & J Wulff. in: W Leszynski (Ed.), Powder Metallurgy, Interscience, 1961, pp. 113-35.

[10] HW Hayden, JH Brophy. Activated Sintering of Tungsten with Group VIII Elements Journal of Electrochemcial Society 110 (1963) 805.

[11] RM German, ZM Munir. Enhanced Low-Temperature Sintering of Tungsten Metallurgical Transactions 7A (1976) 1873.

[12] G Gottstein, DA Molodov. Grain Boundary Migration in Metals: Recent Developments Interface Science 6 (1998) 7.

[13] PF Becher, GS Painter, EY Sun, CH Hsueh, MJ Lance. The Importance of Amorphous Intergranular Films in Self-Reinforced Si3N4 Ceramics Acta Materialia 48 (2000) 4493.

[14] D Chen, ME Sixta, X- Zhang, LC DeJonghe, RO Ritchie. Role of the Grain Boundary Phase on the Elevated-Temperature Strength, Toughness, Fatigue and Creep Resistance of Silicon Carbide Sintered with Al, B, and C Acta Materialia 48 (2000) 4599.

[15] JH Choi, N Hwang, DY Kim. Pore-Boundary Separation Behavior during Sintering of Pure and $Bi_2O_3$-Doped ZnO Ceramics Journal of the American Ceramic Society 84 (2001) 1398.

[16] I MacLaren, RM Cannon, MA Gülgün, R Voytovych, NP Pogrion, C Scheu et al. Abnormal Grain Growth in Alumina: Synergistic Effects of Yttria and Silica Journal of the American Ceramic Society 86 (2003) 650.

[17] I- Moon, K- Kim, S- Oh, M- Suk. Nickel-Enhanced Grain Growth in Tungsten Wire Journal of Alloys and Compounds 201 (1993) 129.

[18] SJ Dillon, MP Harmer. Multiple Grain Boundary Transitions in Ceramics: A Case Study of Alumnia Acta Materialia 55 (2007) 5247.

[19] JA Cooper, DR Cousens, S Myhra, RSC Smart. Intergranular Films and Pore Surfaces in Synroc C: Structure, Composition, Dissolution Characteristics Journal of the American Ceramic Society 69 (1986) 347.

[20] Y- Chiang, LA Silverman, RH French, RM Cannon. Thin Glass Film Between Ultrafine Conductor Particles in Thick-film Resistors Journal of the American Ceramic Society 77 (1994) 143.

[21] DL Callahan, G Thomas. Impurity Distribution in Polycrystalline Aluminum Nitride Ceramics Journal of the American Ceramic Society 73 (1990) 2167.

# CHPATER TWO

# LITERATURE REVIEW

## 2.1 Surface and Grain Boundary Premelting in Unary Systems

Surface and grain boundaries (GBs) play significant roles in the fabrication and properties of metallic and ceramic materials. Surface (or GB) premelting refers to the stabilization of a thin quasi-liquid layer on a surface (or at a GB) when the temperature is still below the melting point of the bulk material. The surface premelting phenomenon in ice had been convincingly confirmed by various experiments [1]. Premelting of ice is a major reason that ice is slippery [2]. Furthermore, surface and GB premelting plays a key role in the consolidation (sintering), adhesion, and creep of snow and ice. Thus, it has major environmental consequences, for example, in the phenomena of frost heave, glacier motion, and electrical charging in thunderstorms [1,3]. GB premelting has been observed in a colloidal crystal system where the structural unit is 300-400 nm monodispersed polymer particles (instead of atoms), where a GB becomes disordered when the temperature approaches the $T_{melt}$ from below [4]. For a real one-component material, aluminum, a hot-stage TEM experiment conducted at MIT in 1980s showed that GB premelting did not occur up to 1 $^{o}$C below the melting temperature for aluminum [5]. Since then, the materials community was greatly discouraged, and it is generally believed that GB premelting in unary materials is unimportant for materials science.

## 2.2 Grain Boundary Transitions

A first-order transition refers to as a phase transition whereby the free energies of two phases are equal, but the first derivative of the free energy is discontinuous at the transition point. In 2006, Tang and Carter used a diffuse-interface model to analyze GBs, and they showed that the first-order GB transitions can occur in both unary materials [6,7,8] and binary alloys. In unary systems, this GB transition is a premelting transition [7]. In binary systems, this GB transition can be interpreted as a coupled premelting (structural disordering) and prewetting (adsorption) transition [8]. In their model, the GB is treated as a unique phase which is different from bulk phase. If a thermodynamic variable (degree of order, $\eta$ or GB excess) which represents the GB properties is plotted vs. temperature, a finite jump can occur at a GB transition point, e.g., at a GB premelting temperature below bulk melting point. Tang et al. also predicted the existence of GB critical points, above which GB transitions become continuous (high order) [7,8].

## 2.3 Impurity-based Quasi-liquid Interfacial Films

Impurity-based equilibrium-thickness intergranular films (IGFs) were widely observed and extensively studied in ceramic systems. [9] They can be stabilized below and above the solidus line. The stabilization of these impurity-based quasi-liquid IGFs below the bulk solidus line in multicomponent systems is phenomenologically analogous

to the simpler phenomenon of GB premelting in unary systems. These IGFs show several unique characteristics [9]:

- Thermodynamic stability below the bulk eutectic/peritectic temperature
- Disordered structure, like a liquid, but with some partial crystalline order (Fig. 2.1)
- Structural and compositional gradients across the film thickness direction
- A self-selecting or "equilibrium" thickness on the order of 1 nm
- High diffusivity

These IGFs play important roles in electronic and mechanical properties as well as fabrication of various ceramic materials.

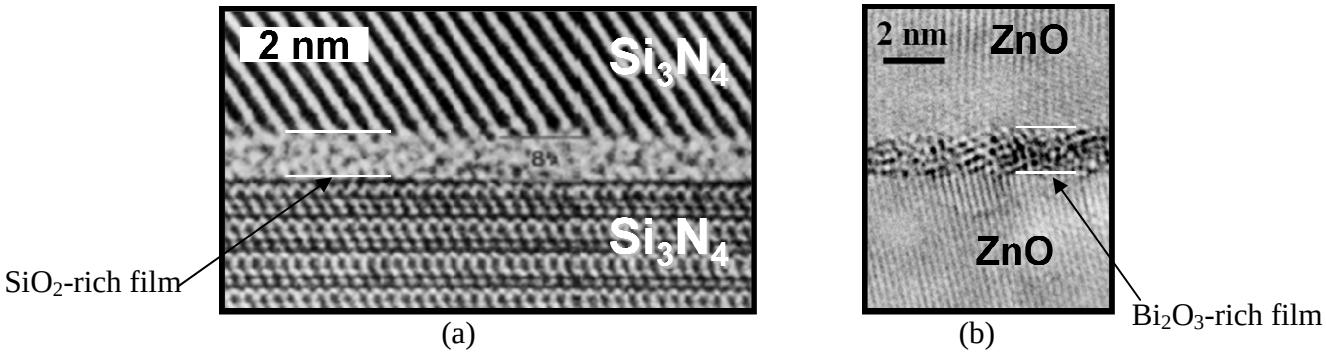


Figure 2.1 Representative HRTEM images of impurity-based liquid-like IGFs.

A force-balance model and a diffuse-interface model have been developed to explain the equilibrium-thickness of IGF [9]. The formation of quasi-liquid IGF can be understood in the frame of a coupling premelting and prewetting theory [9,10]. Tang et al. [7,8] employed the diffuse-interface theory to predict the formation of quasi-liquid IGF via a first-order GB transition (Fig.2.2(a)). But since the London dispersion force (as the

major component of the *van der Waals* force) and electrostatic force that complicate the scenario in ceramics are not considered, Tang's model is better applied to binary metallic systems. Due to the *vdW* force, the complete wetting was not immediately observed in ceramic systems when temperature was increased above the bulk $T_{eutectic}$ (Fig. 2.2(b)) [9].

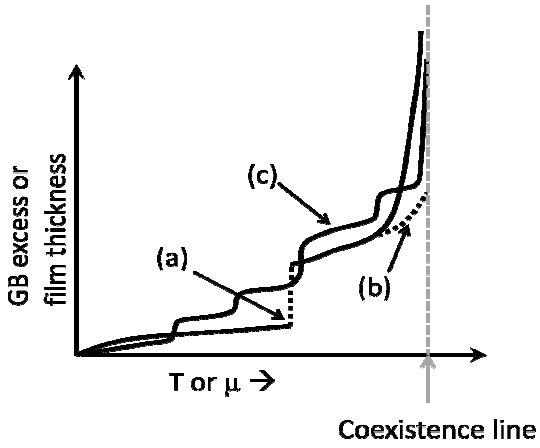


Figure 2.2 Thickness (GB excess) of a GB layer versus temperature or chemical potential. The GB transition can be (a) first-order, (b) incomplete (frustrated by an attractive *vdW* force), or (c) it can occur via layering transitions (producing a series of GB complexions) [9].

On the other hand, surficial amorphous films (SAF) were also studied in $Bi_2O_3$-doped ZnO and other systems [11]. They show the similar characteristics with quasi-liquid IGF (Fig. 2.3 (a)). Therefore, they are generally regarded as surface counterparts to the IGF. SAF can also be stabilized into the subsolidus regime while an analogy to surface premelting in one component systems can be drawn. When $T > T_{eutectic}$, the complete wetting can also be suppressed if an attractive *vdW* force is present (Fig.2.2 (b)). A recent study of SAF in vanadia-doped titania system (Fig. 2.3 (b)) confirmed the

existence of a first-order surface transition, at which the film thickness jumps discontinuously (Fig. 2.2 (a)).

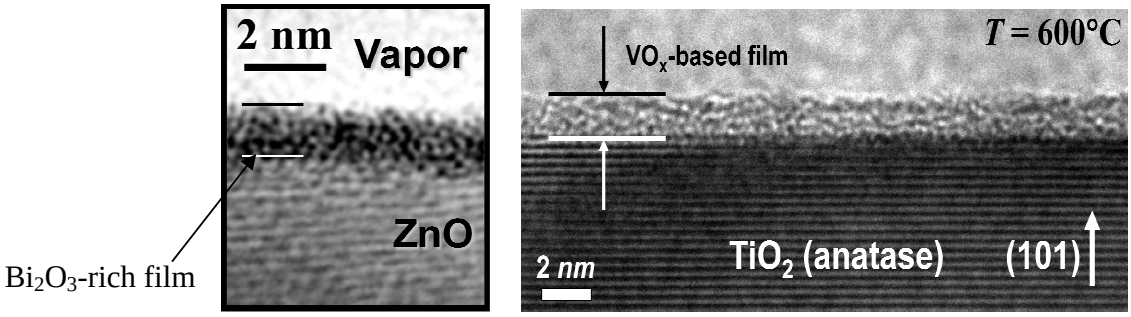


(a) (b)

Figure 2.3 Representative HRTEM images of SAFs [11,12,13].

Most recently, Dillon and Harmer observed a series of GB complexions (= GB "phases") in doped-$Al_2O_3$ systems by HRTEM and HAADF-STEM. The structures of this series of GB complexions are schematically shown in Fig. 2.4. The formation of these six GB "phases" can be understood from a series of layering transitions: from monolayer and bilayer adsorption, to multilayer (trilayer), nanoscale IGF, and thick wetting films, as illustrated in Fig.2.2 (c). This can be considered as yet another extension to GB prewetting/premelting model, indicating that a wide range of diversifying and interesting interfacial "phase" transitions can occur at GB.

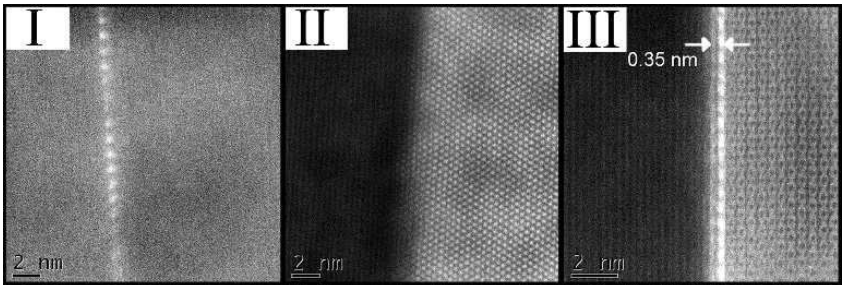


(a)

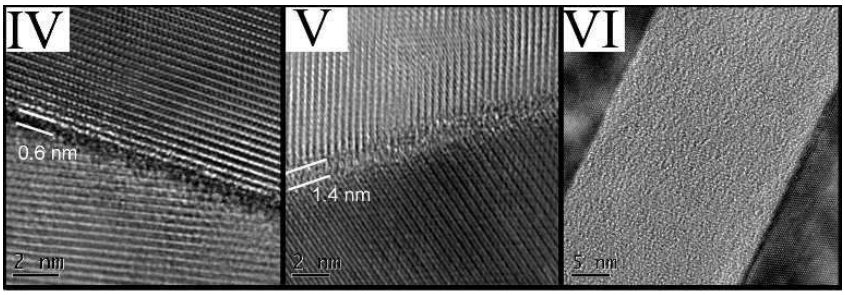


(b)

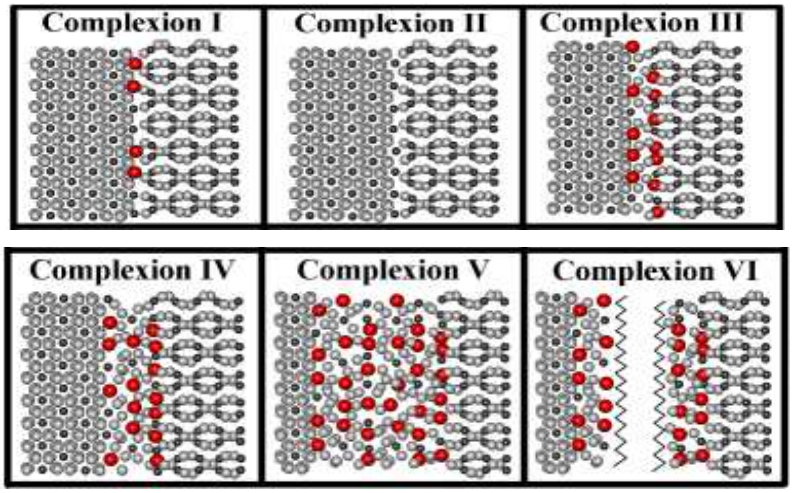


(c)

Figure 2.4 The HAADF-STEM (a) and HRTEM (b) images of GB complexions in doped- $Al_2O_3$ and their schematic structures (c). [14,15]

## 2.4 Theories and Models of Equilibrium-thickness IGF

Two types of models have been developed: force-balance models and diffuse-interface models. The force-balance models, by its name, are built upon the assumption that the quasi-liquid IGF is stabilized because of a balance between attractive forces and repulsive interfacial forces. In ceramic systems, short-range (steric) and electrostatic forces serve as repulsive force. For subsolidus IGFs, the free energy penalty for forming the undercooled liquid can be treated as attractive force. For IGFs in ceramic materials, the *vdW* force is also attractive and often significant (It can be repulsive for SAFs, and it is generally insignificant for metallic systems). Force-balance models assume that an IGF is uniform in composition and structure. Nevertheless, through-thickness gradients in composition and structure generally exist [9,16]. These gradients can be treated in diffuse-interface (phase-field) models. Tang et al. analyzed a diffuse-interface model for a binary alloy and predicted a first-order GB transition [8]. However, this diffuse-interface model did not consider *vdW* and electrostatic forces [9] that are generally present in ceramic systems. Moreover, diffuse-interface models are more difficult to quantify and to be compared with experiments. In this research, we focus on force-balance models for the sake of simplicity and the possibility of quantification.

The basic physical principle of stabilizing a quasi-liquid IGF is as follows. When the energy penalty (the free energy of amorphization, $\Delta G_{\text{amorph}}$) is more than offset by the interfacial energy reduction due to the replacement of one original GB by two liquid-crystal interfaces, the quasi-liquid IGF can be thermodynamically stabilized (Fig. 2.5):

$$\Delta G_{\text{vol.}} \cdot h < -\Delta\gamma \equiv \gamma_{gb}^{(0)} - 2\gamma_{cl} \ . \tag{2.1}$$

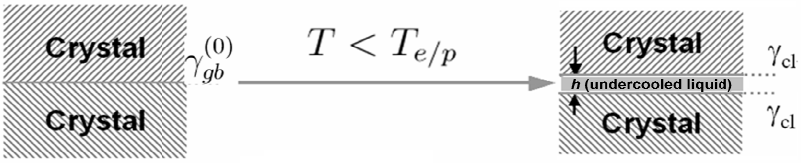


Figure 2.5 Illustration of the principle of stabilizing a nanoscale quasi-liquid IGF when the liquid phase is not yet a stable bulk phase.

Furthermore, a force-balance model can be proposed which also include other interfacial interactions, such as the *vdW* and electrostatic interaction. Subsequently, the total excess free energy of an IGF in a ceramic system can be written as:

$$G^x - \gamma_{GB}^{(0)} = \Delta G_{amorph} \cdot h + \Delta\gamma + \underbrace{\Delta\gamma \cdot e^{-\frac{h}{\zeta}}}_{Interfacial} + \underbrace{\frac{H_{121}}{12\pi h^2}}_{van-der-Waals} + \underbrace{(-\frac{\sigma^2}{\varepsilon\varepsilon_0\kappa}e^{-\kappa\cdot h})}_{Electrostatic} \tag{2.2}$$

In Eq. 2.2, first two terms originate from Eq. 2.1, which stand for the free energy of amorphization and interfacial energy reduction, respectively. The third term represents short-range interfacial interaction of structural and compositional original (originated from the interactions of two adjacent grains and structural/compositional gradients); $\zeta$ is a coherent length, which is scaled with the bond length. The fourth term represents the free energy arising from *vdW* interaction where $H_{121}$ is the Hamaker constant for the system crystal(1)/film(2)/crystal(1). The fifth term shows the electrostatic interaction, which is built upon the classic electrical double layer (EDL) theory or DLVO theory in colloidal system. Here, $\kappa^{-1}$ is the Debye length. In a metallic system, there is no electrostatic force

and *vdW* force is insignificant. I will discuss the force-balance model in metallic systems in later chapters.

## 2.5 Subsolidus Activated Sintering in Refractory Metals – A 50 Years Mystery

The activated sintering in refractory metals is referred to as the phenomenon whereby the densification rate can be significantly enhanced if a small amount of dopants (mostly group VIII transition metals, such as Ni or Co) was added. In a classic review article [17] in 1978, Coble and Cannon stated that "the most significant changes which have been taken place in recent years regard the finding with respect to densification below the eutectics in numerous systems, notably tungsten-carbide:cobalt, tungsten:nickel, …" Although the study of activated sintering in refractory metals became active since 1960s' especially in the powder metallurgy community, the exact mechanism underneath remains unknown for decades.

A widely accepted qualitative explanation (the "classical wisdom") stated that "solid-state wetting" happened, where a crystalline film of a dopant-rich secondary phase formed at GB, thereby enhancing the GB transport rates [18,19]. But there are several open questions:

- Does the "solid-state wetting" really exist? No solid evidence has been presented to support the existence of solid-state wetting in activated sintering systems.

- Does this crystalline film have macroscopic (arbitrary) thickness (as implicated by complete wetting)?

On the other hand, a recent study attributed an enhanced GB transport in $Bi_2O_3$-doped ZnO to a "short-circuit" diffusion in nanoscale liquid-like films that are stabilized at GB well below the bulk eutectic temperature [20]. There is a similarity in activated sintering between $Bi_2O_3$-doped ZnO and doped refractory metals. It inspired us to seek the similar disordered films in doped refractory metals.

A more recent HRTEM study of Ni-doped W revealed the existence of disordered interfacial films at GB in 1 at % Ni doped W. Auger Electron spectroscopy characterization indicated that these films are Ni-rich and their thickness is a function of temperature and doping level [21,22]. These subsolidus quasi-liquid films appear to be the metallic counterparts to the well-known IGF in ceramic systems.

In addition, there were systematical studies of sintering kinetics in W doped with different group VIII transition metals. In several papers in 1960's to 1970's [23,24], the effects of dopants, including Pd, Ni, Fe, Co, Ru, Rh and Cu, on the sintering rate of W were extensively investigated. The effectiveness of dopants can be roughly ranked as: Pd, Ni >Fe, Co, Ru > Cu. However, no clear explanation about the effectiveness of these dopants was offered at that time. It motivated us to build a thermodynamic model that could predict the effectiveness of sintering aids from the GB disordering point of view.

## 2.6 Ni-doped Mo

Ni-doped Mo is another interesting refractory metallic system which shows activated sintering. Same as the earlier explanation for doped W systems, it was proposed by Huang [25] that the δ–NiMo compound formed crystalline nanoscale films at GB, which enhance the GB transport rates. This implied the occurrence of a complete solid-state GB wetting. If so, an arbitrary film thickness would be expected. However, the observation of a 2-nm thick GB film seems to be in conflict with the complete GB wetting explanation. In principle, a nanoscale crystalline IGF can also exhibit an equilibrium thickness. An alternative explanation is that this film was disordered but become re-crystallized upon cooling. Our research clarified this controversy by demonstrating that solid-state GB wetting does not occur and nanoscale liquid-like IGFs can be stabilized at high-temperatures.

References

[1] JG Dash, H Fu, JS Wettlaufer. The Premelting of Ice and Its Environmental Consequences Reports on Progress in Physics 58 (1995) 115.

[2] R Rosenberg. Why Is Ice Slippery? Physics Today 58(12) (2005) 50.

[3] JG Dash, AM Rempel, JS Wettlaufer. The Physics of Premelted Ice and Its Geophysical Consequences Reviews of Modern Physics 78 (2006) 695.

[4] AM Alsayed, MF Islam, J Zhang, PJ Collings, AG Yodh. Premelting at Defects within Bulk Colloidal Crystals Science 309 (2005) 1207.

[5] TE Hsieh, RW Balluffi. Experimental Study of Grain Boundary Melting in Aluminum Acta Metallurgica 37 (1989) 1637.

[6] M Tang, WC Carter, RM Cannon. Grain Boundary Order-Disorder Transitions Journal of Materials Science 41 (2006) 7691.

[7] M Tang, WC Carter, RM Cannon. Diffuse Interface Model for Structural Transitions of Grain Boundaries Physical Review B 73 (2006) 024102.

[8] M Tang, WC Carter, RM Cannon. Grain Boundary Transitions in Binary Alloys Physical Review Letters 97 (2006) 075502.

[9] J Luo. Stabilization of Nanoscale Quasi-Liquid Interfacial Films in Inorganic Materials: A Review and Critical Assessment Critical Reviews in Solid State and Material Sciences 32 (2007) 67.

[10] M Tang, WC Carter, RM Cannon. Grain Boundary Transitions in Binary Alloys Physical Review Letters 97 (2006) 075502.

[11] J Luo, Y- Chiang. Equilibrium-thickness Amorphous Films on {11-20} Surfaces of $Bi_2O_3$-Doped ZnO Journal of the European Ceramic Society 19 (1999) 697.

[12] H Qian, J Luo. Vanadia-Based Equilibrium-Thickness Amorphous Films on Anatase (101) Surfaces Applied Physics Letters 91 (2007) 061909.

[13] H Qian, J Luo. Nanoscale surficial films and a surface transition in V2O5-TiO2-based ternary oxide systems Acta Materialia 56 (2008) 4702.

[14] SJ Dillon, MP Harmer. Multiple Grain Boundary Transitions in Ceramics: A Case Study of Alumnia Acta Materialia 55 (2007) 5247.

[15] SJ Dillon, M Tang, WC Carter, MP Harmer. Complexion: a new concept for kinetic engineering in materials science Acta Materialia 55 (2007) 6208.

[16] A Subramaniam, CT Koch, RM Cannon, M Rühle. Intergranular Glassy Films: An Overview Materials Science and Engineering A 422 (2006) 3.

[17] RL Coble, RM Cannon. Current Paradigms in Powder Processing (1978) 151.

[18] JH Brophy, LA Shepard, & J Wulff. in: W Leszynski (Ed.), Powder Metallurgy, Interscience, 1961, pp. 113-35.

[19] RM German. Diffusional Activated Sintering - Densification, Microstructure and Mechanical Properties Progress in Powder Metallurgy 39 (1984) 243.

[20] J Luo, H Wang, Y- Chiang. Origin of Solid State Activated Sintering in Bi2O3-Doped ZnO Journal of the American Ceramic Society 82 (1999) 916.

[21] J Luo, VK Gupta, DH Yoon, HM Meyer. Segregation-Induced Grain Boundary Premelting in Nickel-doped Tungsten Applied Physics Letters 87 (2005) 231902.

[22] VK Gupta, DH Yoon, HM Meyer III, J Luo. Thin Intergranular Films and Solid-State Activated Sintering in Nickel-Doped Tungsten Acta Materialia 55 (2007) 3131.

[23] RM German, ZM Munir. Enhanced Low-Temperature Sintering of Tungsten Metallurgical Transactions 7A (1976) 1873.

[24] HW Hayden, JH Brophy. Activated Sintering of Tungsten with Group VIII Elements Journal of Electrochemcial Society 110 (1963) 805.

[25] KS Hwang, HS Huang. Identification of the Segregation Layer and Its Effects on the Activated Sintering and Ductility of Ni-doped Molybdenum Acta Materialia 51 (2003) 3915.

# CHAPTER THREE

# EXPERIMENTAL PROCEDURES

## 3.1 Raw Materials

In the present study, high purity molybdenum (99.999%) with an average particle size of 20 microns was purchased from Alfa Aesar. To achieve a homogeneous distribution of nickel in molybdenum, nickel chloride ($NiCl_2 \cdot 6H_2O$, Alfa Aesar) was mixed with molybdenum in solution. Then, the slurry was dried in an oven at 90 ºC. Afterwards, the powders were annealed in a tube furnace at 600 ºC for 1 hour under the flowing gas of Ar-5% $H_2$ to reduce nickel chloride to nickel. This procedure is called calcine. The characteristics of nickel and molybdenum are shown in Table 3.1.

Table 3.1 Physical properties of nickel and molybdenum [1].

| Element | Nickel (Ni) | Molybdenum (Mo) |
|---|---|---|
| Atomic number | 28 | 42 |
| Atomic weight | 58.69 | 95.94 |
| Density (20 ºC g/cm3) | 8.90 | 10.28 |
| Crystal structure | FCC | BCC |
| Atomic radius (nm) | 0.125 | 0.139 |
| Ionic radius (nm) | 0.069 | 0.062 (+6e), 0.070 (+4e) |
| Most common valance | 2+ | 4+, 6+ |
| Melting point (ºC) | 1455 | 2623 |

The binary phase diagram of Ni-Mo is shown in Fig. 3.1. Experimental designs are based on this diagram. We investigated the GB phenomena and sintering behaviors in three phase regimes: single-phase regime (BCC), sub-peritectic two-phase regime (BCC+δ) and solid-liquid two-phase regime, which are marked in the inset of the phase diagram.

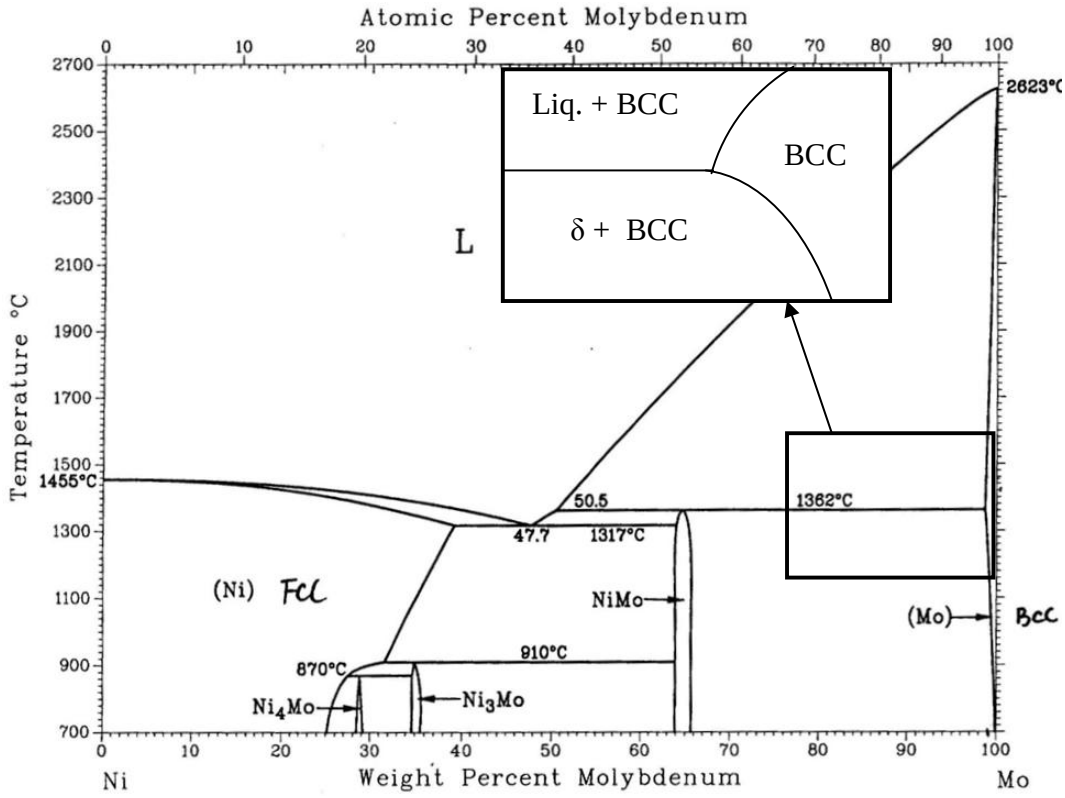


Figure 3.1 Phase diagram of the binary Ni-Mo system. The inset is an enlarged view of the regoins where we conducted experiments [2].

## 3.2 Specimens Preparation

Ni-Mo green specimens were prepared using a standard powder metallurgy method. The calcined Ni-doped Mo powders were grinded gently using a spatula or mortar. Thereafter, cylinder-shape specimens were prepared using a hand press with 280 MPa pressure and a die. The pressed green specimen had a diameter of ~6.36 mm and an average height of 8-9 mm. To prevent formation of a transient liquid and to ensure the specimens are chemically homogenous, all green specimens were pre-sintered at 1100 ºC

for 12 hours in flowing Ar-5% $H_2$. Finally, the specimen was placed in an oil-quench furnace at a desired temperature and isothermally sintered for 3 hours. Afterwards, the specimen was dropped into room temperature diffusion pump silicone oil in less than 1 second inside the quench chamber under vacuum. The well-quenched specimens were characterized by a scanning electron microscope (SEM, Hitachi 4800) and a HRTEM (Hitachi 9500, 300 kV).

In the experiments probing the sintering kinetics, the calcine and press procedures were the same, but the presintering was conducted at 1000 ºC for 1 hour and isothermal sintering was carried out in another gas-quench furnace. The lower pre-sintering temperature and shorter pre-sintering time enable us to have a longer window to extract GB diffusivity via kinetic data.

## 3.3 High-temperature Oil-quench Furnace

A high-temperature quench furnace was customer built. The schematic of this furnace is shown in Fig. 3.2 (a), and the devise is shown in Fig. 3.2 (b).

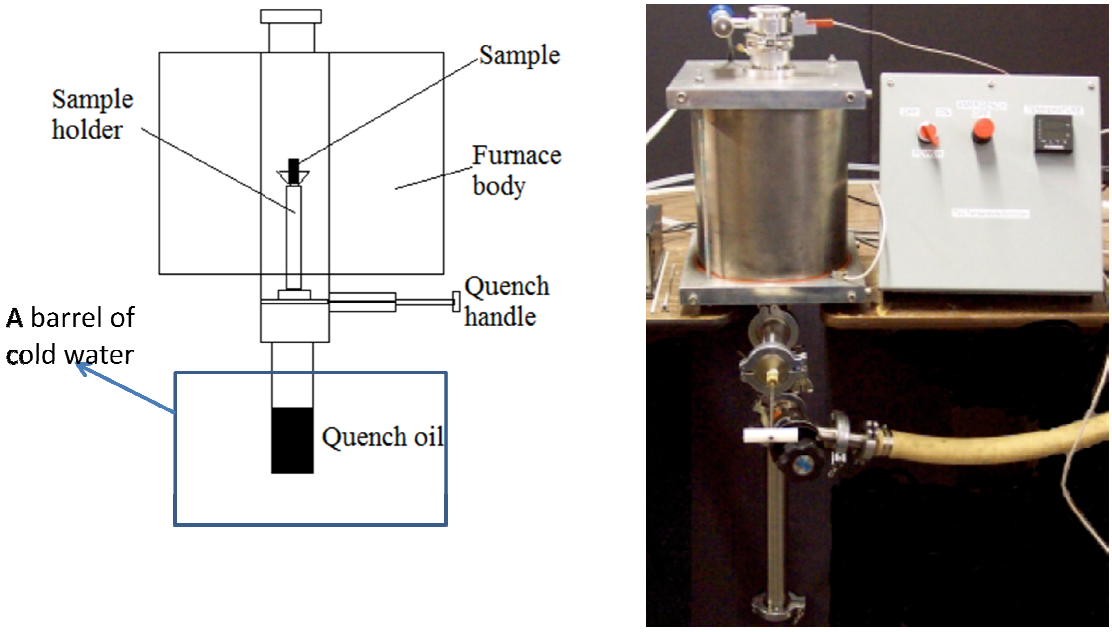


Figure 3.2 (a) Schematic and (b) embodiment of the high-temperature quench furnace.

Only one specimen may be placed on the sample holder in this furnace for each run. This sample holder is comprised of an alumina tube and a spiral-shape Mo wire container (Fig. 3.3), When isothermal sintering was accomplished, we pulled the quench handle to let the specimen to fall into quench oil (diffusion pump silicone oil), which took less than 1 second.

Figure 3.3 The specimen holder for the oil-quench furnace.

## 3.4 Furnace for Probing the Sintering Kinetics

We also assembled another furnace specifically for designed sintering experiments to extract GB diffusivity as a function of temperature and chemical potential. The schematic of this furnace is shown in Fig. 3.4. It is a vertical tube furnace. When the furnace was running, Ar + 5% $H_2$ gas is flowing through the system to protect specimens from oxidation. This furnace is unique in that a mechanism of loading/unloading samples was built so that the specimens can be inserted into the hot zone of the furnace after the furnace reaches pre-set temperature. The specimens can also be taken out for gas quench after a predetermined sintering time by pulling out the crucible back to the cold-zone. The advantage is that the specimens are heated to a target temperature in a negligibly short time (~2 minutes), so there is almost no heating ramp in beginning period. Moreover, after a certain sintering time, the specimen can be cooled down quickly (to below 800 ºC in ~1 min) so that cooling ramp is also negligible. By doing this, the effects

of heating and cooling ramps are minimized. In all experiment, a second thermocouple is placed in the crucible to monitor the actual temperature of the specimens.

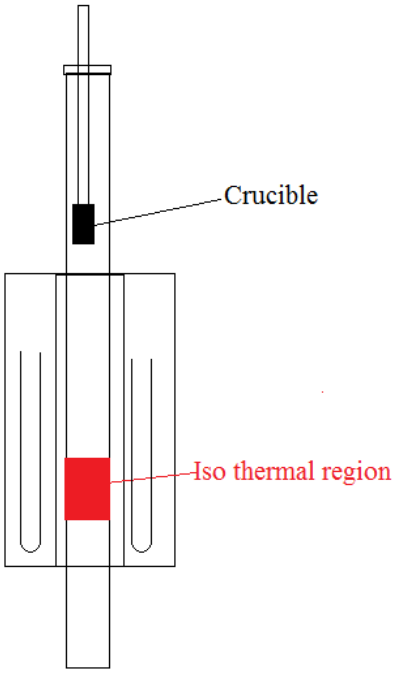


Figure 3.4 The schematic of the gas-quench furnace for probing sintering kinetics.

The density of the sample was determined by measuring the sample dimension and mass. All the green specimens were cylinder-shaped. These cylindrical green specimens deformed to truncated cone shape after sintering. Therefore three measurements were conducted on the diameter of each specimen at different heights.

Through measuring the density (and microstructure) as a function of time during sintering, we can calculate the densification rate. Bulk or GB diffusivity can then be determined by fitting the well established sintering kinetic models. The relevant sintering kinetic models are described in the next section. The extracted GB diffusivity as a function of doping level and temperature can be correlated with our thermodynamic

models and the GB structure/chemistry observed by HRTEM and Auger Electron Spectroscopy studies.

## 3.5 Sintering Models

Bulk/GB diffusivity can be extracted by fitting experimentally measured densification vs. time curves to the well-established sintering models. In the Coble sintering model, densification is divided into three stages: the initial stage, the intermediate stage, and the final stage. These three stages are label in the density vs. time plot in Fig. 3.5 [3].

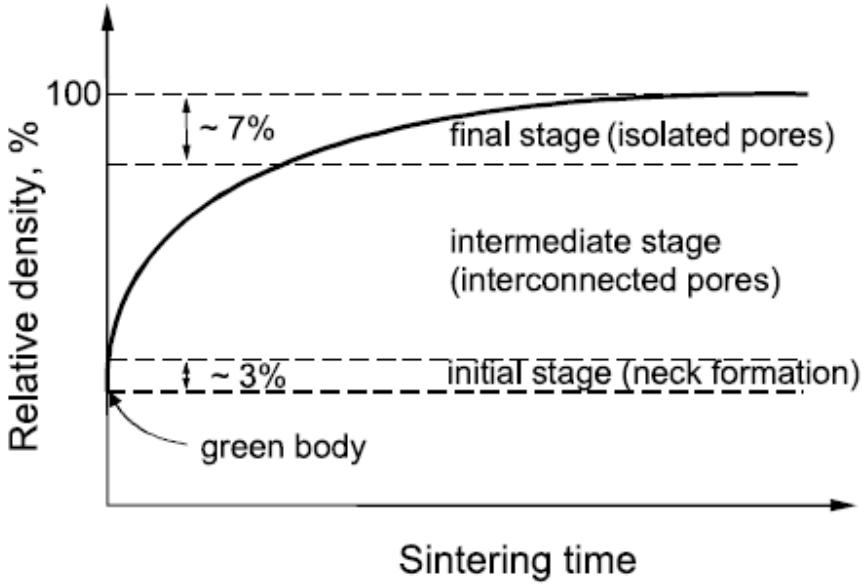


Figure 3.5 Typical relative density vs. time during sintering [3].

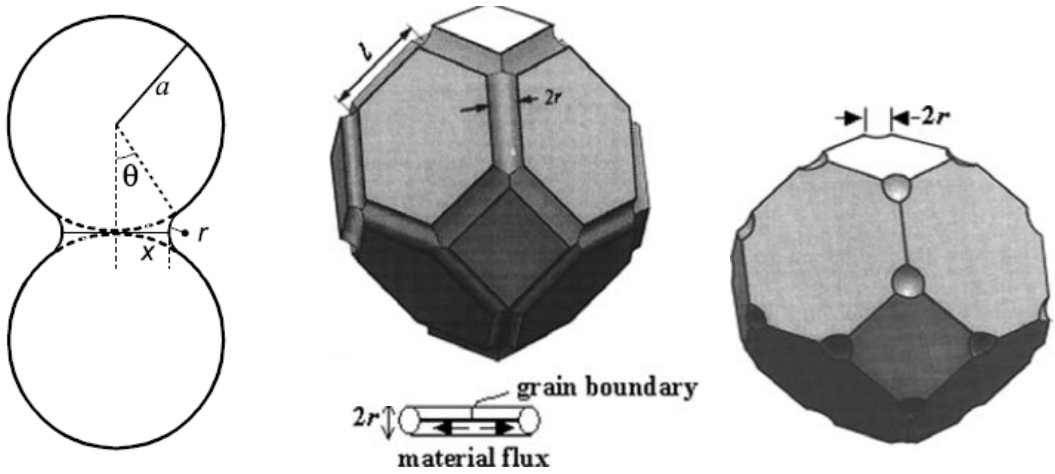


(a) (b) (c)

Figure 3.6 The models for (a) initial, (b) intermediate, and (c) final stage of sintering [3].

During the initial-stage sintering, necks form between particles and densification can occur if there is bulk or GB diffusion (but no densification if there is only surface diffusion or vapor phase transport). The initial-stage sintering is often modeled using a two-sphere model as shown in Fig. 3.6(a). In the intermediate stage (Fig. 3.6 (b)), a continuous interconnected pore channel forms and shrinkage is large, but grain growth is expected to be mild (because GB are pinned by the pore channels). In the final stage (Fig. 3.6 (c)), the pores become isolated at quandary junctions and grain growth may be significant. In the following part, the sintering models for three different stages will be briefly introduced.

**Initial-Stage Sintering**

The Johnson model [4] is the most widely used for the initial stage of sintering. The key assumptions are:

- Transport due to dislocation or small angle grain boundary is negligible;

- The grain geometry can be represented by two round grains in contact with each other as shown in Fig. 3.6;
- The surface and GB energy are isotropic;
- Vacancy concentration potentials are equal for bulk diffusion and GB diffusion ($\nabla\mu_{XL} = \nabla\mu_{GB}$); and
- The densification rate is small ($\Delta L/L_0 < 0.05$).

In the Johnson model, the densification vs. time is represented by:

$$\frac{\Delta L}{L_0} = \left[ K \frac{\gamma_s \Omega D}{kTG^p} \right]^m t^m \tag{3.1}$$

where:

$K$ = (3.1-6.9)*8; $m$ = ~0.4-0.5, $p$ = 3, $D = D_{XL}$; for bulk diffusion dominant sintering; and

$K$ = (1.6-3)*16; $m$ = ~0.3, $p$ = 4, $D = \delta D_{GB}$ for GB diffusion dominant case.

In the above equations, $\Delta L/L_0$ is the linear shrinkage; $\gamma_s$ is the surface energy of the particle materials; $\Omega$ is the volume of single vacancy; $D_{XL}$ is the bulk diffusivity; $D_{GB}$ is the GB diffusivity; $\delta$ is the GB width (which is arbitrarily selected to be 1 nm in most prior studies); $k$ is the Boltzmann constant; $T$ is the sintering temperature; and $G$ is the grain size. German also proposed a similar model [5,6].

**Intermediate-Stage Sintering**

Coble developed the model for intermediate stage sintering [7]. The key assumptions are:

- Grain boundaries are the sink of vacancies and pores are the source of vacancies ($J_v = -J_{atom}$);
- The grain geometry is represented by a tetrakaidecahedra (Fig. 3.6(b)) with a continuous pore channel at triple-grain junctions; and
- The pore channels have cylindrical.

If the intermediate stage sintering is controlled by bulk diffusion, the porosity and its derivative with respect to time can be expressed as:

$$P_v - P_v^0 = -336\frac{D_{XL}\gamma_s\Omega}{kTG^3}t \tag{3.2}$$

$$\frac{dP}{dt} = -336\frac{D_{XL}\gamma_s\Omega}{kTG^3} \tag{3.3}$$

On the other hand, if the intermediate stage sintering is controlled by GB diffusion, the porosity and its derivative with respect to time can be expressed as:

$$P_v^{\frac{3}{2}} - P_v^{0\frac{3}{2}} = -1281\frac{\delta D_{GB}\gamma_s\Omega}{kTG^4}t \tag{3.4}$$

$$\frac{dP^{\frac{3}{2}}}{dt} = -1281\frac{\delta D_{GB}\gamma_s\Omega}{kTG^4}$$

Those equations above assume a constant grain size. All the variables appearing in above equations are defined the section of the initial-stage sintering model, except that $P_v$ is porosity and it is defined:

$$P_v = (1 - \rho_{relative}) \tag{3.5}$$

where $\rho_{relative}$ is the relative density.

**Final-Stage Sintering**

After the interconnected pore channels break up and pores become isolated, the sintering enters the final stage (Fig. 3.6 (c)). Coble developed a final-stage sintering Model [7], where the relative density was expressed as:

$$\frac{d\rho_r}{dt} = 441\frac{D_{XL}\gamma_s\Omega}{kTG^3} \quad \text{(for bulk diffusion controlled sintering)} \tag{3.6}$$

$$\frac{d\rho_r}{dt} = 735\frac{\delta D_{GB}\gamma_s\Omega}{kTG^4} \quad \text{(for GB diffusion controlled sintering)} \tag{3.7}$$

The three-stage sintering theories are developed for solid-state sintering. However, it can also be extended to liquid-phase sintering by making a few adjustments and modifications. Based on the Kingery liquid-phase sintering model [8], German developed a model for intermediate stage of liquid-phase sintering if the kinetics is controlled by a solution-reprecipitation process [9,10]. Here, the linear densification rates are expressed as:

$$(\frac{\Delta L}{L_0})^3 = 192\frac{\delta D_{GB}\gamma_s\Omega C}{kTG^4}t \tag{3.8}$$

Or:

$$\ln(\frac{\Delta L}{L_0}) = \frac{1}{3}\ln(t) + \frac{1}{3}\ln\{\delta\cdot D_{GB}\cdot[192\frac{\gamma_s V_m C}{RTG^4}]\} \tag{3.9}$$

Here, the variables are defined similarly as those used for soli-state sintering except that δ is the width for the macroscopic liquid films that are present at GB and *C* is composition of the primary element in the liquid phase.

## 3.6 TEM Specimen Preparation

HRTEM is the primary technique we employed to characterize the structure of GB. Preparation of TEM specimens from bulk materials is the first challenging step. To prepare ~3 mm self-supporting TEM specimens, I

1. used Buehler low-speed diamond saw to cut a sintered sample into thin pellets which had the same diameter as the sintered sample (~5.8 mm) and was ~ 1 mm in thickness;
2. roughly polished the cut pellets on both sides on emery papers of grits 320, 400, 600, 800, and 1000 (in a sequence) to reduce the thickness to about 0.2 mm;
3. used a South Bay Technology (SBT) abrasive disc cutter to cut ~3 mm diameter discs;
4. finely polished the disc (0.2 mm thick and ~3 mm in diameter) on emery paper of grit 1000 and then diamond lapping film/diamond paste with 9 μm, 3 μm and 1 μm particle sizes (in a sequence), to produce a final foil of ~50 μm thick; (Note that the recommended final thickness of the foil depends on specific material. For hard metal such as Mo or W, it is recommended to reduce thickness to ~50 μm. For other soft metals or ceramics with high ion-milling etch rates, ~100 μm is generally recommended);
5. used a Fischione (Model 150D) precision dimple grinder to dimple grind the 50 μm thick foil on both side with a dimple of about 22 μm in depth until the thinnest section in the center was about a few microns; (Although generally people leave about 20 μm in the center for ion-milling to perforate it, in our

case of hard metals with low ion-milling etching rates, we try to keep the final center thickness as thin as possible to reduce milling time.) and

6. employed a Fischione Model 1010 low angle argon ion mill to further thin the center of the foil until a perforation appear in the foil and good electron transparency was achieved.

For ion-milling process, key adjustable parameters include accelerating voltage, milling current, milling angle and milling time. Table 3.2 listed a few optimized milling recipes that produced good TEM foils for Mo-Ni specimens.

Table 3.2 Optimized ion-milling recipes for Ni-Mo specimens.

Recipe 1

| Accelerating Voltage | Milling Current | Milling Angle | Stage Temperature | Milling Time |
|---|---|---|---|---|
| 5kV | 5.5 mA | 12º | Liquid $N_2$ | 90 mins |
| 5 kV | 5.5 mA | 9º | Liquid $N_2$ | 30 mins |
| 5 kV | 5.5 mA | 5º | Liquid $N_2$ | 30 mins |

Recipe 2

| Accelerating Voltage | Milling Current | Milling Angle | Stage Temperature | Milling Time |
|---|---|---|---|---|
| 5kV | 5.5 mA | 12º | Liquid $N_2$ | 120 mins |
| 5 kV | 5.5 mA | 9º | Liquid $N_2$ | 60 mins |
| 5 kV | 5.5 mA | 5º | Liquid $N_2$ | 30 mins |

After ion-milling, a good electron transparency should be achieved. The best way to testing electron transparency was to load the milled foil into a TEM and examine it. Primarily, we used the Hitachi-9500 300 kV HRTEM to image our specimen. If the electron transparency was not good enough, additional ion-milling can be carried out to

further thin the specimen. Usually, good HRTEM images can be obtained if one can find a large field of transparent region from the hole in the center to the peripheral edge.

## 3.7 Auger Electron Spectroscopy and Specimen Preparation

Auger Electron Spectroscopy (AES) is an extremely surface sensitive analytical technique. It is used to identify elemental composition of surfaces by measuring the energies of Auger electrons. The energy of an Auger electron is characteristic of the element from which it comes. Compositional depth profiling is performed by using an independent ion beam to sputter the specimen surface while collecting the Auger electron spectrum. Scanning Auger Microscope (SAM) operates like an SEM with an Auger analyzer and an ion sputtering device, which allows analyzing a small spot on a specimen with a high spatial resolution, as well as conducting mapping and line-profiling.

The Auger experiments were conducted at Oak Ridge National Laboratory (ONRL) via the High Temperature Materials Laboratory (HTML) user facility program using a PHI 680 SAM in collaboration with Dr. H. M. Meyer III.

To prevent any contamination, the specimens were fractured in situ in an ultra high vacuum (UHV) chamber. Analysis of GB is possible because the Ni-doped Mo sintered specimens are known to undergo brittle intergranular fracture. A compositional depth profiling was conducted. Sputtering was performed until low and constant Ni composition was reached. The sputtering rate was calibrated to be 2 nm/min for a $SiO_2$ standard at the same experimental condition.

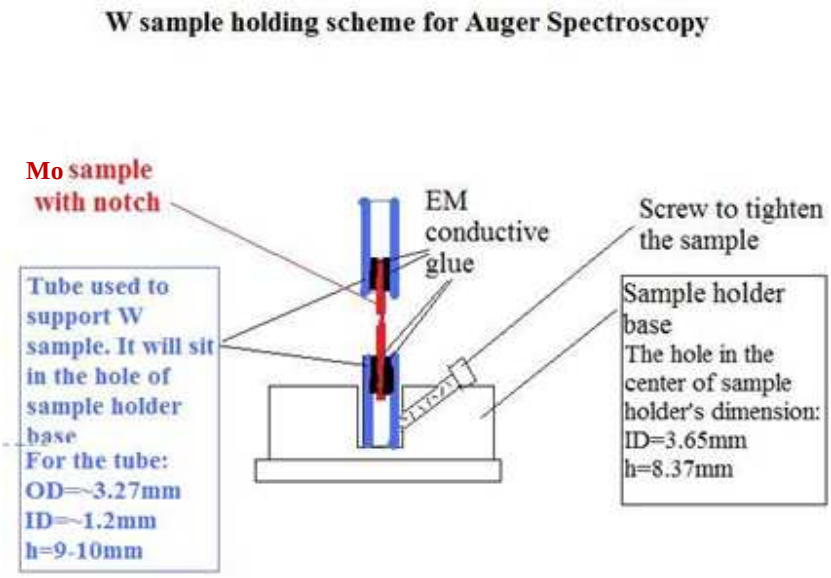


Figure 3.7 Schematic of an AES specimen fixture for in situ fracture.

Fig. 3.7 shows schematically a specimen fixture for in situ fracture in the SAM chamber. The procedure to make the AES specimen is described as follows:

1. A Buehler low-speed diamond saw was used to cut ~1 mm thick disc from sintered sample.
2. The same diamond saw was employed to cut the rectangular sections ~1 mm×1 mm×3.5-5 mm.
3. Two notches was made using the diamond saw on midsection of specimen.
4. After going through a rigorous clean procedure, the notched specimen was fixed into stainless tube on both ends using SEM-grade conductive epoxy.
5. The epoxy-fixed specimen was cured in a 90 ºC oven for 6-8 hours. After cool down, the specimen was wrapped with foam carefully and packed in a plastic box to prevent from being broken.

A noteworthy point was that to minimize the carbon contamination in AES specimen introduced by the cutting fluid, a special clean procedure was implemented to all the notched specimens before making epoxy fixture. The specimens were

1. ultrasonically cleaned with acetone for 20 mins to remove all the polar organic contamination and then let dry fully;
2. ultrasonically cleaned with toluene for 20 mins to remove all the non-polar organic contamination and then let dry fully;
3. ultrasonically cleaned with hexane for 20 mins to remove all the non-polar organic contamination and then let dry fully;
4. ultrasonically cleaned with ethanol for 20 mins;
5. soaked in ethanol overnight 24 hours to remove all the polar organic and hydrophilic contamination; and
6. dried in a 90 ºC oven for 3 hours to evaporate all the residue organic contaminant.

## 3.8 Grain oundary Wetting Experiment

To determine if a bulk δ-NiMo compound phase wetted and penetrated along the Mo grain boundaries, a solid-state wetting experiment was performed using a Mo alloy with 12.5 at. % Ni. This Ni content will result in the formation of ~15 vol. % of δ-NiMo compound phase at the sintering temperature ($T$ = 1344 ºC and 1495 ºC). Ni (99.999%; Alfa) and Mo (99.999%; Alfa) powders were mixed in distilled de-ionized water and dried. The mixture was compacted in a die at 280 MPa to produce green specimen with ~

6.35 mm in diameter and 8~9 mm in height. Thereafter, specimen was presintered at 1100 ºC for 12 hours and then sintered at a predetermined temperature for 2 hours with flowing gas of Ar/5%$H_2$. The purpose of presintering was to homogenize the system and prevent the formation of transient liquid. The sintered specimens were polished and characterized with a Hitachi S-4800 SEM equipped with an Oxford EDX detector.

## 3.9 Grain Size Measurement

Grain size evolution of specimen was analyzed. The specimens were polished to mirror finish on emery papers and alumina slurries (diamond paste). Thereafter, they were etched at room-temperature with 30% volume hydrogen peroxide to make grain boundaries visible. The specific procedure for producing polished and etched samples for grain size analysis is described as follows:

1. A Buehler low speed diamond saw was used to cut discs from sintered Ni-Mo pellets.
2. The specimens were then roughly polished with emery papers of grit sizes of 240, 400, 600, 800, 1000 in a sequence (while always orienting the scratches normal to the direction of prior polishing).
3. Then, specimens were finely polished with alumina suspensions in water (or diamond pastes) to get a mirror finish.
4. The polished Ni-Mo specimens were etched at room-temperature using hydrogen peroxide for 45 second to 1 min.

A Hitachi S-4800 field emission SEM and Olympus optical microscope were used to measure the grain size of these Ni-Mo specimens.

## 3. 10 Powder Processing and Sintering of Mo-Si-B Alloys

The processing and sintering of Mo-Si-B alloy were similar to the common powder metallurgy methods. The only difference was that we start from silicon nitride and boron nitride powder instead of pure silicon or boron powder (to reduce the possibility of oxidation). The powders used in this experiment are listed in table 3.3. Two kinds of Mo powders with different average particle size were selected to examine the effect of particle size on sintering and grain growth.

Table 3.3 Raw materials of powders for preparing Mo-Si-B alloy

| Materials | Supplier | Particle size | Purity |
|---|---|---|---|
| Mo powder | Atlantic Equipment Engineer | 1-2 μm | 99.98% |
| Mo powder | Nanostructured and Amorphous Materials Inc | 85 nm | 99.5% |
| $Si_3N_4$ | Alfa | < 1 μm | 99.5% |
| BN | Cerac Incorporated | < 1 μm | 99.9% |

After mixing of Mo, $Si_3N_4$ and BN powders and pressing, the green pellets were subjected to a high-temperature reactive sintering process, where the following reactions occurred:

$3Mo + 1/3Si_3N_4 \rightarrow Mo_3Si$ (A15 phase) $+ 2/3N_2$ (g)

$5Mo + 1/3Si_3N_4 + 2BN \rightarrow Mo_5SiB_2$ (T2 phase) + $5/3N_2$ (g)

where the nitrides reacted with molybdenum to form A15 and T2 phases, which are labeled in ternary phase diagram of Mo-Si-B in Fig. 3.8.

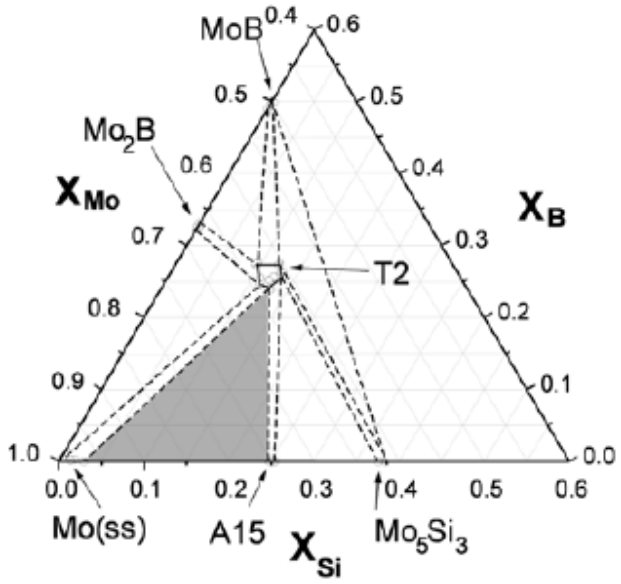


Figure 3.8 Ternary phase diagram of Mo-Si-B. A15 and T2 phases are labeled [11].

A homogenous mixture of the starting powders was critical to achieving a uniform dispersion of the intermetallic phases in the final microstructure. The detailed procedure of making sintered Mo-Si-B is described as follows:

1. The Mo, $Si_3N_4$ and BN powders were dry mixed with 3 wt. % of PMMA, Elvacite 2008 (Lucite International), which was added as a dispersant and binder, and 0.3 wt.% stearic acid, which was added as a powder lubricant (both PMMA and stearic acid burned out during firing).
2. The powder mixture was ball milled with $Si_3N_4$ media in $Si_3N_4$ grinding jar using a SPEX ball milling machine for 30 mins.

3. Then, the powders were press into cylindrical pellets of ~6.36 mm in diameter and 8~9 mm in height using 480 MPa pressure.
4. The specimens were sintered at the predetermined temperatures (1500-1600 ºC) for 6 to 12 hours with 3 ºC/min heating rate and spontaneous cooling.

References

[1] Wikipedia

[2] TB Massalski, H Okamoto. Binary Alloy Phase Diagrams, ASM International, Ohio., 1990.

[3] SL Kang. Sintering, Butterworth-Heinemann, 2004.

[4] DL Johnson. New method of obtaining volume, grain-boundary, surface diffusion coefficients from sintering data J.Appl.Phys. 40 (1969) 192.

[5] RM German, ZA Munir. Heterodiffusion model for the activated sintering of molybdenum Journal of the Less-Common Metals 58 (1978) 61.

[6] JL Johnson, RM German. Theoretical modeling of densification during activated solid-state sintering Metallurgical and Materials Transactions A (Physical Metallurgy and Materials Science) 27A (1996) 441.

[7] RL Coble. Sintering Crystalline Solids. I. Intermediate and Final State Diffusion Models J. App. Phys. 32 (1961) 787.

[8] WD Kingery. Densification during Sintering in the Presence of a Liquid Phase I. Theory Journal of Applied Physics 30 (1959) 301.

[9] RM German. Liquid Phase Sintering, Plenum Press, New York, 1985.

[10] RM German, P Suri, SJ Park. Review: Liquid phase sintering J.Mater.Sci. 44 (2009) 1.

[11] MR Middlemas, JK Cochran. Dense, fine-grain Mo-Si-B alloys from nitride-based reactions JOM 60 (2008) 19.

# CHAPTER FOUR

# GRAIN BOUNDARY DISORDERING IN DOPED TUNGSTEN

Part of this chapter has been published in:

"Grain Boundary Disordering in Binary Alloys," J. Luo and X. Shi, *Applied Physics Letters*, 92: 101901 (2008).

## 4.1 Motivations

In a classic review article in 1978 [1], Coble and Cannon stated that "the most significant changes which have been taken place in recent years regard the finding with respect to densification below the eutectics in numerous systems, notably tungsten-carbide:cobalt, tungsten:nickel, …" Although subsolidus activated sintering in doped refractory metal had been studied since early 1960's, the exact underlying mechanism remained controversial for decades. Recent high-resolution transmission electron microscopy (HRTEM) studies attributed subsolidus activated sintering in Ni-doped W, $Bi_2O_3$-doped ZnO [2] and other systems [3,4] to short-circuit diffusion in premelting-like IGFs. Subsolidus activated sintering experiments have been conducted for W using various dopants with significantly different effectiveness: Pd, Ni >Fe, Co, Ru > Cu [5,6], enabling a critical test of the hypothesized sintering mechanism. Moreover, using onset sintering as an indicator for GB disordering, we can establish a quantitative model for predicting GB disordering in binary alloys with broader implications beyond sintering.

This chapter describes our initial effort in developing a GB premelting/prewetting model based on the Miedema model and computational thermodynamics. This model quantitatively

explains the long-standing mystery of subsolidus activated sintering in five tungsten based binary alloys. This work represents the first step towards proposing a long-range scientific goal of developing GB "phase" diagrams as a new tool for materials science, and is the first successful example that demonstrates such GB diagrams can lead to quantitative predictions. Further refinements and in-depth discussion of relevant concepts and models are given in Chapter Six.

## 4.2 The Model

Five W alloys (W-M; M = Pd, Ni, Fe, Co and Cu) were selected for this study in part due to the availability of binary thermodynamic functions, which were developed via the CALPHAD (CALculation of PHAse Diagrams) effort [7,8,9,10]. Stabilization of a subsolidus quasi-liquid IGF of thickness *h* can be considered in terms of the free energy penalty for forming an undercooled liquid ($\Delta G_{\text{amorph.}} \cdot h$) being more than offset by the reduction in interfacial energies resulting from the replacement of a GB with two crystal-liquid interfaces as shown in Fig. 4.1:

$$\Delta G_{\text{amorph.}} \cdot h < (\gamma_{gb}^{(0)} - 2\gamma_{cl}) \equiv -\Delta\gamma, \qquad (4.1)$$

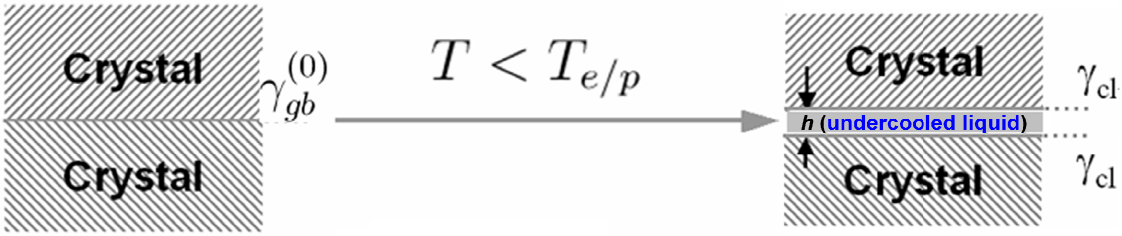


Figure 4.1 Basic principle of the stabilization of a liquid-like IGF at subsolidus temperature. Below the bulk *solidus line,* a nanometer-thick, quasi-liquid film can be stabilized at GBs; this can be conceptualized as the reduced interfacial energy ($\gamma_{gb}$ -2$\gamma_{cl}$) overcompensating for the increased free energy to form an undercooled liquid film ($\Delta G_{amorph} \cdot h$).

The average excess free energy of random W GBs without adsorption ( $\gamma_{gb}^{(0)}$ ) is interpolated from the data at 1773 K (1.08 J/m$^2$) [11] and 0 K (1.225 J/m$^2$) [12]. The crystal-liquid interfacial energies are estimated based on the Miedema model [12,13] and the data in Ref. [12]:

$$\gamma_{cl} = F_M^W(X_M) \cdot \frac{\Delta H_{\text{W in M}}^{\text{interface}}}{C_0 V_{\text{W}}^{2/3}} + \frac{H_{\text{W}}^{\text{fuse}}}{C_0 V_{\text{W}}^{2/3}} + \frac{1.9RT}{C_0 V_{\text{WM}}^{2/3}}, \quad (4.2)$$

where $\Delta H_{\text{W in M}}^{\text{interface}}$ is the enthalpy of solution; $X_{\text{M}}$ is the molar fraction of M in the liquid (IGF); $C_0$ is a constant ($\approx 4.5 \times 10^8$); $V$ is the molar volume; $R$ is the gas constant; and $F_M^W(X_M)$ is the degree to which W atoms are surrounded by M atoms [13].

The value of $\Delta G_{\text{amorph.}}$ can be computed from the liquid formation free energy and the chemical potentials set by the equilibrium bulk phase(s) via standard CALPHAD methods (Fig. 4.2):

$$\Delta G_{\text{amorph.}} = G_{\text{liquid}}^f - [X_M \mu_M + (1 - X_M)\mu_W]. \quad (4.3)$$

Relevant bulk thermodynamic terms are calculated using the thermodynamic functions (as shown in Table 4.1) in refs.[7,8,9,10,14].

Table 4.1 Binary thermodynamic functions used in the calculations. Thermodynamic functions for W-Ni, W-Co, and W-Fe [7,8,9,10] have been fully assessed (being included in the Scientific Group Thermodata Europe or SGTE binary alloy database). In addition, (less reliable) thermodynamic functions have been derived for W-Pd based on partial phase-diagram data [14]. Formation free energies of unary phases are taken from the SGTE unary database [15,16] for the first three systems and from ref. [17] for W-Pd. $\Delta S_{conf.} = -R[X \ln X_W + X_M \ln X_M]$ is the configuration entropy.

| | Phase | Gibbs free energy (J·mol$^{-1}$) | Ref. |
|---|---|---|---|
| W-Ni | Liquid | $X_{Ni}\,{}^oG_{Ni}^{liq} + X_W\,{}^oG_W^{liq} - T\Delta S_{conf.} + X_{Ni}X_W[16290 - 10.25T - 22450(X_{Ni} - X_W)]$ | [9] |
| | BCC | $X_{Ni}\,{}^oG_{Ni}^{bcc} + X_W\,{}^oG_W^{bcc} - T\Delta S_{conf.} + X_{Ni}X_W(78432)$ | |
| | FCC | $X_{Ni}\,{}^oG_{Ni}^{fcc} + X_W\,{}^oG_W^{fcc} - T\Delta S_{conf.} + X_{Ni}X_W[2556 + 11.6T - 52900(X_{Ni} - X_W)] + G_{mag.}$ | |
| | $\frac{1}{5}Ni_4W$ | $\frac{4}{5}{}^oG_{Ni}^{fcc} + \frac{1}{5}{}^oG_W^{bcc} - 2572.4 - 0.9494T$ | |
| | $\frac{1}{2}$ NiW | $\frac{1}{2}{}^oG_{Ni}^{fcc} + \frac{1}{2}{}^oG_W^{bcc} - 4442.95 + 1.5T$ | |
| | $\frac{1}{3}NiW_2$ | $\frac{1}{3}{}^oG_{Ni}^{fcc} + \frac{2}{3}{}^oG_W^{bcc} - 29630.2 + T$ | |
| W-Co | Liquid | $X_{Co}\,{}^oG_{Co}^{liq} + X_W\,{}^oG_W^{liq} - T\Delta S_{conf.} + X_{Co}X_W(-42606.6 + 15.5064T)$ | [10] |
| | BCC | $X_{Co}\,{}^oG_{Co}^{bcc} + X_W\,{}^oG_W^{bcc} - T\Delta S_{conf.} + X_{Co}X_W(54648)$ | |
| | FCC | $X_{Co}\,{}^oG_{Co}^{fcc} + X_W\,{}^oG_W^{fcc} - T\Delta S_{conf.} + X_{Co}X_W[-13038 + 8.038T - 11832(X_{Co} - X_W)]$ | |
| | $\frac{1}{13}Co_6W_7$ | $\frac{6}{13}{}^oG_{Co}^{fcc} + \frac{7}{13}{}^oG_W^{bcc} - 3796.9 - 0.6526T$ | |
| W-Fe | Liquid | $X_{Fe}\,{}^oG_{Fe}^{liq} + X_W\,{}^oG_W^{liq} - T\Delta S_{conf.} + X_{Fe}X_W[-3607 + 5.65T - 5450(X_{Fe} - X_W)]$ | [7,8] |
| | BCC | $X_{Fe}\,{}^oG_{Fe}^{bcc} + X_W\,{}^oG_W^{bcc} - T\Delta S_{conf.} + X_{Fe}X_W[41544 - 12621(X_{Fe} - X_W)] + G_{mag.}$ | |
| | FCC | $X_{Fe}\,{}^oG_{Fe}^{fcc} + X_W\,{}^oG_W^{fcc} - T\Delta S_{conf.} + X_{Fe}X_W[25977 - 3.36T - 7258.6(X_{Fe} - X_W)] + G_{mag.}$ | |
| | μ-phase | $y_{Fe}^3\,{}^oG_{Fe:W:Fe}^{\mu} + y_W^3\,{}^oG_{Fe:W:W}^{\mu} + 4(y_{Fe}^3 \ln y_{Fe}^3 + y_W^3 \ln y_W^3)$<br>where: $y_{Fe}^3$ and $y_W^3$ are the site fraction of element Fe and W on sublattice 3.<br>${}^oG_{Fe:W:Fe}^{\mu} = (7\,{}^oG_{Fe}^{fcc} + 2\,{}^oG_W^{bcc} + 4\,{}^oG_{Fe}^{bcc} - 14300 + 26.7T)/13$<br>${}^oG_{Fe:W:W}^{\mu} = (7\,{}^oG_{Fe}^{fcc} + 2\,{}^oG_W^{bcc} + 4\,{}^oG_W^{bcc} - 53450 + 19T)/13$ | |
| | $\frac{1}{3}Fe_2W$ | $\frac{2}{3}{}^oG_{Fe}^{fcc} + \frac{1}{3}{}^oG_W^{bcc} - 4500 + 1.66667T$ | |
| W-Pd | Liquid | $X_{Pd}\,{}^oG_{Pd}^{liq} + X_W\,{}^oG_W^{liq} - T\Delta S_{conf.} + X_{Pd}X_W(13868.7 + 10.9322T)$ | [14] |
| | BCC | $X_{Pd}\,{}^oG_{Pd}^{bcc} + X_W\,{}^oG_W^{bcc} - T\Delta S_{conf.} + X_{Pd}X_W(9386.8 + 14.6329T)$ | |
| | FCC | $X_{Pd}\,{}^oG_{Pd}^{fcc} + X_W\,{}^oG_W^{fcc} - T\Delta S_{conf.} + X_{Pd}X_W(-13144 + 16.6866T)$ | |

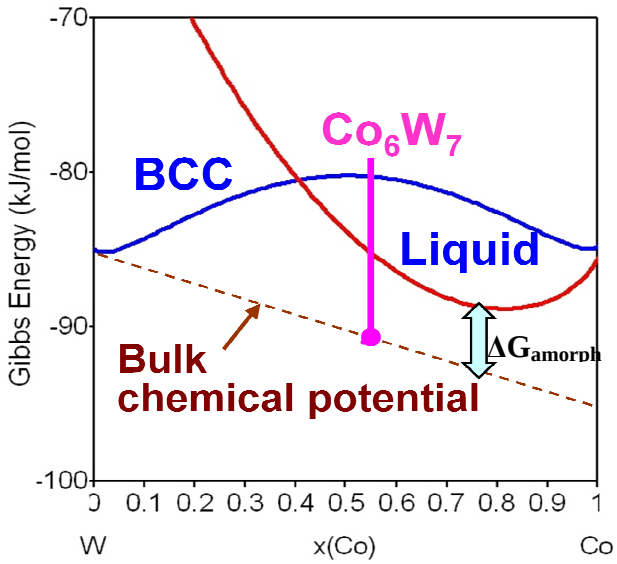


Figure 4.2 Calculated free energies in the W-Co binary system at 1400 °C. The volumetric free energy for amorphization ( $\Delta G_{\text{amorph.}}$ ) is labeled.

We define the following variable to represent the thermodynamic tendency to stabilize a quasi-liquid IGF:

$$\lambda \equiv \underset{(0<X_m<1)}{\text{Max}}\left\{\frac{-\Delta\gamma(X_M)}{\Delta G_{amorph}(X_M)}\right\}, \tag{4.4}$$

which scales the film thickness. Further discussion of this thermodynamic variable ($\lambda$) and derivatives variables can be found in Chapter Six.

Furthermore, the excess free energy of a quasi-liquid IGF can be written as [18]

$$G^x - \gamma_{gb}^{(0)} = \Delta G_{\text{amorph.}} \cdot h + \Delta\gamma \cdot f(h), \tag{4.5}$$

where $f(h)$ is an interfacial coefficient that ranges from 0 to 1 as $h$ increases from 0 to ∞, and $\sigma_{\text{interfacial}}(h) \equiv \Delta\gamma \cdot [f(h) - 1]$ is a short-range interfacial interaction[18]. The equilibrium thickness ( $h_{EQ}$ ) is determined by minimizing Eq. (4.5). If a continuum approximation can be adopted,

$$f(h) \approx 1 - e^{-h/\xi} \tag{4.6}$$

and $h_{EQ} \approx \xi \cdot \ln(\lambda/\xi)$, where $\xi$ is a coherent length of ~0.3 nm[18,19]. Then, we estimate the range of GB solidus temperature ($T_{\mathrm{GBS}}$) via:

$$0.5 \text{ nm} < \lambda(T_{\mathrm{GBS}}) < 1 \text{ nm}. \tag{4.7}$$

At $T_{\mathrm{GBS}}$, $h_{EQ}$ is about one monolayer (0.2-0.3 nm) from extrapolation of the continuum approximation.

## 4.3 Model Prediction and Comparisons with Experiments

The $\lambda$ values are computed numerically as functions of the bulk chemical potentials and temperature using a homemade MATLAB code. Lines of constant $\lambda$ are plotted in bulk binary phase diagrams, and one example is shown in Fig. 4.3. At a constant temperature, $\lambda$ is constant in the two-phase region and decreases with decreasing dopant concentration in the single-phase region. Consistently, it is well known that additional doping beyond optimal levels (which are typically slightly above the solid solubility limits) does not provide additional benefits to enhance sintering [5,6,20]. Lines of constant $\lambda$ are also plotted in other W-M bulk binary phase diagrams, and a few other examples are shown in Fig. 4.4

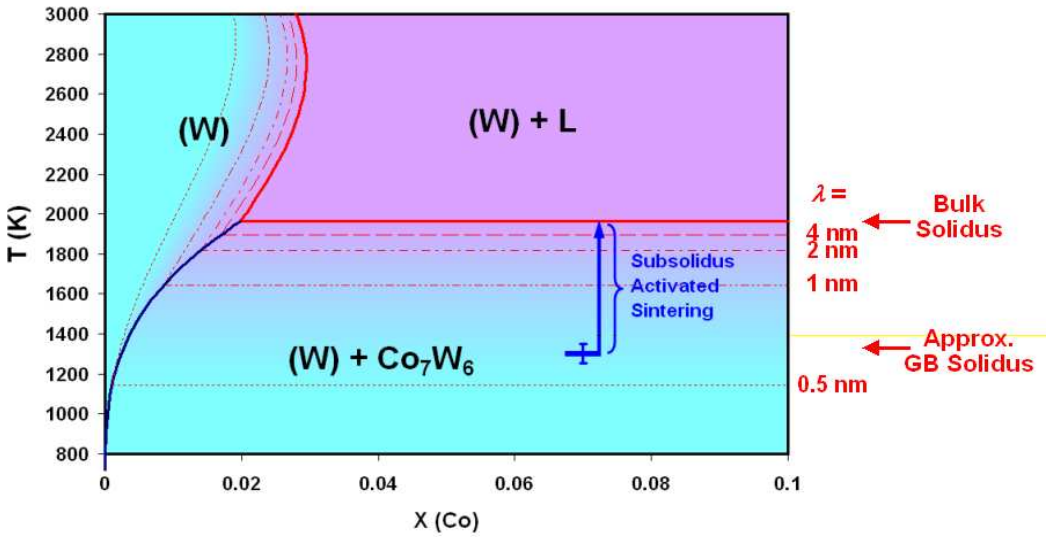


Figure 4.3 Computed lines of constant $\lambda$ are plotted in the W-Co binary bulk phase diagram. Computed diagrams for W-Fe, W-Pd and W-Ni exhibit similar features.

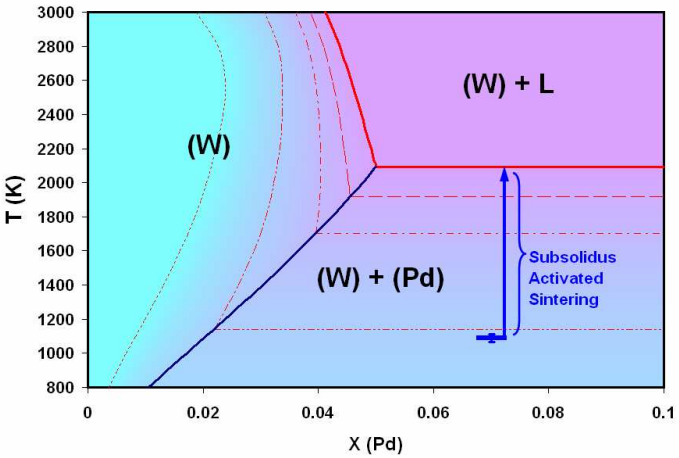


**(a)**

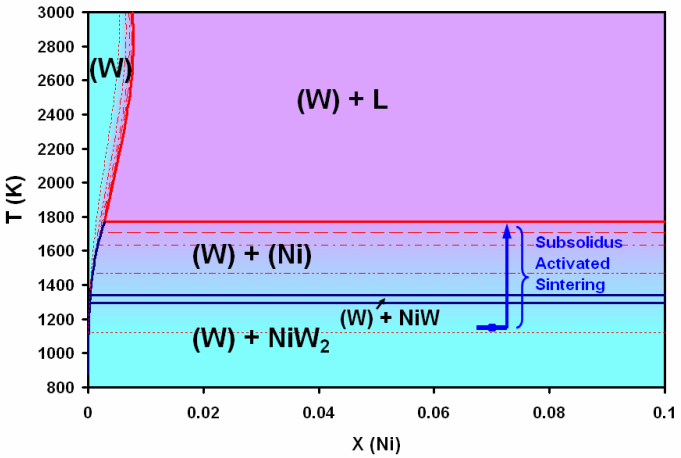


**(b)**

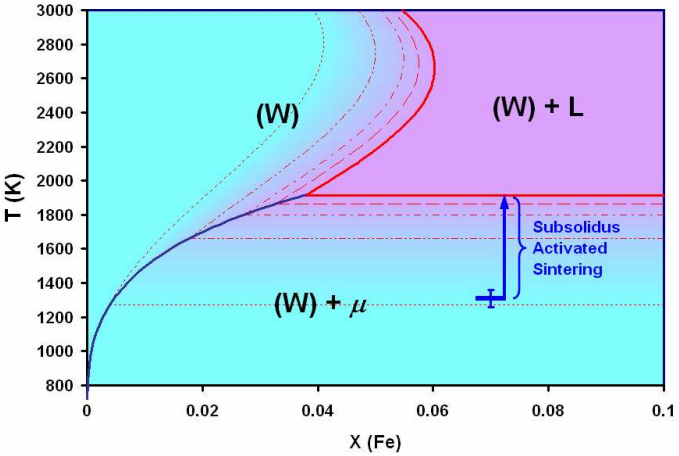


**(c)**

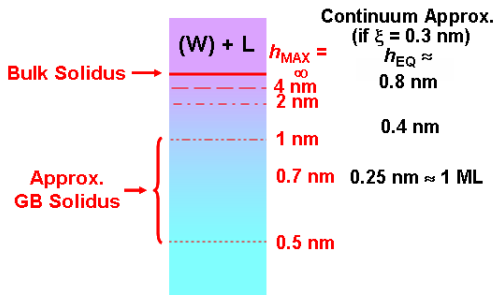


Figure 4.4 Computed lines of constant $h_{MAX}$ are plotted in the binary bulk phase diagrams for (a) W-Pd, (b) W-Ni, and (c) W-Fe.

Subsequently, computed $\lambda(T)$ values for dopant-saturated W specimens (in the two-phase regions) are shown in Fig. 4.5, which predicts the correct order for the dopant effectiveness (Pd > Ni > Co ≈ Fe >> Cu) [5,6]. Furthermore, $\lambda(T)$ can be used to rationalize detailed observations. For example, Pd is the most effective dopant at low temperatures, but Ni becomes more effective at moderate temperatures (inset in Fig. 4.3[6]); this observation can be explained from the different slopes in $\lambda(T)$ (Fig. 4.5).

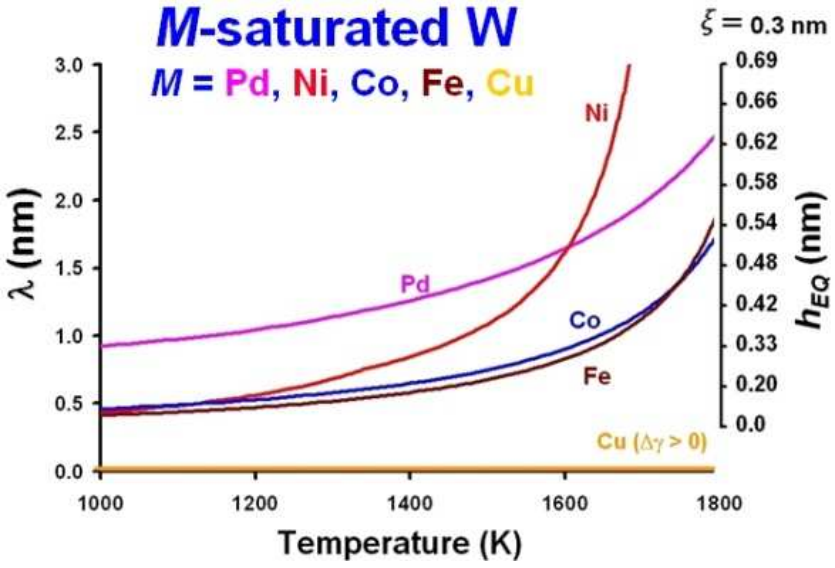


(a)

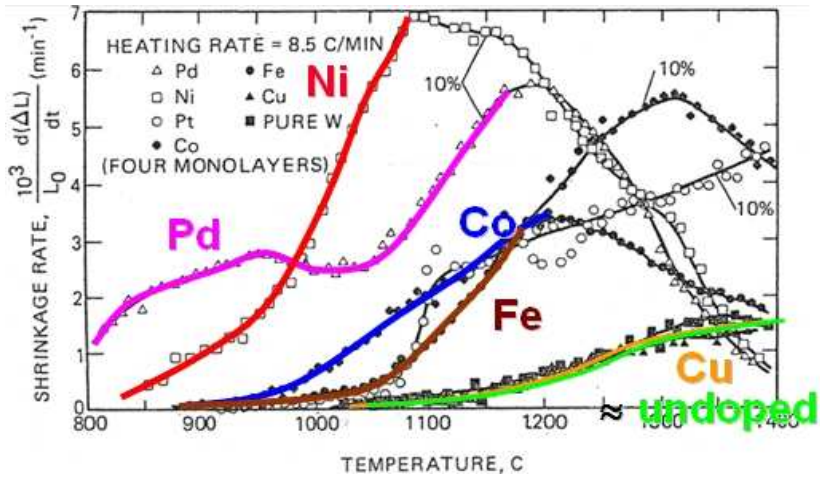


(b)

Figure 4.5 (a) Computed $\lambda$ vs. $T$ for dopant-saturated W specimens. Corresponding equilibrium film thicknesses are computed from a continuum approximation. (b) The $T$-dependent densification rates (re-plotted after Fig. 5 in ref.[21]; including only initial-stage sintering data).

To conduct a critical model-experimental comparison, onset activated sintering temperatures were retrieved from prior studies [5,6] and reprocessed to remove variations

due to the different sintering schemes and grain sizes. For GB-controlled sintering, it is known that $s^2 ds/dt \propto D_{GB} \cdot G^{-4}$, where $s$ is the linear shrinkage, $D_{GB}$ is the GB diffusivity, and $G$ is the grain size. The onset activated sintering temperature is defined as the temperature at which $s^2 ds/dt = 10^{-8}\,\text{min}^{-1}$ for a reference grain size of 0.56 μm[5], which corresponds to $s$ = 1% after 33 minutes of isothermal sintering.

Table 4.2 Activated sintering data retrieved from prior experiments [5,6] and relevant model predictions. The $\Delta\gamma_{e/p}$ values were computed by using the eutectic/peritectic temperature ($T_{e/p}$) and composition.

| | $T_{e/p}$ (K) | $\Delta\gamma_{e/p}$ (J/m$^2$) | Onset Activated Sintering $T_{sinter}$ (K) | | | | $\lambda(T_{sinter})$ (nm) | Estimated $T_{GBS}$ (K) |
|---|---|---|---|---|---|---|---|---|
| | | | #1[a] | #2[b] | #3[b] | Mean (STD) | | |
| W-Pd | 2088 | -0.60 | 1075 | 1079 | 1117 | 1090 (23) | 0.97[c] | < 1141[c] |
| W-Ni | 1768 | -0.52 | 1130 | 1160 | 1161 | 1150 (18) | 0.52 | 1121-1470 |
| W-Co | 1962 | -0.40 | 1355 | 1259 | 1290 | 1301 (49) | 0.58 | 1140-1644 |
| W-Fe | 1910 | -0.37 | 1333 | 1340 | 1250 | 1308 (50) | 0.52 | 1273-1664 |
| W-Cu | 1357 | +0.49 | No activated sintering | | | | No IGF ($\Delta\gamma > 0$) | |

[a] Data set #1 was extrapolated from the isothermal sintering data[6,22].

[b] Data sets #2 and #3 were retrieved from continuous sintering experiments of 8.5 and 17 °C/min, where the original data [11] were numerically reprocessed to obtain $s^2 ds/dt$.

[c] The thermodynamic functions for the W-Pd were derived based on partial data (less reliable)[14].

As shown in Table 4.2, the normalized onset sintering temperatures fall into the estimated ranges of $T_{GBS}$ for W-Pd, W-Ni, W-Co and W-Fe, which are ~60-85% of the

bulk eutectic/peritectic temperatures ($T_{e/p}$). On the other hand, computed $\Delta\gamma$ is > 0 for W-Cu, indicating that IGFs cannot form. This predication is consistent with the observation that Cu has no effect in enhancing sintering at all temperatures (Fig. 2) [6], even if this binary system has the lowest $T_{e/p}$ (Table 4.1).

## 4.4 A Model for Discrete Grain Boundary Complexions?

Recently, Tang *et al.* suggested an extension of the Gibbs definition of bulk phases to equilibrium GB features and designated them as *GB complexions* [19,23]. These subsolidus quasi-liquid IGFs are one important GB complexion that is a precursor to the bulk liquid phase. Notably, Dillon and Harmer recently observed a series of GB complexions in doped $Al_2O_3$ with increasing levels of structural disorder and GB mobility, and their study explained the mechanism of abnormal grain growth (another outstanding scientific mystery)[19,24]. To interpret their observations, Eq. (4.6) is refined to consider the finite atom size:

$$f(h) \approx 1 - e^{-h/\xi}[1 - \delta \sin^2(\pi h/\sigma_0)], \tag{4.8}$$

where $\sigma_0 \approx 0.25\,\text{nm}$ is the inter-atomic distance. Eq. (4.8) includes a well-known oscillatory structural force [25], producing local energy minima at $h = n\sigma_0$ ($n$ is an integer). This refinement leads to layering transitions [25,26] for moderate $\delta$ and produces a series of GB complexions (Fig. 4.5) similar to those observed by Dillon and Harmer[19,24].

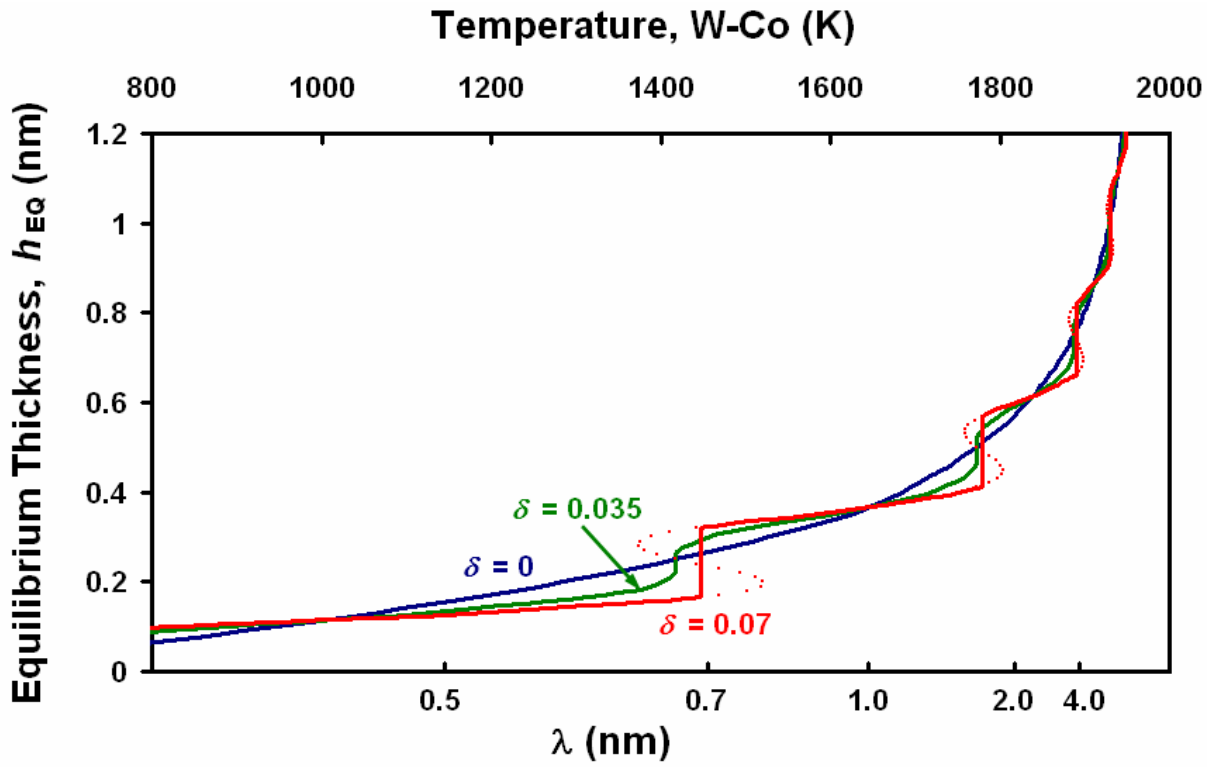


Figure 4.6 (Color online) Computed equilibrium film thickness vs. $\lambda$ [Eq. (4.8); $\xi$ = 0.3 nm]. Corresponding temperatures are computed for the W-Co system. Layering transitions occur for $\delta > 3.5\%$, leading to a series of GB complexions similar to those observed by Dillon and Harmer [24,26].

The current model can be extended to multicomponent alloys via the use of well-established CALPHAD extrapolation methods and statistical thermodynamic models for estimating interfacial energies. This model for metals serves as a basis for developing models for ceramics, where London dispersion forces and electrostatic interactions should be added separately [18]. To accurately represent interfacial forces, additional coarse-grained parameters, e.g., the average film composition ($X$) and structural order ($\eta$), can be included in the interfacial coefficient [ $f(h, X, \eta)$ ] in Eq. (4.6), which can in

principle produce many different types of GB complexions and transitions. A further extension of this model should consider structural and chemical gradients in a diffuse-interface theory [23].

## 4.4 Summary and Discussion

In summary, a quantitative GB disordering model (with no adjustable parameters) can explain all major observations of subsolidus activated sintering. In conjunction with recent direct HRTEM observations [20,27], it is concluded that subsolidus activated sintering is due to short-circuit diffusion in premelting-like IGFs. Moreover, this model can have broad applications beyond activated sintering, e.g., in understanding creep and liquid metal embrittlement [18].

This study represents an initial step towards a long-range scientific goal of developing quantitative GB complexion (phase) diagrams as fundamental information leading to controlled materials design. Because GB disordering or transitions can vastly change GB diffusivity and mobility, Fig. 4.2 or more sophisticated GB complexion diagrams (which may include first-order GB transitions [23]) can be used to design fabrication pathways to utilize desired GB structures during processing to control microstructural evolution. This study shows that bulk phase diagrams are not adequate for predicting optimal activated sintering protocols since liquid-like GB complexions can form at ~60-85% of bulk solidus temperatures, resulting in subsolidus activated sintering phenomena that is parallel to liquid-phase sintering. Since IGFs or other GB

complexions can be retained upon cooling and critically affect a variety of mechanical and physical properties [18], GB complexion diagrams can also be used to devise heat treatment recipes to adjust final GB structures for the desired properties.

References

[1] RL Coble, RM Cannon. Current Paradigms in Powder Processing (1978) 151.

[2] J Luo, H Wang, Y- Chiang. Origin of Solid State Activated Sintering in Bi2O3-Doped ZnO Journal of the American Ceramic Society 82 (1999) 916.

[3] E Jud, Z Zhang, W Sigle, LJ Gauckler. Microstructure of Cobalt Oxide Doped Sintered Ceria Solid Solutions Journal of Electroceramics 16 (2006) 191.

[4] Z Zhang, W Sigle, M Ruhle, E Jud, LJ Gauckler. Microstructure characterization of a cobalt-oxide-doped cerium-gadolinium-oxide by analytical and high-resolution TEM Acta Materialia 55 (2007) 2907.

[5] HW Hayden, JH Brophy. Activated Sintering of Tungsten with Group VIII Elements Journal of Electrochemcial Society 110 (1963) 805.

[6] RM German, ZM Munir. Enhanced Low-Temperature Sintering of Tungsten Metallurgical Transactions 7A (1976) 1873.

[7] P Gustafson. THERMODYNAMIC EVALUATION OF THE C-Mo-W SYSTEM Zeitschrift fuer Metallkunde/Materials Research and Advanced Techniques 79 (1988) 397.

[8] P Gustafson. THERMODYNAMIC EVALUATION OF THE C-Fe-W SYSTEM Metallurgical transactions.A, Physical metallurgy and materials science 18 A (1987) 175.

[9] P Gustafson, A Gabriel, I Ansara. THERMODYNAMIC EVALUATION OF THE C-Ni-W SYSTEM Zeitschrift fuer Metallkunde/Materials Research and Advanced Techniques 78 (1987) 151.

[10] AF Guillermet. Thermodynamic properties of the Co-W-C system Metallurgical Transactions A (Physical Metallurgy and Materials Science) 20A (1989) 935.

[11] EN Hodkin, MG Nicholas, DM Poole. The Surface Energies of Solid Molybdenum, Niobium, Tantalum, and Tungsten Journal of Less-Common Metals 20 (1970) 93.

[12] FR de Boer, R Boom, WCM Mattens, AR Miedema, AK Niessen. *Cohesion in Metals: Transition Metals Alloys*, North-Holland, Amsterdam, 1988.

[13] R Benedictus, A Böttger, EJ Mittemijer. Thermodynamic Model for Solid-State Amorphization in Binary Systems at Interfaces and Grain Boundaries Physical Review B 54 (1996) 9109.

[14] KL Seh, NL Dong. Calculation of phase diagrams using partial phase diagram data Calphad 10 (1986) 61.

[15] DR Lide. STGE Unary Database 2009

[16] EDR Lide. CRC Handbook of Chemistry and Physics

[17] L Kaufman, H Bernstein. Computer Calculation of Phase Diagrams with Special Reference to Refractory Metals, Academic Press, New York, 1970.

[18] J Luo. Stabilization of Nanoscale Quasi-Liquid Interfacial Films in Inorganic Materials: A Review and Critical Assessment Critical Reviews in Solid State and Material Sciences 32 (2007) 67.

[19] SJ Dillon, MP Harmer. Multiple Grain Boundary Transitions in Ceramics: A Case Study of Alumnia Acta Materialia 55 (2007) 5247.

[20] VK Gupta, DH Yoon, HM Meyer III, J Luo. Thin Intergranular Films and Solid-State Activated Sintering in Nickel-Doped Tungsten Acta Materialia 55 (2007) 3131.

[21] GA Lopez, EJ Mittemeijer, BB Straumal. Grain boundary wetting by a solid phase; microstructural development in a Zn-5 wt% Al alloy Acta Materialia 52 (2004) 4537.

[22] AP Prill, WW Hayden, JH Brophy. The Role of Phase Relations in Activated Sintering of Tungsten Transaction of American Institute of Mining Engineers 230 (1964) 769.

[23] M Tang, WC Carter, RM Cannon. Grain Boundary Transitions in Binary Alloys Physical Review Letters 97 (2006) 075502.

[24] SJ Dillon, M Tang, WC Carter, MP Harmer. Complexion: a new concept for kinetic engineering in materials science Acta Materialia 55 (2007) 6208.

[25] JN Israelachvili. Intermolecular and Surface Forces, Academic Press Limited, London, 1994.

[26] SJ Dillon, MP Harmer. Multiple grain boundary transitions in ceramics: a case study of alumina Acta Materialia 55 (2007) 5247.

[27] J Luo, VK Gupta, DH Yoon, HM Meyer. Segregation-Induced Grain Boundary Premelting in Nickel-doped Tungsten Applied Physics Letters 87 (2005) 231902.

# CHAPTER FIVE

# GRAIN BOUNDARY WETTING AND PREWETTING IN NI-DOPED MO

Part of this chapter has been published in

"Grain Boundary Wetting and Prewetting in Ni-Doped Mo," X. Shi and J. Luo, *Applied Physics Letters*, 94: 251908 (2009).

## 5.1 Motivations

As discussed in Chapter 2, impurity-based intergranular films (IGFs), which are ubiquitous in ceramic materials, often control sintering, grain growth and various mechanical and physical properties.[1] In a generalized Cahn wetting model, Tang, Carter and Cannon proposed that subsolidus IGFs could form from coupled grain boundary (GB) prewetting and premelting transitions.[2,3] Although GB premelting and prewetting in metals have been extensively investigated by Straumal and co-workers [4], high-resolution transmission electron microscopy (HRTEM) studies are rare. The only exception is a recent HRTEM study of Ni-doped W, which found stable quasi-liquid IGFs in the sub-eutectic two-phase region [5,6]. Although GB prewetting transitions in Bi-Cu and Fe-Si-Zn have been indicated by GB chemistry and diffusion measurements [4], direct HRTEM observation of quasi-liquid IGFs in the single-phase region has not

been made for any metallic system.

GB wetting and prewetting in the Mo-Ni system are practically important for understanding its sintering and embrittlement properties [7,8]. Two prior studies found nanometer-thick layers of crystalline δ-NiMo at Mo GBs and inferred a solid-state complete GB wetting.[7,8] However, it is unknown whether these compound layers could indeed exhibit arbitrary thickness as being expected for a case of complete wetting and whether they were in fact disordered at the firing temperatures.

This chapter reports thermodynamic modeling and critical experiments about Mo-Ni systems to clarify the existing controversy about GB wetting, and to seek direct HRTEM evidence for the stabilization of quasi-liquid IGFs in the single-phase region of a binary metallic system to critically support prewetting theories [2,4,9].

## 5.2 Grain Boundary Wetting and Non-Wetting

We adopt a Miedema type model that was elaborated by Benedictus et al. to evaluate relevant interfacial energies [10]. The average excess energy for a crystal-crystal interface between Mo (BCC) and δ-NiMo is estimated as:

$$\gamma_{cc} \approx \frac{\gamma^{s}_{Mo} + \gamma^{s}_{MoNi}}{6} + \frac{F^{Mo}_{Ni}\,\Delta H^{\text{interface}}_{\text{Mo in Ni}}}{C_0 V^{2/3}_{\text{Mo}}} \approx 0.90\ \text{J/m}^2, \qquad (5.1)$$

where surface energies $\gamma^{s}_{Mo}$ and $\gamma^{s}_{MoNi}$ are evaluated using the Miedema model (Eq. 7a and Eq. 11b in Ref. [10]; neglecting the entropic contribution); $\Delta H^{\text{int}}$ is the enthalpy of

solution; $C_0 \approx 4.5 \times 10^8$; $V$ is the molar volume (neglecting thermal expansion); R is the gas constant; and $F_{Ni}^{Mo}$ is the surface fraction of Ni atoms of δ-NiMo. The first term of Eq. 5.1 represents contribution due to the mismatch between two kinds of crystalline structures; and second term represents excess interfacial energy due to the interaction between two crystals with different composition.

Furthermore, the average energy of random GBs in pure Mo is estimated as: $\gamma_{gb}^{(0)} \approx 1/3 \cdot \gamma_{Mo}^{s} \approx$ 1.0 J/m$^2$. In a Ni-doped specimen, the actual GB energy ($\gamma_{gb}$) is less than $\gamma_{gb}^{(0)}$, because Ni adsorption (including the formation of an IGF) reduces GB energy according to the Gibbs adsorption isothermal. Since $2\gamma_{cc} > \gamma_{gb}^{(0)} > \gamma_{gb}$, complete GB wetting cannot occur in the solid-state generally. The average dihedral angle is estimated based on the Young equation as:

$$\phi = 2\arccos\left(\frac{\gamma_{gb}}{2\gamma_{cc}}\right) > 2\arccos\left(\frac{\gamma_{gb}^{(0)}}{2\gamma_{cc}}\right) \approx 112^\circ . \qquad (5.2)$$

For specimens quenched from 1344 °C (with two equilibrium phases of Mo-rich BCC and δ-NiMo), the average measured dihedral angles on 2-D sections (which should be equal to the average true 3-D dihedral angle in theory [11]) is 105° with a standard deviation of 11°. This result reasonably agrees with Eq. (5.2) , thereby supporting the validity of the Benedictus et al.'s equations [10]. Fig. 5.1 shows comparison of experiments-measured value and theoretically-calculated value of dihedral angle. In summary, it can be unequivocally concluded that δ-NiMo does not wet Mo GBs, which is directly shown in Fig. 5.2.

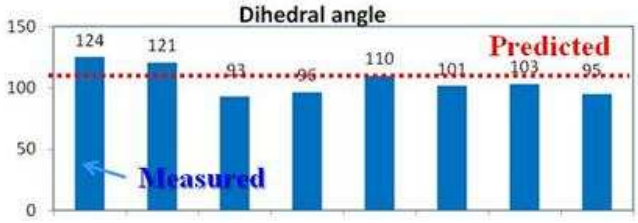


Figure 5.1 Comparison of measured value and theoretically-predicted value of dihedral angle.

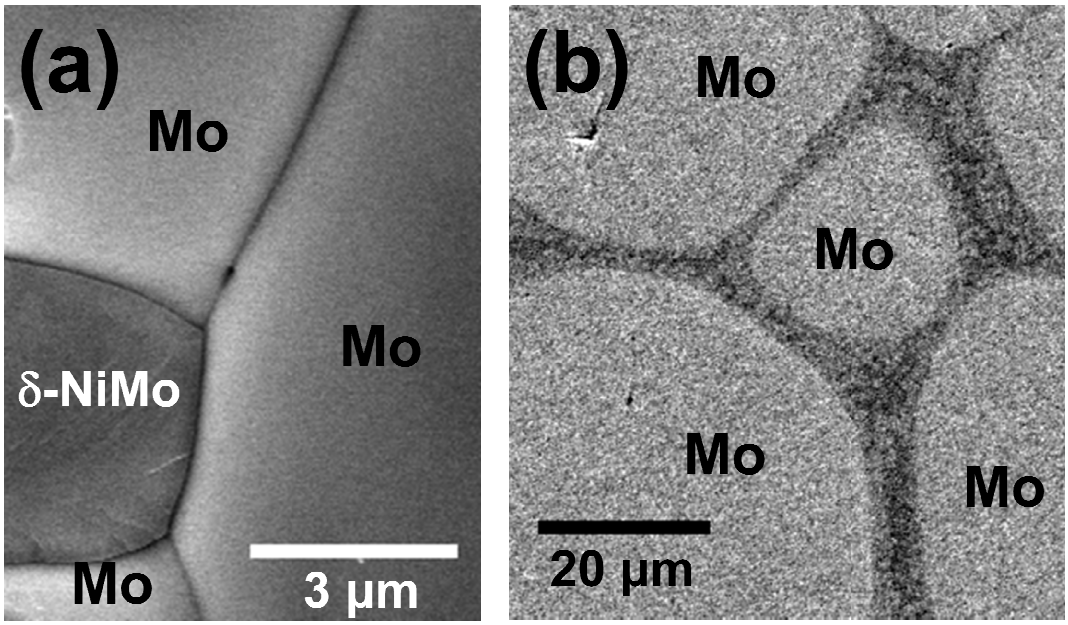


Figure 5.2 (a) An SEM image of a fractured Mo + 12.4 at. % Ni specimen quenched from 1344 ° C shows that δ-NiMo phase does not wet Mo GBs in the solid state. (b) A cross-sectional SEM image of a Mo + 12.4 at. % Ni specimen quenched from 1495 °C shows that the Ni-rich liquid phase completely wets Mo GBs.

In the solid-liquid two-phase regime, the crystal-liquid interfacial energy is

estimated as [10]:

$$\gamma_{cl} \approx \frac{H_{\text{Mo}}^{\text{fuse}}}{C_0 V_{Mo}^{2/3}} + \frac{\Delta H_{\text{Mo in Ni}}^{\text{interface}} \cdot F_{Ni}^{Mo}}{C_0 V_{Mo}^{2/3}} + \frac{1.9RT}{C_0 V_{Mo/Ni}^{2/3}} = (0.138 - 0.160 F_{Ni}^{Mo} + 8.92\times10^{-5} T)\ \text{J/m}^2, \quad (5.3)$$

Where it is comprised of three terms including enthalpic contribution, interaction contribution and entropic contribution respectively from left to right; $H_{Mo}^{fuse}$ is the fusion enthalpy, and $F_{Ni}^{Mo}$ represents the fraction of Ni-Mo bonds at the interface. We calculated it using Eq. 5.4 adapted from Ref. [10]

$$F_{Ni}^{Mo} = C_{Ni}^{s} \equiv \frac{X_{Ni} V_{Ni}^{2/3}}{(1 - X_{Ni}) V_{Ni}^{2/3} + X_{Ni} V_{Ni}^{2/3}} \quad (5.4)$$

We assumed that liquid-like IGF adopted the liquidus composition, $X_{\text{Ni}} = X_{\text{L}}$. Then, $\gamma_{cl}$ is calculated to be 0.211 J/m$^2$ at 1362 °C (= $T_{\text{peritectic}}$) and 0.231 J/m$^2$ at 1495 °C. Since $2\gamma_{cl} < \gamma_{gb}^{(0)} \approx 1.0$ J/m$^2$, complete wetting of Mo GBs by the Ni-rich liquid is generally expected (although this is neither a sufficient condition nor applicable to coincident GBs with low $\gamma_{gb}^{(0)}$). Complete GB wetting in the solid-liquid regime had been confirmed by characterizing quenched specimens, and one example is shown in Fig. 5.1b.

## 5.2 Prewetting and Premelting in Single Phase Regime

In the single-phase (Mo-rich BCC phase) region, there is a free energy penalty ($\Delta G_{\text{amorph}}$) for forming the meta-stable liquid phase. Nonetheless, a quasi-liquid IGF of thickness *h* can be thermodynamically stable if this free energy penalty is more than

offset by the reduction in interfacial energies when a GB is replaced with two crystal-liquid interfaces:

$$\Delta G_{amorph} \cdot h < \gamma_{GB}^{(0)} - 2\gamma_{cl} \equiv -\Delta\gamma. \quad (5.5)$$

At 1495 °C, $-\Delta\gamma$ is estimated to be 0.54 J/m$^2$. Consequently, nanoscale GB wetting can occur when the (liquid) phase that does the wetting is not yet a stable bulk phase, which is a prewetting phenomenon [12].

As we will discuss in Chapter 6, we define $\lambda_L$ to represent the maximum thickness of a stable quasi-liquid IGF of the liquidus composition $X_L$ (without interfacial forces), as:

$$\lambda_L \equiv -\Delta\gamma / \Delta G_{\text{amorph}} . \quad (5.6)$$

It should be noted that $\lambda_L$ defined here is slightly different from the $\lambda$ defined in Chapter 4, Refs. [13,14] in that the IGF is assumed to adopt the liquidus composition. This assumption allows us to compute $\lambda_L$ values analytically. Further discussion about these thermodynamic parameters can be found in Chapter Six.

Fig. 5.3 shows computed $\lambda_L$ vs. bulk Ni fraction at 1495 ° C ($X_S$ = 0.0189 and $X_L$ = 0.5802, calculated with the thermodynamic functions in Ref. 16). Dotted lines in Fig. 2 bound the range of computed $\lambda_L$'s for random GBs assuming ± 30% variations in $\gamma_{gb}^{(0)}$. The actual equilibrium film thickness, which depends on the unknown interfacial forces, should scale (but is typically not identical to) the computed $\lambda_L$ [13,14]. Furthermore, as we have discussed in the prior chapter, discrete jumps in film thickness may arise from a first-order prewetting transition [2] or a finite atomic size effect[13,14], producing

discrete GB complexions (phases) similar to those observed by Dillon and Harmer [15].

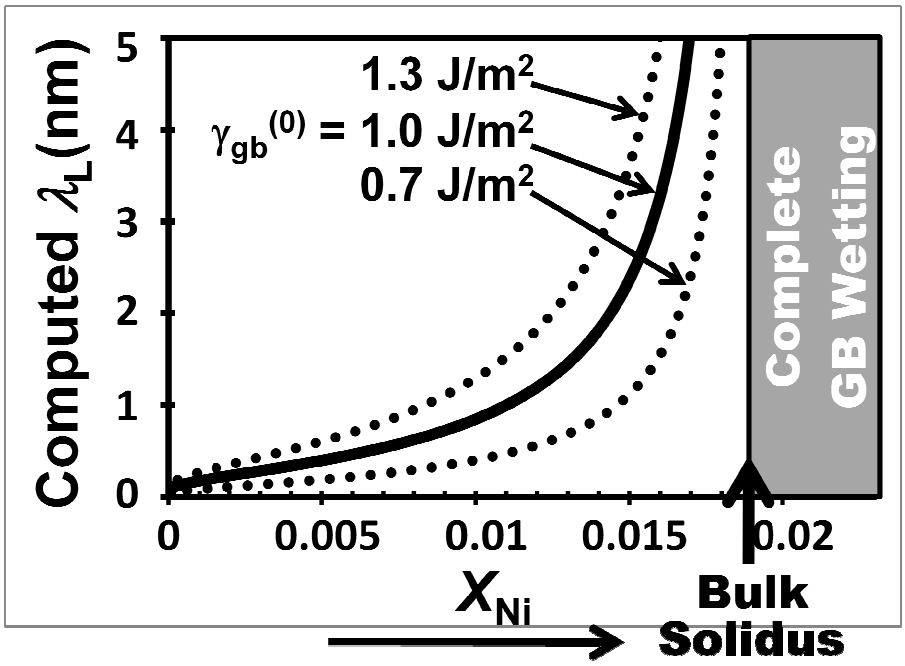


Figure 5.3 Computed $\lambda_L$ vs. Ni atomic fraction at 1495 ºC. The computed $\lambda_L$ value represents the maximum thickness of a stable quasi-liquid IGF of liquidus composition ($X_L$) without considering interfacial forces, and $\lambda_L$ scales the actual IGF thickness ($h_{EQ}$). [13,14]

To seek the nanoscale IGFs predicted in Fig. 5.3 in the single-phase region, Mo + 1 at. % Ni specimens were annealed at 1495 °C ($X_S$ = 1.89 %) and quickly quenched. SEM examination confirmed no observable secondary phase. These well-quenched specimens were characterized by HRTEM. Nanoscale IGFs were observed at six GBs

(among seven edge-on GBs that could be clearly imaged); the average measured thickness is 0.80 nm and the standard deviation is 0.12 nm. A representative HRTEM image is shown in Fig 5.4a, and this relatively thick IGF is presented so that the disordered structure can be more clearly evident. Furthermore, an FFT filtering method developed by MacLaren [16] was adopted to remove the lattice fringes, and the filtered image shown in Fig. 5.4b clearly shows a discrete IGF that exhibits high degree of structural disorder. Fig. 5.5 show a few images of different disordered IGF.

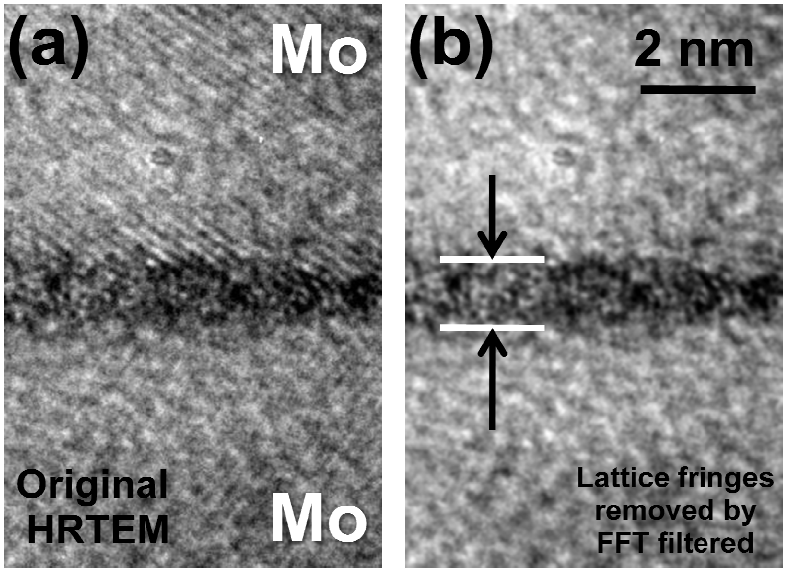


Figure 5.4 (a) An original (unprocessed) HRTEM image of an IGF in a Mo + 1 at. % Ni specimen quenched from 1495 °C. (b) After removing lattice fringes using a FFT filtering method that was developed for enhancing the images of thin IGFs in Ref. 18, a discrete film that exhibit high degree of structural disorder is more distinguishable.

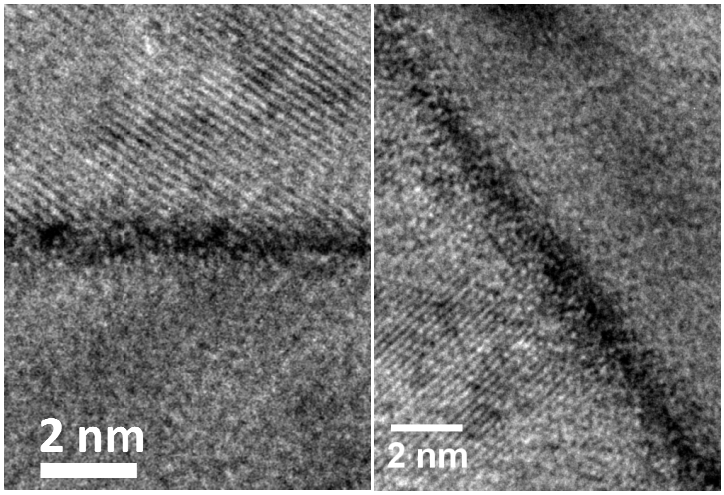


(a) (b)

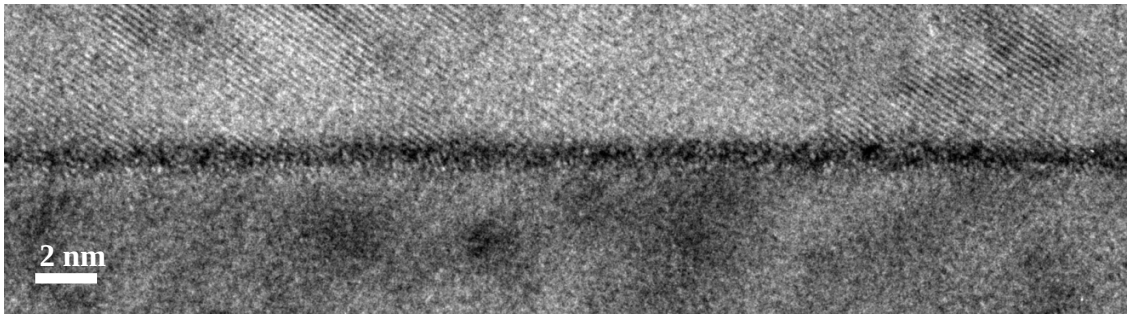


(c)

Figure 5.5 HRTEM images of the IGFs at different grain boundaries with similar disordered structures.

Additionally, Auger Electron Spectroscopy (AES) examination was conducted on specimens that were fractured in UHV in-situ. Ion sputtering was conducted in conjunction with AES to obtain the depth profiles. Fig. 5.6 shows a SEM image of in-situ fractured surface. Different numbers labeled the points whereby Auger spectra were collected. The final depth profile was obtained by selecting the average of the depth profiles of those different points in Fig. 5.5.

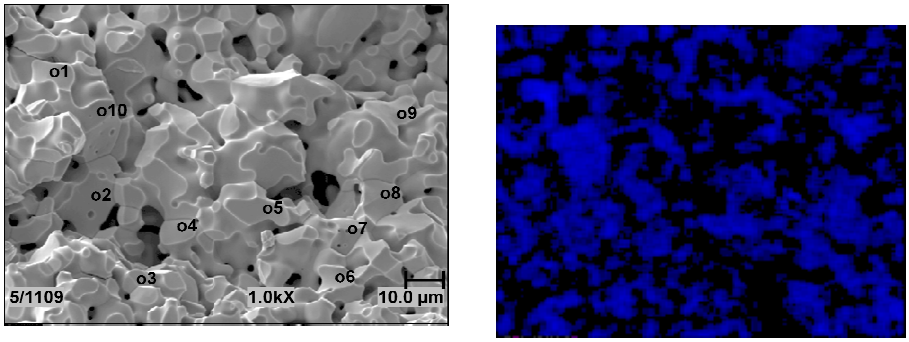


(a) (b)

Figure 5.6 (a) SEM image of in-situ fractured surface of Auger specimen, numbers labeled the points where Auger spectra were collected; (b) the mapping of Ni element.

The results shown in Fig. 5.7 clearly demonstrate the segregation of Ni at GB. Since the sputtering rate was calibrated for 2 nm/min for a $SiO_2$ standard specimen, the thickness of Ni-enriched IGF should be on nanometer scale (noting that the sputtering rate for the heavier Mo and Ni atoms should be slower. This result is consistent with direct HRTEM imaging.

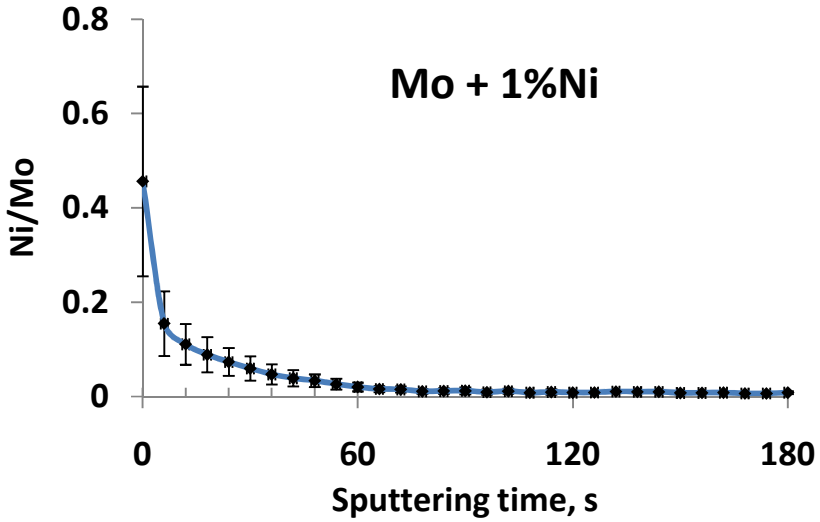


Figure 5.7 Depth profile of residue intergranular film on in-situ fracture surface of Mo + 1at. % Ni specimen quenched from 1495 °C. This depth profile was obtained by choosing an average of the depth profiles of six points on fractured surface specimen.

The above results suggested that activated sintering in Ni-doped Mo is likely due to enhanced mass transport in nanoscale quasi-liquid IGFs that form below the bulk peritectic temperature, similar to those reported for Ni-doped W [6,14,17] and $Bi_2O_3$-doped ZnO [18]. A further study of the sintering in this system is reported in Chapter Seven.

It is possible that the GB layers of δ-NiMo observed in prior studies [7,8] were disordered at firing temperatures but crystallized upon cooling. Alternatively, nanoscale layers of crystalline δ-NiMo could be stabilized at special GBs if there is a lattice match at one or two interface(s), where a strain effect might limit the film thickness.

## 5.3 Conclusions

Both experiments and thermodynamic models show that δ-NiMo does not wet Mo GBs in the solid state while the Ni-rich liquid does completely wet Mo GBs. HRTEM characterization of well-quenched specimens has directly revealed the stabilization of quasi-liquid IGFs in the single-phase region in Ni-doped Mo, which can critically impact materials fabrication processing and high-temperature properties. Further studies of thermodynamic modeling and sintering of the Mo-Ni system are reported and discussed in Chapter Six and Chapter Seven, respectively.

References

[1] J Luo. Stabilization of Nanoscale Quasi-Liquid Interfacial Films in Inorganic Materials: A Review and Critical Assessment Critical Reviews in Solid State and Material Sciences 32 (2007) 67.

[2] M Tang, WC Carter, RM Cannon. Grain Boundary Transitions in Binary Alloys Physical Review Letters 97 (2006) 075502.

[3] CM Bishop, M Tang, RM Cannon, WC Carter. Continuum Modelling and Representations of Interfaces and Their Transitions in Materials Materials Science and Engineering A 422 (2006) 102.

[4] BB Straumal, B Baretzky. Grain Boundary Phase Transitions and their Influence on Properties of Ploycrystals Interface Science 12 (2004) 147.

[5] VK Gupta, DH Yoon, HM Meyer III, J Luo. Thin Intergranular Films and Solid-State Activated Sintering in Nickel-Doped Tungsten Acta Materialia 55 (2007) 3131.

[6] J Luo, VK Gupta, DH Yoon, HM Meyer. Segregation-Induced Grain Boundary Premelting in Nickel-doped Tungsten Applied Physics Letters 87 (2005) 231902.

[7] KS Hwang, HS Huang. Identification of the Segregation Layer and Its Effects on the Activated Sintering and Ductility of Ni-doped Molybdenum Acta Materialia 51 (2003) 3915.

[8] JM Penisson, T Vystavel. Wetting of molybdenum grain boundaries by nickel: effect of the boundary structure and energy Acta Materialia 48 (2000) 3303.

[9] CM Bishop, M Tang, RM Cannon, WC Carter. Continuum Modelling and Representations of Interfaces and Their Transitions in Materials Materials Science and Engineering A 422 (2006) 102.

[10] R Benedictus, A Böttger, EJ Mittemijer. Thermodynamic Model for Solid-State Amorphization in Binary Systems at Interfaces and Grain Boundaries Physical Review B 54 (1996) 9109.

[11] RT DeHoff. Estimation of dihedral angles from stereological counting measurements Metallography 19 (1986) 209.

[12] D Bonn, D Ross. Wetting Transitions Reports on Progress in Physics 64 (2001) 1085.

[13] J Luo. Liquid-like interface complexion: from activated sintering to grain boundary diagrams Current Opinion in Solid State & Materials Science 12 (2008) 81.

[14] J Luo, X Shi. Grain boundary disordering in binary alloys Appl.Phys.Lett. 92 (2008) 101901.

[15] SJ Dillon, M Tang, WC Carter, MP Harmer. Complexion: a new concept for kinetic engineering in materials science Acta Materialia 55 (2007) 6208.

[16] I MacLaren. Imaging and thickness measurement of amorphous intergranular films using TEM Ultramicroscopy 99 (2004) 103.

[17] VK Gupta, DH Yoon, HM Meyer III, J Luo. Thin Intergranular Films and Solid-State Activated Sintering in Nickel-Doped Tungsten Acta Materialia 55 (2007) 3131.

[18] J Luo, H Wang, Y- Chiang. Origin of Solid State Activated Sintering in Bi2O3-Doped ZnO Journal of the American Ceramic Society 82 (1999) 916.

# CHAPTER SIX

# THERMODYNAMIC MODELS OF QUASI-LIQUID INTERGRANULAR FILMS IN NI-DODED MO

The basic concepts regarding the thermodynamic stability of subsolidus quasi-liquid intergranular films have been discussed in Chapter 4 using W-based binary alloys as examples. In this chapter, refined thermodynamic models are described more rigorously and discussed in great detail. Calculations are performed for the Ni-doped Mo system. The computed results are compared with the HRTEM and Auger results presented in Chapter 5, and correlated with the grain boundary diffusivity measurements from the controlled sintering experiments presented in Chapter 7.

## 6.1 A Phenomenological Thermodynamic Model

A phenomenological thermodynamic model can be proposed as an extension to a premelting model for unary systems [1,2,3]. In this model for binary alloys, the excess GB energy (referring to a mixture of equilibrium bulk phases) of a subsolidus liquid-like IGF in a binary A-B alloy is expressed as:

$$\sigma^x(h) \equiv G^S - (\mu_A\Gamma_A + \mu_B\Gamma_B) = 2\gamma_{cl} + \Delta G_{amorph}h + \sigma_{\text{interfacial}}(h), \qquad (6.1)$$

where $G^S$ is excess free energy according to the Gibbs definition, $\mu$ is the bulk potential, $\Gamma$ is the adsorption (GB excess), $h$ is the film thickness, $\gamma_{cl}$ is the interfacial energy of the crystal-liquid interface (which is well defined when the two interfaces are well separated

or $h \rightarrow +\infty$), $\Delta G_{\text{amorph}} \equiv G_{\text{liquid}} - G_{\text{crystal}}$ is the volumetric free energy for forming an undercooled liquid (assuming a uniform film), and $\sigma_{\text{interfacial}}$ is the *interfacial potential* (where $d\sigma_{\text{interfacial}}/dh$ is the well-known Derjaguin disjoining pressure). The interfacial potential ($\sigma_{\text{interfacial}}(h)$) represents the interactions of two interfaces when the film is thin, and it is the sum of all short- and long-range interfacial interactions using $h = +\infty$ as the reference point. By definition,

$$\begin{cases} \sigma_{\text{interfacial}}(0) = (\gamma_{gb}^{(0)} - 2\gamma_{cl}) \equiv -\Delta\gamma \\ \sigma_{\text{interfacial}}(+\infty) = 0 \end{cases}, \tag{6.2}$$

where we define $\gamma_{gb}^{(0)} \equiv \sigma^{x}(0)$ as the excess free energy of a "dry" GB, which is in general different from the equilibrium $\gamma_{gb}$. The equilibrium GB energy ($\gamma_{gb}$) corresponds to the global minimum in $\sigma^{x}(h)$, which specifies an "equilibrium" thickness:

$$\begin{cases} \left.\dfrac{d\sigma^{x}(h)}{dh}\right|_{h=h_{eq.}} = 0 \\ \gamma_{gb} \equiv \sigma^{x}(h_{eq}) \end{cases}. \tag{6.3}$$

One may further define a dimensionless *interfacial coefficient* as

$$f(h) \equiv 1 + \frac{\sigma_{\text{interfacial}}(h)}{\Delta\gamma}, \tag{6.4}$$

which satisfies

$$\begin{cases} f(0) = 0 \\ f(+\infty) = 1 \end{cases}. \tag{6.5}$$

Then, Eq. (6.1) can be rewritten as:

$$\Delta\sigma(h) \equiv \sigma^{x}(h) - \gamma_{gb}^{(0)} = \Delta\gamma \cdot f(h) + \Delta G_{amorph} h. \tag{6.6}$$

A liquid-like IGF of thickness $h$ can be thermodynamically more stable than a dry GB if $\Delta\sigma(h) < 0$. As such, an estimation of the IGF thickness can be given as:

$$h_{eq} = \frac{\Delta\gamma}{\Delta G_{amorph}} \cdot f(h_{eq}) < \frac{\Delta\gamma}{\Delta G_{amorph}} \equiv \lambda_L^* \tag{6.7}$$

Here the subscript "L" is used to denote that $\Delta G_{\text{amorph}}$ is calculated using a reference composition on the stable or metastable liquidus line. (Possible strategies for selecting this hypothetic reference film composition are discussed in §6.2, among which this assumption leads to a theoretically elegant treatment of the phenomenological model.) If the interfacial coefficient takes a simple exponentially decaying form with a characteristic coherent length of $\xi$ (as what is commonly assumed for the premelting theories for one-component metals):

$$f(h) \approx 1 - e^{-h/\xi}\ , \tag{6.8}$$

minimizing $\Delta\sigma(h)$ leads to:

$$h_{EQ} \approx \xi \cdot \ln(\lambda_L^* / \xi)\,, \tag{6.9}$$

## 6.2 Through-Thickness Gradients, Film Composition and Simplifications

Through-thickness compositional and structural gradients generally exist in an IGF. Correspondingly, $\Delta G_{\text{amorph}}$ is calculated after a (somewhat subjective) selection of a reference film composition (for a hypothesized uniform film of undercooled liquid as a reference state); the remaining volumetric free energies, along with the excess free energies associated with the compositional and structural gradients, are then to be

considered in the interfacial potential so that the thermodynamic treatment remains rigorous. Prior studies have assumed this reference composition to be the average film composition [4,5] or the composition that maximizes a particular figure of merit (such as $\lambda$ in Chapter 4 [6]; see elaboration below). In either of the above conventions, this reference composition becomes a function of film thickness, approaching the (stable or metastable) liquidus composition ($X_L$) as $h \rightarrow +\infty$. An alternative, and perhaps theoretically more elegant, strategy is to select a constant reference film composition (independent of $h$). In this case, this reference composition must be $X_L$ to ensure that $\sigma_{\text{interfacial}}(+\infty) = 0$, even if the average film composition can be significantly different from $X_L$ when the film is thin.

Furthermore, the equilibrium $\gamma_{cl}$ should consider the effects of the near-interface gradients in composition (absorption) and structure (partial ordering), which are generally difficult to quantify. A useful strategy is to define a new "un-relaxed" $\gamma_{cl}^{(0)}$ ($> \gamma_{cl}$) for a hypothesized "step" interface between a crystal and a perfect liquid (without any adsorption and near-interface ordering), which can be easier to quantify (as discussed in the following section). Then, we can define a new thermodynamic variable, with respect to a hypothesized uniform film of a perfect liquid, as:

$$\lambda_X(X_{film}) \equiv \frac{\gamma_{gb}^{(0)} - 2\gamma_{cl}^{(0)}(X_{film})}{\Delta G_{amorph}(X_{film})} . \tag{6.10}$$

Two particular $\lambda$'s that can be quantified are:

$$\begin{cases} \lambda \equiv \underset{(0<X_{film}<1)}{\text{Max}} \{\lambda_X(X_{film})\} \\ \lambda_L \equiv \lambda_X(X_L) \end{cases} \tag{6.11}$$

It is easy to demonstrate that:

$$\lambda_L < \lambda; \quad \lambda_L < \lambda_L^*, \tag{6.12}$$

and

$$\begin{cases} \lim\limits_{\lambda \to +\infty} \dfrac{\lambda_L}{\lambda} \to 1 \\ \dfrac{\lambda_L^*}{\lambda_L} = \dfrac{\gamma_{gb}^{(0)} - 2\gamma_{cl}}{\gamma_{gb}^{(0)} - 2\gamma_{cl}^{(0)}} \end{cases}. \tag{6.13}$$

All three λ's represent the thermodynamic tendency for stabilizing subsolidus liquid-like IGFs, and they scale the actual film thickness. Since the exact form of the interfacial potential is generally unknown, none of them can guarantee more predictive power than others. While $\lambda_L^*$ appears to be conceptually more rigorous, λ and $\lambda_L$ are generally easier to quantify. In Chapter 4 and an earlier publication [6], we quantified λ via a numerical method. More recently, we derived an analytical solution for $\lambda_L$ for regular solutions [7] (and in this chapter we further generalize it to subregular solutions), which is practically useful.

In summary, $\lambda_L$, which is the maximum thickness of a stable IGF assuming an uniform film composition of $X_L$ and no interfacial interactions, appears to be the most convenient thermodynamic variable to be used practically. Thus, it will be used here. To compute $\lambda_L$ as a function of temperature and bulk composition, interfacial energies ($\gamma$'s) and bulk free energies (to compute $\Delta G_{amorph}$) need to be quantified via statistical models or computational thermodynamic methods, which are discussed in the following sections.

## 6.3 Estimation of Interfacial Energies via Statistical Models

The interfacial energies ($\gamma$'s) can be estimated by either lattice-gas models or Miedema-type "macroscopic atom" models.

### 6.3.1 Lattice-Gas Model

In the lattice-gas model, the crystal-liquid interfacial energy can be expressed as [8]:

$$\gamma_{cl}^{(0)} = \gamma_{<A>-\{A\}} X_A^S + \gamma_{<B>-\{B\}} X_B^S + \frac{m_1\omega_L(X_A^L X_B^S + X_A^S X_B^L)}{V^{2/3}} - \frac{m_1\omega_L X_A^L X_B^L}{V^{2/3}} - \frac{m_1\omega_S X_A^S X_B^S}{V^{2/3}} \quad (6.14)$$

where $\gamma_{<A>-\{A\}}$ and $\gamma_{<B>-\{B\}}$ represent the solid-liquid interfacial energies of pure A or B respectively; $X_A^S$ and $X_A^L$ are atomic fractions of A in solid and liquid, respectively; similarly, $X_B^S$ and $X_B^L$ are atomic fractions of B in solid and liquid, respectively ($X_A^S + X_B^S = 1$; $X_A^L + X_B^L = 1$); $\omega_L$ and $\omega_S$ are the regular solution parameters for solid and liquid, respectively; $m_1$ is the fraction of the (liquid type) bonds that are "cross" the interface; $V$ is molar volume; $V^{2/3}$ is molar area; $R$ is gas constant; and $T$ is temperature. Essentially, the estimation of solid-liquid interfacial energy by Eq. (6.14) is determined through calculating the bond energies. Here the key assumptions (simplifications) are:

- The solid-liquid interface can be represented by a step function (i.e., adsorption at the interface and near-interface ordering are not considered); thus only the bonds

between the first layer of the liquid and first layer of the solid contribute to the interfacial energy;

- These bonds at the interface are liquid-type; and
- The reference state is bulk binary solutions (assuming that the bulk solid is in a thermodynamic equilibrium with the bulk liquid phase).

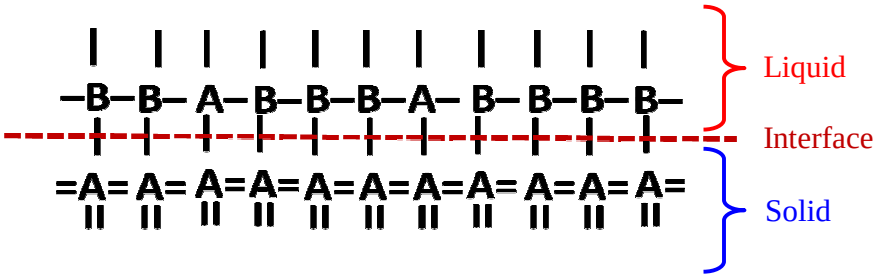


Figure 6.1 Schematic illustration of the lattice-gas model for a liquid-solid interface of an A-B binary system. Assuming that the solubility of B in solid is negligible ( $X_B^S = 0$).

If the solubility of B in A crystal is negligible ( $X_B^S = 0$; $X_A^S = 1$), Eq. (6.14) can be simplified to:

$$\gamma_{cl}^{(0)} = \gamma_{<A>-\{A\}} + \frac{m_1 \omega_L}{V^{2/3}} (1 - X_A^L)^2 \qquad (6.15)$$

where the first term is due to the enthalpic contribution; the second term is the interaction contribution (a "chemistry" term resulted from the formation of a different number of A-B bonds at the interfaces as compared to those in the bulk liquid). The above lattice-gas model is schematically illustrated in Fig. 6.1.

The above model can be further modified by considering the adsorption and compositional gradients at the solid-liquid interfaces, which are discussed by Shimizu

and Takei [9,10]. An entropic term associated with ordering at the interfaces (discussed below in the Benedictus model) can also be added.

### 6.3.2 "Macroscopic Atom" Model

Instead of using the lattice-gas type models described above, we adopt and modify a Miedema-type "macroscopic atom" model to estimate interfacial energies. The "macroscopic atom" model is developed on a similar base as lattice-gas models, and it is more realistic to represent actual transition metal alloys. This "macroscopic atom" model has the following features (that are useful for achieving our objectives):

- It considers the different molar volumes for A and B;
- It represents average interfaces without anisotropic effects (while the lattice-gas model considers the anisotropic effects via the coordination numbers); and
- It provides a systematical method to evaluate all required thermodynamic parameters (for all binary transition metal alloys as well as some other alloys).

Benedictus *at al.* reported a systematic approach to evaluating interfacial energies based on the Miedema type "macroscopic atom" model, and the entropic contribution is added into the model [11]. In this model, the interfacial energy for an A crystal (assuming that the solubility of B in A crystal is negligible) and a binary A-B liquid is expressed as:

$$\gamma_{cl}^{(0)} = \underbrace{\frac{H_{\mathrm{A}}^{\mathrm{fuse}}}{C_0 V_A^{2/3}}}_{Enthalpic} + \underbrace{\frac{\Delta H_{A\,in\,B}^{\mathrm{interface}} F_B^A}{C_0 V_A^{2/3}}}_{Interaction} + \underbrace{\frac{1.9RT}{C_0 V_{A/B}^{2/3}}}_{Entropic} \tag{6.16}$$

where $H_A^{fuse}$ is the fusion enthalpy of A; $\Delta H_{A\,in\,B}^{\mathrm{interface}}$ is the enthalpy of solution (similar as shown in the Miedema model); $C_0 \approx 4.5 \times 10^8$; $V$ is the molar volume (neglecting thermal

expansion); $R$ is the gas constant; and $F_B^A$ represents the "area" fraction A-B bonds at the interface, which is expressed as:

$$F_B^A = \frac{X_B V_B^{2/3}}{(1-X_B)V_A^{2/3} + X_B V_B^{2/3}}, \tag{6.17}$$

where $X_B$ is the atomic fraction of B in the liquid phase.

In Eq. (6.16), liquid-crystal interfacial energy is comprised of enthalpic, interaction, and entropic contributions, which are articulated in Ref. [11].

It is important to note that the interaction term in Eq. (6.16) is derived assuming that the reference states are solid pure A and pure B (which is valid for the discussion of solid-state amorphization - the initial objective for Benedictus *et al.*'s work). In our case, however, we wish to use the thermodynamic equilibrium state as the reference state. To achieve this, we may assume that the reference state is set by the bulk liquid (by assuming the bulk solid A, with negligible solutes of B, is in a thermodynamic equilibrium with the bulk liquid). In other words, the reference state for the interaction term is set by a hypothetical liquid-liquid interface, which should have zero excess interfacial energy. In terms of the "macroscopic atom" model, the reference state would produce the following interfacial energy:

$$\gamma_{liq-liq.}^{(\text{Inter. Ref.})} = \frac{\Delta H_{A\,in\,B}^{\text{interface}}}{C_0 V_A^{2/3}}[2F_B^A \cdot (1-F_B^A)], \tag{6.16b}$$

where $[2F_B^A \cdot (1-F_B^A)]$ represents the "area" fraction of A-B bonds for this hypothetical liquid-liquid interface (which should produce zero excess interaction energy by definition). Thus, Eq. (6.16) should be revised to

$$\gamma_{cl}^{(0)} = \underbrace{\frac{H_{\mathrm{A}}^{\mathrm{fuse}}}{C_0 V_A^{2/3}}}_{Enthalpic} + \underbrace{\left[\frac{\Delta H_{A\,in\,B}^{\mathrm{interface}} F_B^A}{C_0 V_A^{2/3}} - \frac{1}{2}\gamma_{liq-liq.}^{(\mathrm{Inter.\,Ref.})}\right]}_{Interaction} + \underbrace{\frac{1.9RT}{C_0 V_{A/B}^{2/3}}}_{Entropic} \tag{6.16c}$$

Or:

$$\gamma_{cl}^{(0)} = \underbrace{\frac{H_{\mathrm{A}}^{\mathrm{fuse}}}{C_0 V_A^{2/3}}}_{Enthalpic} + \underbrace{\frac{\Delta H_{AinB}^{\mathrm{interface}} (F_B^A)^2}{C_0 V_A^{2/3}}}_{Interaction} + \underbrace{\frac{1.9RT}{C_0 V_{A/B}^{2/3}}}_{Entropic} \tag{6.16d}$$

Specific to the Ni-Mo binary system of our interest, the liquid-crystal interfacial energy was derived from Eq. (6.16d) and determined as

$$\gamma_{cl}^{Ni-Mo} = [0.138 - 0.160(F_{Ni}^{Mo})^2 + 8.92\times10^{-5}T]\ \mathrm{J/m^2} \tag{6.18}$$

where

$$F_{Ni}^{Mo} = \frac{X_{Ni}V_{Ni}}{X_{Ni}V_{Ni} + X_{Mo}V_{Mo}} = \frac{X_{Ni}}{1.253 - 0.253X_{Ni}} \tag{6.19}$$

The average GB energy of Mo, $\gamma_{gb}^{(0)}$, in polycrystalline materials was determined by using the Turnbull's estimation [12,13,14,15]:

$$\gamma_{gb}^{(0)} \approx 1/3 \cdot \gamma_{Mo}^{s} \tag{6.20}$$

The surface energy of Mo at $T$ = 0K was estimated by enthalpy of evaporation:

$$\gamma_{Mo}^{s} = \frac{H_{Mo}^{vap}}{C_0 V_{Mo}^{2/3}} \tag{6.21}$$

In reality, surface energy is temperature-dependent, where both the thermal expansion effect and entropy effect need to be considered.

$$\gamma_{Mo}^{s}(T_1) = \frac{(\gamma_{Mo}^{s} V_{Mo}^{2/3})^{T=0K} + b_{Mo}T_1}{(V_{Mo}^{2/3})^{T=T_1}} \tag{6.22}$$

$b_{\mathrm{Mo}}$ is a materials-dependent constant. Furthermore, structure relaxation at the free surface will also reduce its excess energy. Nevertheless, these effects are relatively small (as compared with the approximations associated with Eq. (6.20)), and they are generally more difficult to quantify. Thus, they were neglected in our calculation for simplicity. Combining Eq. (6.20) and (6.21) gives an estimation of $\gamma_{gb}^{(0)} \approx 1.0$ J/m$^2$.

The limitations of this model include:

- Adsorption at liquid-crystal interfaces is not considered. This is addressed, in part, in a lattice-gas model by Shimizu & Takei.[9,10]
- Anisotropic effects are not considered. This is considered in a sophisticated lattice-gas model by Wynblatt *et al.*[16].
- Segregation within the lattice at GBs is not considered. This can be considered by Wynblatt *et al.*'s model [16].
- The "asymmetric effects," which are not addressed here in regular solution type models, are discussed in sub-regular solution models by Antion and Chatain [17].

## 6.4 Estimation of the Free Energy Penalty for Forming An Undercooled Liquid

### 6.4.1 The CalPhaD Method

The Calculation of Phase Diagram (CalPhaD) method was adopted to determine the free energy penalty to form an undercooled liquid ($\Delta G_{\mathrm{amorph}}$). CalPhaD is a well-

established method to compute bulk phase diagrams from (usually empirically-fitted) thermodynamic functions of free energies. The Gibbs free energy of a phase $\Phi$ in a binary A-B system can be expressed as:

$$G^{\Phi} = \sum_{i=A,B} X_i \cdot {}^{0}G_i^{\Phi} + RT \sum_{i=A,B} X_i \ln X_i + {}^{XS}G^{\Phi} \tag{6.23}$$

where ${}^{0}G_i^{\Phi}$ is the Gibbs free energy of the pure element $i$ (= $A$ or $B$) that is present in $\Phi$ phase; $X_i$ is the atomic fraction of element $i$; ${}^{XS}G^{\Phi}$ is the excess Gibbs free energy, which can be empirically expressed in a Redlich-Kister polynomial:

$${}^{XS}G^{\Phi} = X_A X_B \sum_{j=0}^{n} L_j^{\Phi} (X_A - X_B)^j \,. \tag{6.24}$$

Here, $L_j^{\Phi}$'s are empirically-fitted parameters for the phase $\Phi$. If $n$ = 0, the phase $\Phi$ is a regular solution, and Eq. (6.24) is reduced to

$${}^{XS}G^{\Phi} = L_0^{\Phi} X_A X_B \equiv \omega X_A X_B \,. \tag{6.25}$$

where $\omega$ (= $L_0^{\Phi}$) is the regular solution parameter. If $\omega$ = 0, the phase $\Phi$ is an ideal solution ( ${}^{XS}G^{\Phi}$ = 0).

If $n$ = 1, the phase $\Phi$ is a sub-regular solution. Eq. (6.24) can be rewritten as

$${}^{XS}G^{\Phi} = L_0^{\Phi} X_A X_B + L_1^{\Phi} X_A X_B (X_A - X_B) \,. \tag{6.26}$$

Gibbs free energy functions for compounds and ordered solutions can be constructed using different models, which are discussed in Ref. [18]. For a given binary A-B system, the Gibbs free energy functions can be developed for all possible phases. Then a bulk phase diagram can be constructed by minimizing the total free energy of the system. In

two-phase regions, the equilibrium states can be found graphically via a well-established "common tangent construction" method.

For the Ni-Mo binary system, four phases (BCC, FCC, δ-NiMo, and liquid phases) are considered. The excess Gibbs energies of each were determined and the Gibbs free energies of different phases are listed in Table 6.1a [19] and Table 6.1b [20].

Table 6.1a Gibbs free energies of the different phases in the Ni-Mo system [19].

| Phase | Gibbs free energy, J/mol |
|---|---|
| Liquid phase | $X_{Ni}{}^{o}G_{Ni}^{liq} + X_{Mo}{}^{o}G_{Mo}^{liq} - T\Delta S_{conf.} + X_{Ni}X_{Mo}[-46540 - 19.53T - 2915(X_{Mo} - X_{Ni})]$ |
| Mo-rich BCC | $X_{Ni}{}^{o}G_{Ni}^{BCC} + X_{Mo}{}^{o}G_{Mo}^{BCC} - T\Delta S_{conf.} + 46422X_{Ni}X_{Mo}$ |
| Ni-rich FCC | $X_{Ni}{}^{o}G_{Ni}^{FCC} + X_{Mo}{}^{o}G_{Mo}^{FCC} - T\Delta S_{conf.} + X_{Ni}X_{Mo}[-4803.7 - 5.96T - 10880(X_{Mo} - X_{Ni})]$ |
| δ-NiMo | $24{}^{o}G_{Ni}^{FCC} + 32{}^{o}G_{Mo}^{BCC} - 212100 + 1089T - 142T\ln(T)$ |

Note: $\Delta S_{\text{conf}} = X_{\text{Ni}} ln X_{\text{Ni}} + X_{\text{Mo}} ln X_{\text{Mo}}$.

Table 6.1b Gibbs free energies of the different phases in the Ni-Mo system [20].

| Phase | Gibbs free energy, J/mol |
|---|---|
| Liquid phase | $X_{Ni}{}^{o}G_{Ni}^{liq} + X_{Mo}{}^{o}G_{Mo}^{liq} - T\Delta S_{conf.} +$ $X_{Ni}X_{Mo}[-39597 + 15.935T - 7373(X_{Mo} - X_{Ni}) + (-12123 + 5.551T)(X_{Mo} - X_{Ni})^2]$ |
| Mo-rich BCC | $X_{Ni}{}^{o}G_{Ni}^{BCC} + X_{Mo}{}^{o}G_{Mo}^{BCC} - T\Delta S_{conf.} + X_{Ni}X_{Mo}[27691 + 18792(X_{Mo} - X_{Ni})]$ |
| Ni-rich FCC | $X_{Ni}{}^{o}G_{Ni}^{FCC} + X_{Mo}{}^{o}G_{Mo}^{FCC} - T\Delta S_{conf.} + X_{Ni}X_{Mo} \cdot$ $[-8916 + 3.591T + (5469 - 0.249T)(X_{Mo} - X_{Ni}) + (-1549 - 2.741T)(X_{Mo} - X_{Ni})^2]$ |
| δ-NiMo | $24{}^{o}G_{Ni}^{FCC} + 20{}^{o}G_{Mo}^{BCC} + 12{}^{o}G_{Mo}^{BCC} - 169981 + 1154.981T - 155.484T\ln(T)$ $+ 24{}^{o}G_{Ni}^{FCC} + 20{}^{o}G_{Ni}^{FCC} + 12{}^{o}G_{Mo}^{BCC} - 154106 + 2855.001T - 394.923T\ln(T)$ $-199.856T + 0.3367 \cdot [(-829211 + 825.923T) + 0.3571 \cdot (-417368 + 326.504T)]$ |

Note: $\Delta S_{\text{conf}} = X_{\text{Ni}} ln X_{\text{Ni}} + X_{\text{Mo}} ln X_{\text{Mo}}$.

Table 6.1c Comparison of phase diagram data by the two groups of thermodynamic functions listed in Table 6.1a and Table 6.1b, respectively.

| Key markers | Experimental value | Krisk's [19] | Zhou *et al.*'s [20] |
|---|---|---|---|
| $T_{\text{peritectic}}$, ºC | 1362 [21,22] | 1364 | 1345 |
| Solidus line and solvus line of BCC | From ref. [23,24] | Good fit | No validation |

The thermodynamic functions in Table 6.1b are more sophisticated than those in Table 6.1a, as they consider entropic contribution to the Gibbs free energy of δ–NiMo compound. Consequently, the thermodynamic functions listed in Table 6.1b achieved better accuracy for predicting FCC phase and intermetallic compounds. However, the thermodynamic functions in Table 6.1a lead to better predictions for the solidus and solvus lines of the Mo-rich BCC and the peritectic temperature, which are our primary concerns. Therefore, we used Table 6.1 for our calculations.

When the thermodynamic functions of all phases are known, we can construct a binary phase diagram by drawing a common tangent line and finding equilibrium phases. Constructions for two representative temperatures of the Mo-Ni binary system are shown in Fig. 6.2.

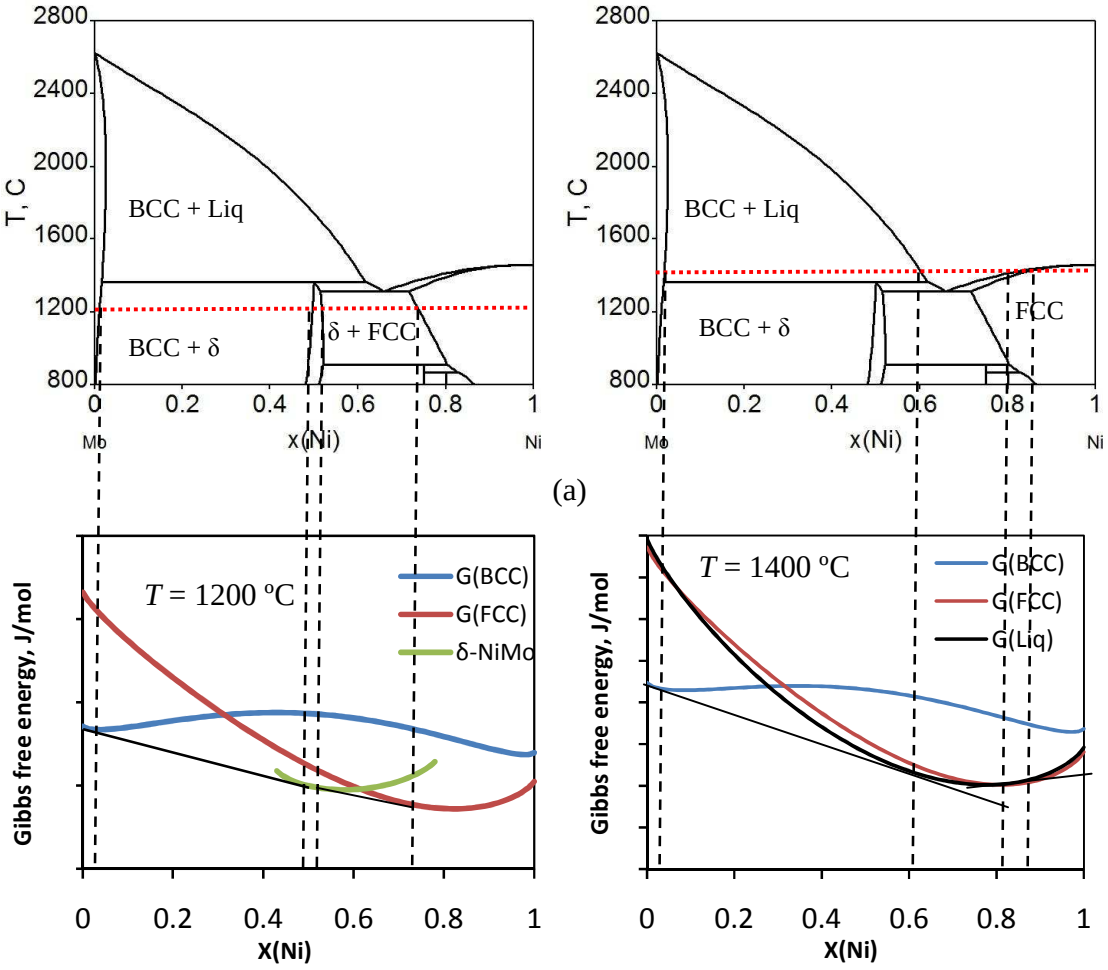


Figure 6.2 Schematic illustration of phase diagram constructions: (a) The Mo-Ni binary phase diagram. (b) Plots of Gibbs free energies of different phases vs. Ni atomic fraction for 1200 ºC (< $T_{peritectic}$) and 1400 ºC ( > $T_{peritectic}$), in which common tangent lines were drawn to find the phase boundaries.

### 6.4.2 Determination of $\Delta G_{amorph}$ and $\lambda_L$

The CalPhaD method was used to compute $\Delta G_{amorph}$ and then $\lambda$. From now on, the subscript "Ni" is dropped for briefly, all the $X$'s ($X$, $X_{film}$, $X_S$, $X_L$) in equations are referred to as atomic fraction of Ni in Ni-Mo binary system with the following definitions:

$X$: the Ni fraction (general)

$X_{film}$: the Ni fraction of IGF

$X_0$: the Ni fraction of the bulk (BCC) phase (which sets the bulk chemical potentials)

$X_S$: the Ni fraction on the solidus line or (if $T < T_{preitectic}$) its metastable extension

$X_L$: the Ni fraction on the solidus line or (if $T < T_{preitectic}$) its metastable extension

$X_{solvus}$: the Ni fraction on the solvus line (for $T < T_{preitectic}$)

Note : if you used X0 as bulk composition, you need to change all equations accordingly

In particular, analytical expressions for $\lambda_L$ can be obtained with two assumptions:

- The IGF has a uniform composition that is equal to the composition on the liquidus line or its metastable extension; and
- The solid (BCC) phase is a regular or sub-regular solution, so its mixing Gibbs energy is given by

$$\Delta G_{Solid}^{MIX} = RT[X_0 \ln X_0 + (1-X_0)\ln(1-X_0)] + L_0^S X_0(1-X_0) + L_1^S X_0(1-X_0)(1-2X_0), \quad (6.27)$$

where $X_0$ is the Ni atomic fraction in the solid phase; $L_0^S$ (=ω) and $L_1^S$ are sub-regular (or regular) solution parameters. In our calculations, the solid phase is the BCC phase because the FCC phase is unstable in this composition region of interest.

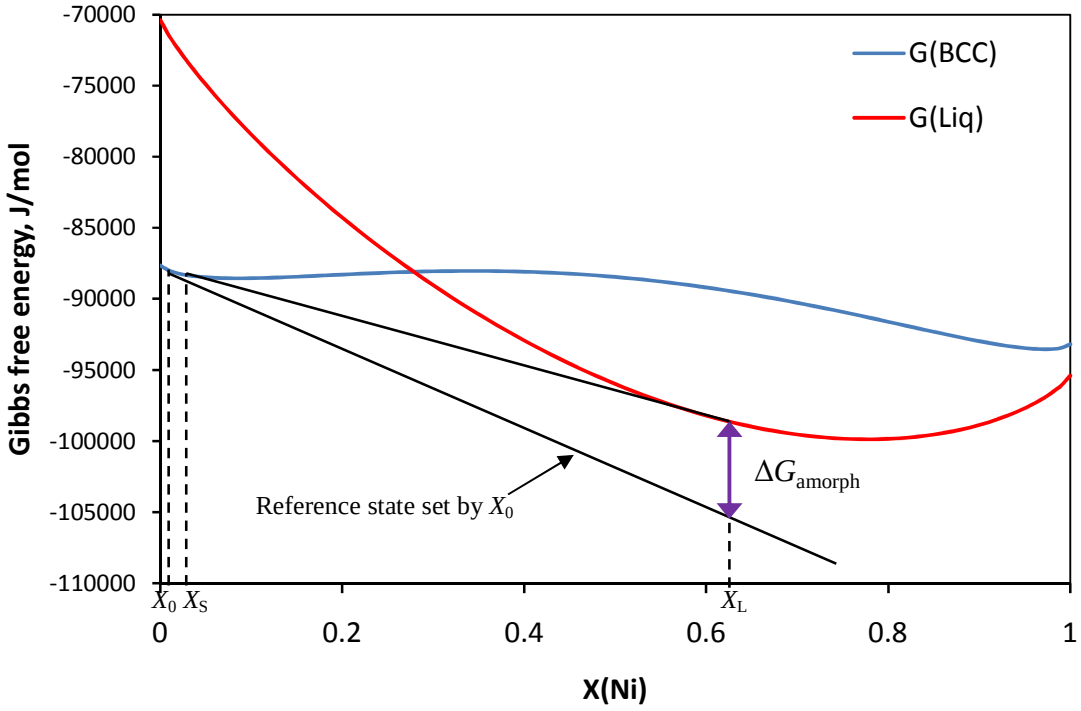


(a)

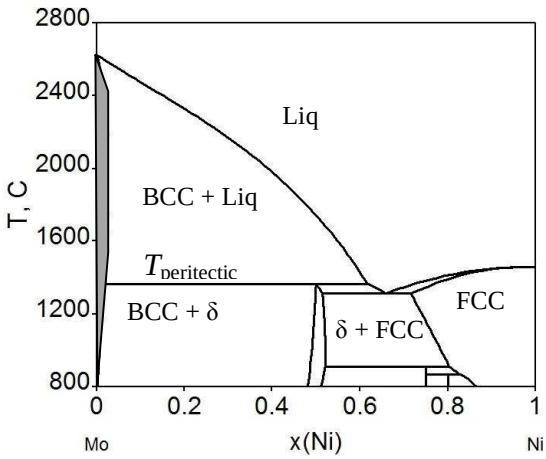


(b)

Figure 6.3 (a) The representation of $\Delta G_{amorph}$ ($X_L$) in the plots of Gibbs free energies vs. Ni fraction for a case of $X_0 < X_S$ and $T$ =1400 ºC ( > $T_{peritectic}$ ), where $X_0$ is the bulk composition. $X_S$ and $X_L$ are equilibrium solidus and liquidus compositions, respectively; (b) The single-phase regime is shaded.

First, we will determine the $\Delta G_{\text{amorph}}$ in the single-phase (BCC) regime. Fig. 6.3 shows an example at $T$ = 1400 ºC ($T > T_{\text{peritectic}}$), in which we assume that the composition of the bulk BCC phase ($X_0$) is lower than the bulk solidus composition ($X_S$). The $\Delta G_{\text{amorph}}$ is defined as the difference between formation energy of the liquid phase (the red line in Fig. 6.3(a)) and the reference state set by the chemical potential of the bulk phase of a composition $X_0$ (the black straight line labeled in Fig. 6.3(a)). This reference state is given by:

$$G^{\text{Ref.}}(X) = X_{film} \cdot \mu_{Ni} + (1 - X_{film}) \cdot \mu_{Mo} = G^f_{bcc}(X_0) + (X_{film} - X_0) \left. \frac{dG^f_{bcc}}{dX} \right|_{X=X_0}, \tag{6.28}$$

which corresponds to the tangent line extended from $X_0$ in Fig. 6.3 (a). Thus, the free energy penalty to form a metastable liquid of composition $X_L$ (being labeled by a purple double arrow in Fig. 6.3(a)) is given by:

$$\Delta G_{\text{amorph}} \approx G^f_{\text{liq}}(X_L) - \left[ G^f_{bcc}(X_0) + (X_L - X_0) \left. \frac{dG^f_{bcc}}{dX} \right|_{X=X_0} \right], \tag{6.29}$$

where $G^f_{liq}$ and $G^f_{bcc}$ are the formation free energies of liquid and solid BCC phases, respectively.

By definition, $\Delta G_{\text{amorph}}$ vanishes if the composition of solid BCC phase is on the bulk solidus line ($X_0 = X_S$), which is the case represented by the common tangent line between $X_S$ and $X_L$ in Fig. 6.3 (a); thus

$$G^f_{liq}(X_L) = G^f_{bcc}(X_S) + (X_L - X_S) \left. \frac{dG^f_{bcc}}{dX} \right|_{X_S}. \tag{6.30}$$

Combining Eqs. (6.27-6.30), while assuming $X_{\text{film}} = X_{\text{L}}$ , gives:

$$\Delta G_{amorph} = RT\left[ X_L \ln\frac{X_s}{X_0} + (1-X_L)\ln\frac{1-X_s}{1-X_0}\right] -$$
$$(X_S - X_0)\left[2X_L(L_0^{BCC} + 3L_1^{BCC}) - (L_0^{BCC} + 3L_1^{BCC} + 6L_1^{BCC})(X_S + X_0) + 4L_1^{BCC}(X_S^2 + X_S X_0 + X_0^2)\right] \quad (6.31)$$

If the solid BCC phase is a regular solution ( $L_1^{BCC} = 0$; $L_0^{BCC} = \omega$), it can be reduced to

$$\Delta G_{amorph} = RT\left[ X_L \ln\frac{X_s}{X_0} + (1-X_L)\ln\frac{1-X_s}{1-X_0}\right] - \omega(X_S - X_0)(2X_L - X_S - X_0)\,. \quad (6.32)$$

Second, in the single BCC phase regime below $T_{\text{peritectic}}$, the calculation is almost the same as that described above for $T > T_{\text{peritectic}}$. The same equations are used, and the only difference is that $X_{\text{S}}$ and $X_{\text{L}}$ are now the Ni fractions on the metasatble extensions of the solidus and liquidus lines, as illustrated in Fig. 6.4 (for an example for $T$ = 1200 ºC). Note that now the solid solubility corresponds to the solvus line $X_{\text{solvus}}$ (instead of $X_{\text{S}}$, which is on the metastable extension of solidus line) for $T > T_{\text{peritectic}}$.

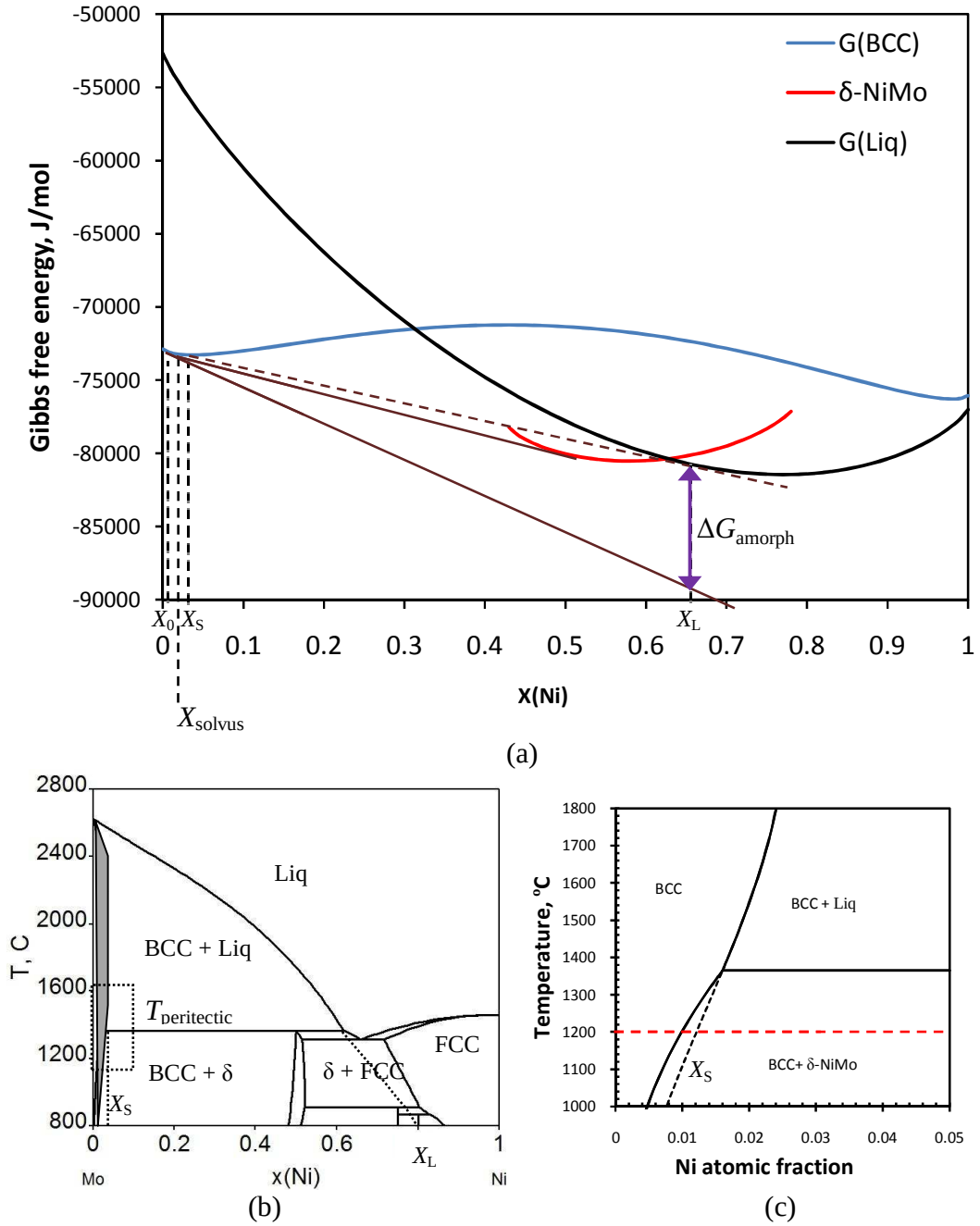


Figure 6.4 (a) The representation of $\Delta G_{amorph}$ ($X_L$) in the plots of Gibbs free energies vs. Ni atomic fraction for a case of $X_0 < X_{solvus}$ and $T$ = 1200 ºC ( < $T_{peritectic}$), where $X_S$ is the composition on the metastable extension of the solidus line; (b) and (c) are the corresponding bulk phase diagram and an expended view. Bulk solidus and liquidus

composition ($X_S$ and $X_L$ respectively) are extended into metastable region as a dashed line.

Finally, in the sub-peritectic two-phase regime, $\Delta G_{\text{amorph}}$ ($X_L$) is a constant at a specific temperature and it does not depend on the overall bulk composition because the bulk chemical potential is a constant. Therefore, $\Delta G_{\text{amorph}}$ ($X_L$) can be determined by using Eq. (6.32) or (6.31) and assuming $X_0 = X_{\text{solvus}}$:

$$\Delta G_{amorph} = RT\left[ X_L \ln\frac{X_s}{X_{slvus}} + (1-X_L)\ln\frac{1-X_s}{1-X_{solvus}}\right] - \omega(X_S - X_{solvus})(2X_L - X_S - X_{solvus})$$
. (6.33)

for a regular solution, or

$$\Delta G_{amorph} = RT\left[ X_L \ln\frac{X_s}{X_{solvus}} + (1-X_L)\ln\frac{1-X_s}{1-X_{solvus}}\right] -$$
$$(X_S - X_{solvus})\left[2X_L(L_0^{BCC} + 3L_1^{BCC}) - (L_0^{BCC} + 3L_1^{BCC} + 6L_1^{BCC})(X_S + X_{solvus}) + 4L_1^{BCC}(X_S^2 + X_S X + X_{solvus}^2)\right] \quad (6.34)$$

for a sub-regular solution.

Furthermore, in the sub-peritectic two-phase regime, $\lambda_L$'s are horizontal lines, and lines of constant $\lambda_L$ can be constructed graphically by finding the intersections of constant $\lambda_L$ lines and the solvus line, as illustrated in Fig. 6.5(c).

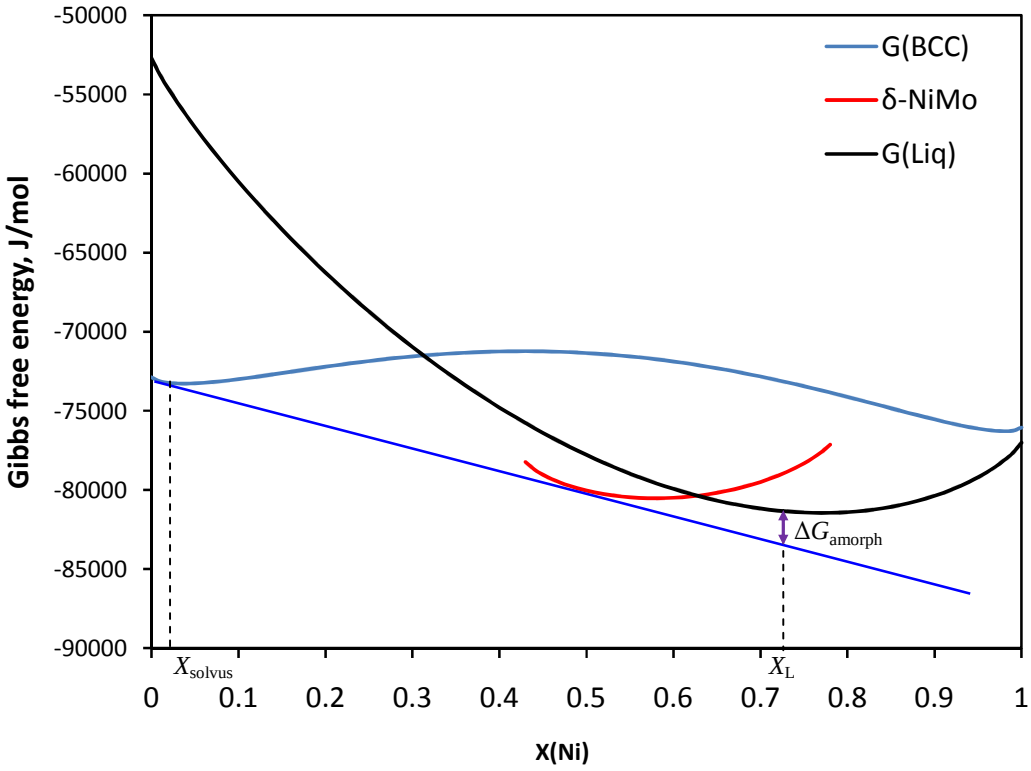


(a)

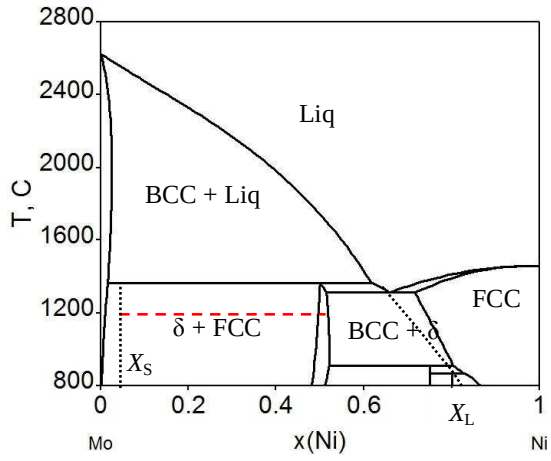


(b)

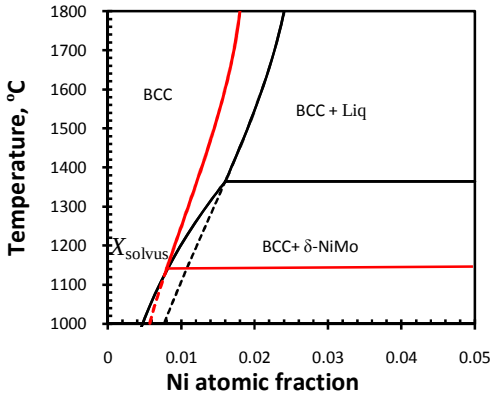


(c)

Figure 6.5 (a) Illustration of determining $\Delta G_{amorph}$ at $T$ = 1200 ºC in the sub-peritectic two-phase regime; (b) Ni-Mo binary phase diagram. The red dashed line represents regime of calculation. (c) Construction of lines of constant $\lambda_L$.

## 6.5 Computed Grain Boundary Diagram for the Mo-Ni System

### 6.5.1 Computed $\lambda_L$ and $\lambda$ vs. Ni Atomic Fraction

Fig. 6.6 shows computed of $\lambda_L$ and $\lambda$ vs. Ni atomic fraction at three representative temperatures. The same trends are found for $\lambda_L$ and $\lambda$ (although $\lambda_L < \lambda$), and both are divergent as bulk Ni composition approaches the solidus line (or its metastable extension). For $T < T_{peritectic}$, $\lambda_L$ and $\lambda$ level off at the bulk solvus line $X_0 = X_{solvus}$, above which the bulk chemical potential is a constant (despite any change in the overall bulk composition in the BCC-NiMo two phase region). As we have discussed above, we will focus on $\lambda_L$ because it is easier to compute.

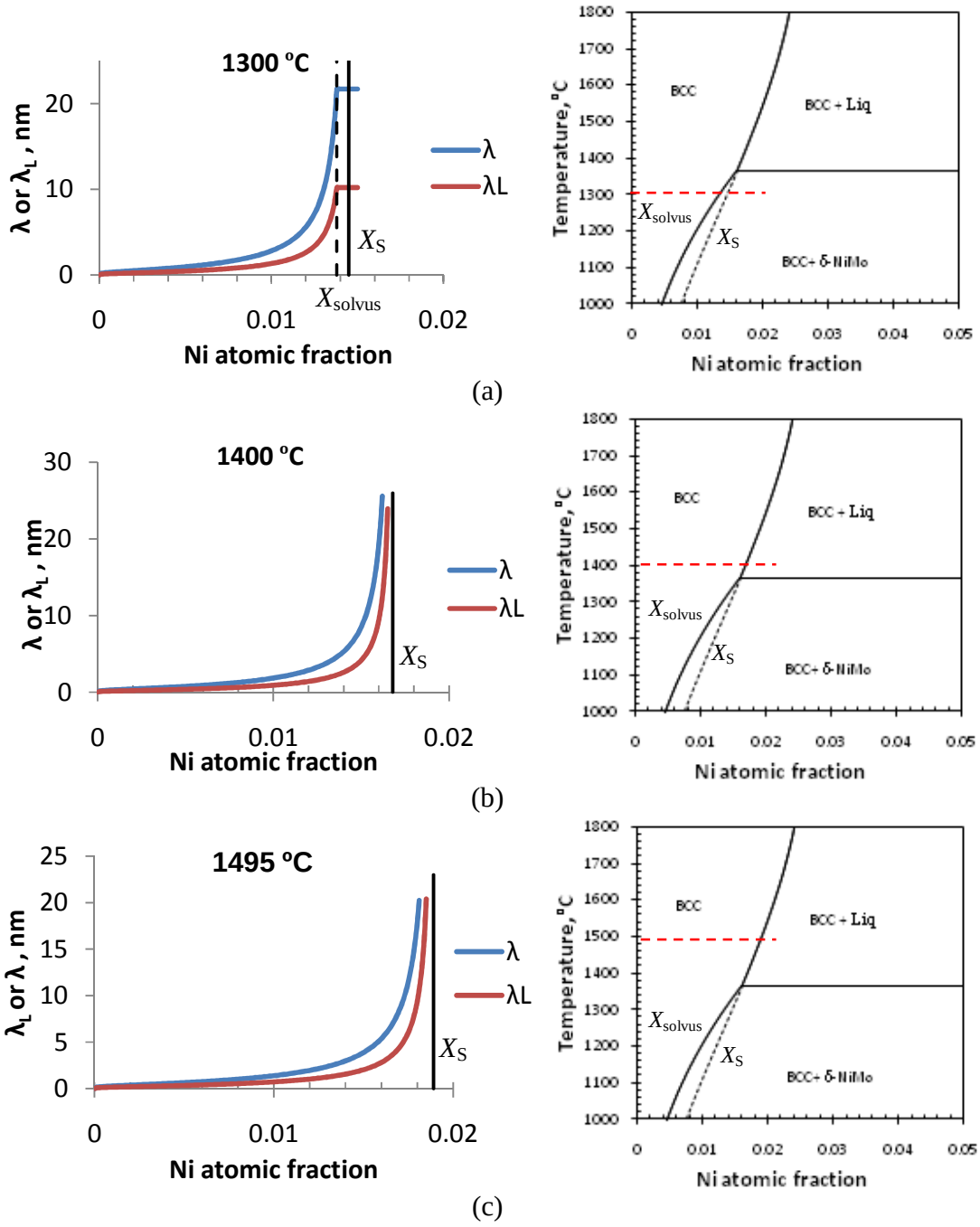


Figure 6.6 Plots of $\lambda_L$ and $\lambda$ vs. Ni atomic fraction and corresponding phase diagrams for 1300 ºC (a), 1400 ºC (b) and 1495 ºC (c). The dashed vertical line in the plot represents bulk solvus composition; the solid vertical line represents bulk solidus composition (or the composition on the metastable extension of the solidus line for 1300 ºC).

### 6.5.2 Computed Grain Boundary Phase Diagram

Furthermore, we plotted lines of constant computed $\lambda_L$ in the bulk phase diagram of the Mo-Ni system. This is a grain boundary phase diagram, where $\lambda_L$ represents the maximum thickness of a quasi-liquid IGF of composition $X_L$ that can be stabilized at Mo GB (an average random GB) without the consideration of interfacial forces and through-thickness compositional and structural gradients. It represents the thermodynamic tendency for a Ni GB to disorder. $\lambda_L$ (or $\lambda$) is not the actual IGF thickness, but it should scale the thickness of the actual (thermodynamically stable) quasi-liquid IGF. For example, as shown in Chapter 5, HRTEM measurement showed that the actual IGF thickness is 0.80 nm at 1495 °C, 1% Ni. This is constant with computed results, where the $\lambda_L$ and $\lambda$ are 0.71 nm and 1.38 nm, respectively. This agreement is rather satisfactory.

In the single-phase region, computed $\lambda_L$ (or $\lambda$) increases with increased bulk composition. Above the peritectic temperature, computed $\lambda_L$ (or $\lambda$) is divergent at the bulk solidus temperature. Below the peritectic temperature, computed $\lambda_L$ (or $\lambda$) levels off at the bulk solvus temperature, and it becomes a constant in the BCC-NiMo two-phase regime. Further model-experimental comparisons will be carried out in Chapter 7.

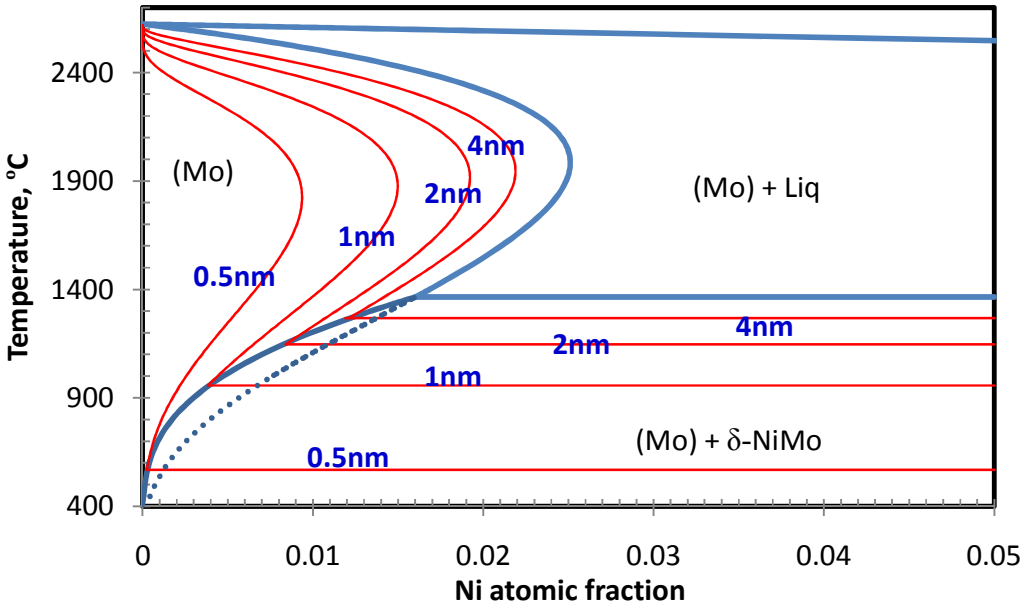


(a)

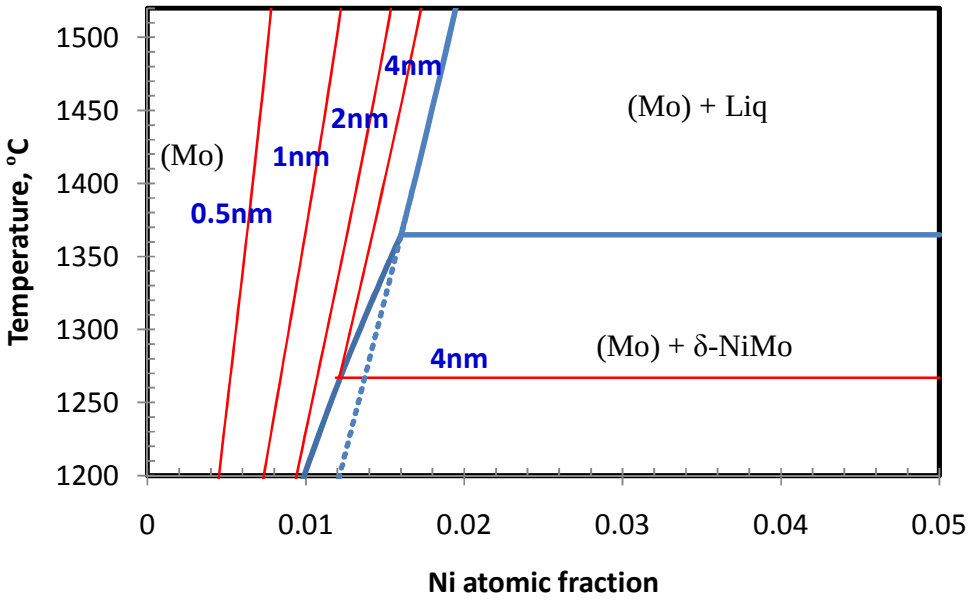


(b)

Figure 6.7 (a) Computed grain boundary diagram with the Ni-doped Mo, where computed lines of constant $\lambda_L$. When the $\lambda_L$ -constant lines approach 0 % Ni vertical axis at the upper left corner, the trend is not correct due to the divergence of calculation at Ni %

=0. (b) Enlarged GB phase diagram of certain area of interest (1200-1500 ºC). Note that $\lambda_L$ is the maximum thickness of a quasi-liquid IGF of composition $X_L$ that can be stabilized at an average (random) Mo GB without the consideration of interfacial forces, and it represents a thermodynamic tendency for a Mo GB to disorder.

References

[1] JG Dash. Surface Melting Contemporary Physics 30 (1989) 89.

[2] JG Dash, H Fu, JS Wettlaufer. The Premelting of Ice and Its Environmental Consequences Reports on Progress in Physics 58 (1995) 115.

[3] JG Dash, AM Rempel, JS Wettlaufer. The Physics of Premelted Ice and Its Geophysical Consequences Reviews of Modern Physics 78 (2006) 695.

[4] J Luo, Y- Chiang, RM Cannon. Nanometer-Thick Surficial Films in Oxides as A Case of Prewetting Langmuir 21 (2005) 7358.

[5] J Luo. Stabilization of Nanoscale Quasi-Liquid Interfacial Films in Inorganic Materials: A Review and Critical Assessment Critical Reviews in Solid State and Material Sciences 32 (2007) 67.

[6] J Luo, X Shi. Grain boundary disordering in binary alloys Appl.Phys.Lett. 92 (2008) 101901.

[7] X Shi, J Luo. Grain boundary wetting and prewetting in Ni-doped Mo Appl.Phys.Lett. 94 (2009)

[8] N Eustathopoulos, MG Nicholas, B Drevet. Wettability at High Tmperatures (1999) 420.

[9] I Shimizu, Y Takei. Thermodynamics of interfacial energy in binary metallic systems: Influence of adsorption on dihedral angles Acta Materialia 53 (2005) 811.

[10] I Shimizu, Y Takei. Temperature and compositional dependence of solid-liquid interfacial energy: Application of the Cahn-Hilliard theory Physica B: Condensed Matter 362 (2005) 169.

[11] R Benedictus, A Böttger, EJ Mittemijer. Thermodynamic Model for Solid-State Amorphization in Binary Systems at Interfaces and Grain Boundaries Physical Review B 54 (1996) 9109.

[12] AR Miedema, FJA den Broeder. On the interfacial energy in solid-liquid and solid-liquid metal combinations Zeitschrift fur Metallkunde 70 (1979) 14.

[13] FR de Boer, R Boom, WCM Mattens, AR Miedema, AK Niessen. *Cohesion in Metals: Transition Metals Alloys*, North-Holland, Amsterdam, 1988.

[14] F Spaepen. A structural model for the solid-liquid interface in monatomic systems Acta Metallurgica 23 (1975) 729.

[15] F Spaepen, RB Meyer. The surface tension in a structural model for the solid-liquid interface Scripta Metallurgica 10 (1976) 257.

[16] P Wynblatt, D Chatain. Anisotropy of segregation at grain boundaries and surfaces Metallurgical and Materials Transactions A (Physical Metallurgy and Materials Science) 37A (2006) 2595.

[17] D Chatain, C Antion. Liquid surface and liquid/liquid interface energies of binary subregular alloys and wetting transitions Surf.Sci. 601 (2007) 2232.

[18] N Saunders, AP Miodownik. CALPHAD (Calculation of Phase Diagram): a comprehensive guide, Pergamon, New York, 1998.

[19] K Frisk. Thermodynamic evaluation of the Mo-Ni system Calphad 14 (1990) 311.

[20] SH Zhou, Y Wang, C Jiang, JZ Zhu, L- Chen, Z- Liu. First-principles calculations and thermodynamic modeling of the Ni-Mo system Materials Science and Engineering A 397 (2005) 288.

[21] TB Massalski, H Okamoto. Binary Alloy Phase Diagrams, ASM International, Ohio., 1990.

[22] TB Massalski, JL Murray, LH Bennett, H Baker. Binary alloy phase diagrams (1986) 2224.

[23] SL Kang, Y Song, WA Kaysser, H Hofman. Z. Metallkd. 75 (1986) 86.

[24] REW Casselton, W Hume-Rothery. J. Less-Common Metals 7 (1964) 212.

# CHAPTER SEVEN
# ACTIVATED SINTERING AND QUASI-LIQUID INTERGRANULAR FILMS IN NI-DOPED MO

## 7.1 Motivation

The existence of liquid-like IGFs in the Ni-Mo binary system had been confirmed by HRTEM and AES (Chapter 5) and a simplified thermodynamic model was discussed elaborately in Chapter 6. It is now widely accepted that liquid-like IGFs in oxide- [1] and tungsten- [ref] based systems have high GB diffusivity and result in subsolidus-activated sintering. In this chapter, we investigated the sintering behaviors of Ni-doped Mo, and extracted GB diffusivities systematically through a series of controlled sintering experiments. We expect a strong correlation between the formation of liquid-like IGFs and enhancing GB diffusion rates (therefore the rates of subsolidus-activated sintering). The objectives are two-fold:

- We extract GB diffusivities via controlled sintering experiments to provide indirect, yet systematical, experimental evidence to prove the thermodynamic model and computed GB diagram presented in Chapter 6.
- Good model-experimental agreements provide further evidence to previously proposed activated sintering mechanisms, i.e., the subsolidus accelerated sintering is due to the enhanced diffusion in quasi-liquid IGFs.

## 7.2 Controlled Sintering Experiments

As was mentioned before, the experiments were described in detail in Chapter 2. A presintering procedure (1000 ºC, 1 hour) was adopted before isothermal sintering to homogenize the system. The XRD confirmed that all the Ni was transformed to δ-NiMo compound, which is a good sign of homogeneity (Fig. 7.1). This also excludes the possibility of transient liquid during the next step of isothermal sintering. The linear shrinkage during presintering is tiny (< 1%), and such small "pre-existing" shrinkages are negligible for analyzing the kinetics of the subsequently isothermal sintering experiments.

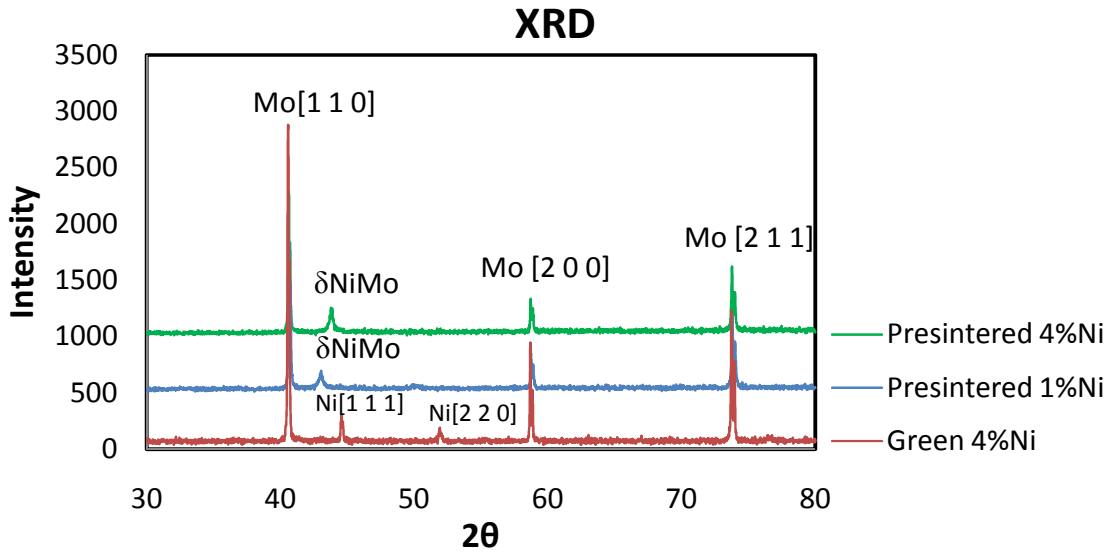


Figure 7.1 XRD spectrum of Ni-doped Mo. Almost all the Ni has been transformed to δ-NiMo compound after presintering at 1000 ºC for 1 hour.

For the controlled isothermal sintering experiments, sintering temperatures were set to 1220 ºC, 1300 ºC, 1350 ºC, 1400 ºC, 1450 ºC, and 1495 ºC (while the peritectic

temperature is 1362 ºC). Different Ni atomic fractions were selected so that they covered both BCC single-phase regime and BCC-liquid or BCC-Mo-NI two-phase regimes. The selection of these experimental conditions is schematically illustrated Fig. 7.2.

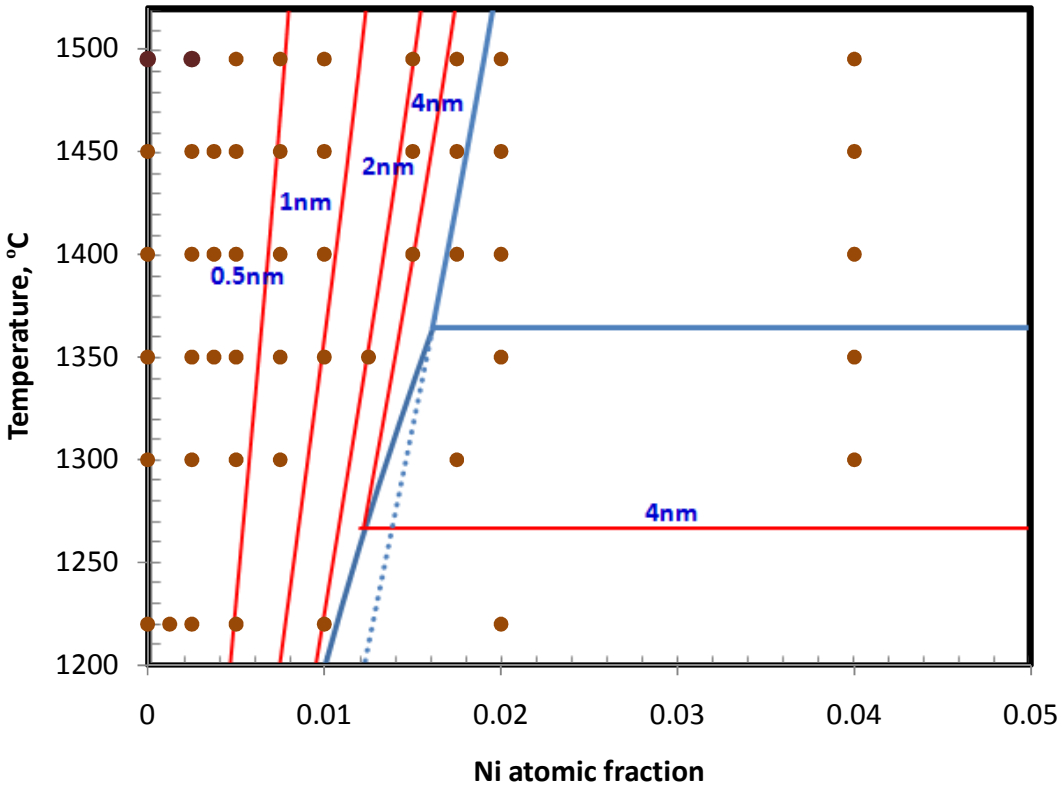


Figure 7.2 The selected sintering temperatures and compositions are marked in the Mo-Ni binary phase diagram.

## 7.3 Sintering Data—Densification and Grain Growth

### 7.3.1 Densification Data

The densification data of isothermal sintering at eight temperatures and plots of relative density vs. sintering time and linear shrinkage vs. sintering time are documented in Section "7.9 Appendix: Raw Densification Data". Several representative plots of relative density vs. sintering time are shown in Fig. 7.3-7.4.

The error bars were determined using the following methods: Due to experimental limitations (a large number of experimental conditions), we could not make/measure multiple specimens for each experimental condition (a specific set of temperature, composition, and time). We selected a few representative conditions (e.g., pure and 1.5 at. % Ni doped Mo at different temperatures and sintering time) to prepare 3-4 specimens to obtain means and standard deviations of the measured densities (to represent specimen-to-specimen variations). Based on these measurements, we found that the standard deviation is about 0.005 of the relative density (or 0.0013 in the linear shrinkage, $\Delta L/L0$) for specimens generally. These error bars were then used as estimated errors bars for other measurements.

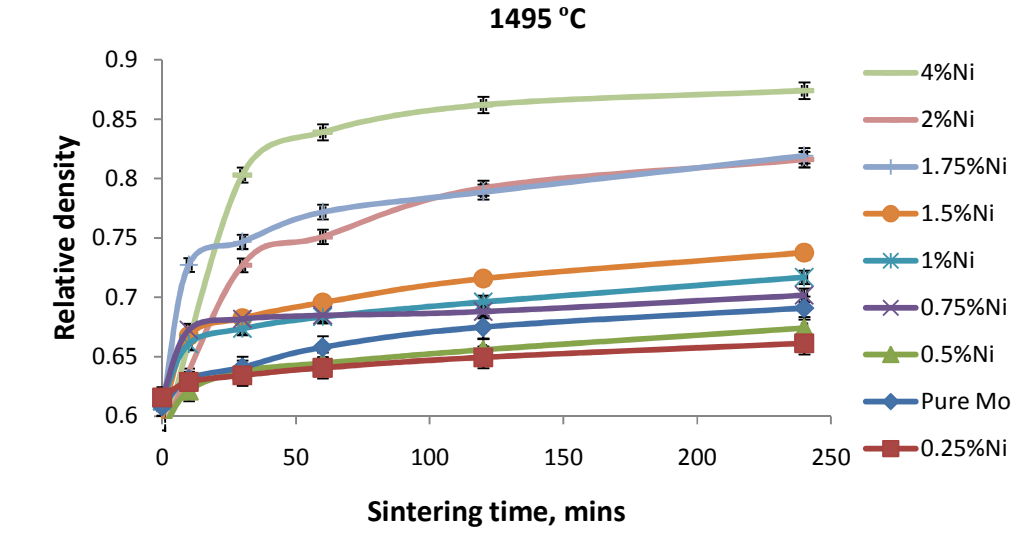


(a)

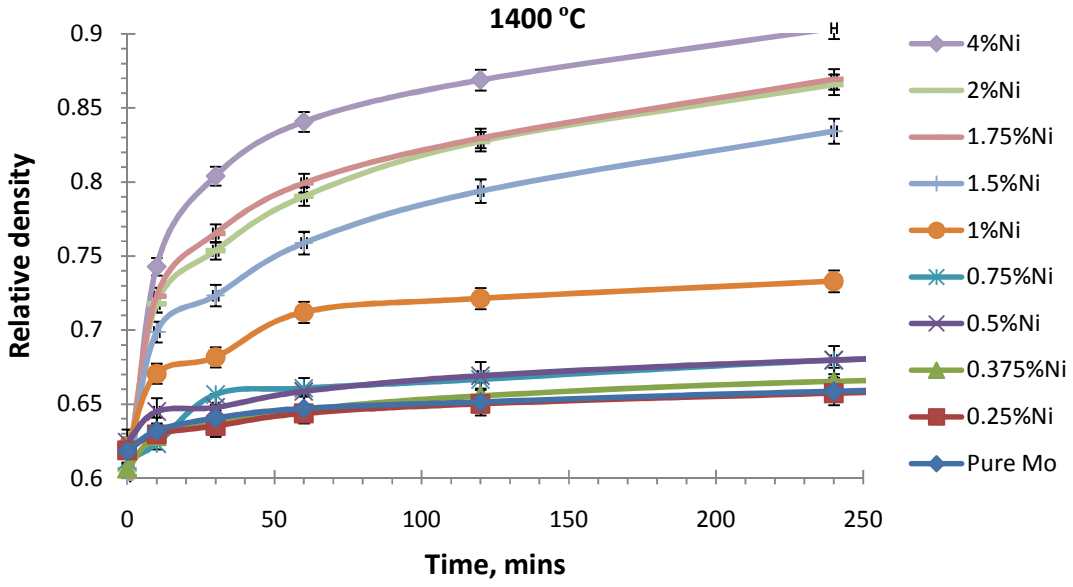


(b)

Figure 7.3 Representative plots of relative density vs. sintering time at (a) 1490 ºC and (b) 1400 ºC (both above $T_{preitectic}$ = 1362 ºC). Additional plots at other temperatures and the raw data are shown in §7.9.

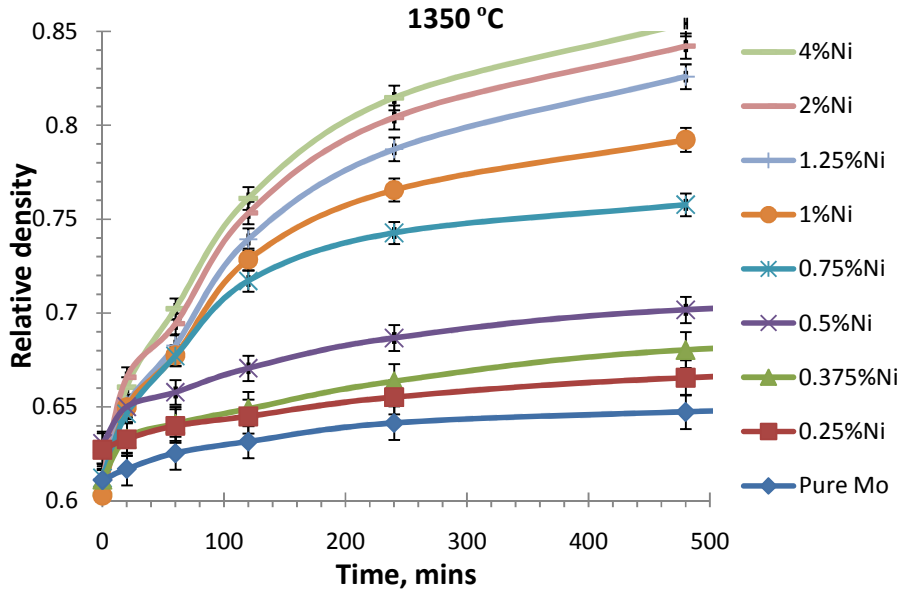


(a)

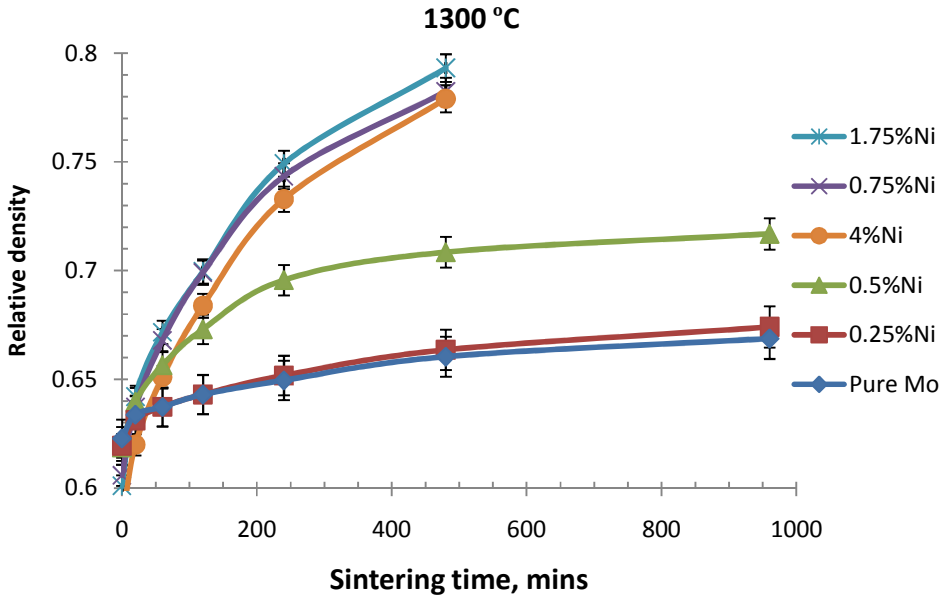


(b)

Figure 7.4 Representative plots of relative density vs. sintering time at (a) 1350 ºC and (b) 1300 ºC (both below $T_{preitectic}$ = 1362 ºC). Additional plots at other temperatures and the raw data are shown in §7.9.

As shown in Fig. 7.3 & 7.4, the plots of relative density vs. sintering time show consistent trends: the densification rate generally increases with increasing Ni content or temperature. This data was further analyzed to extract GB diffusivity as a function of temperature and overall composition. Then, critical comparisons with the computed GB diagram, reported in Chapter 6, were carried out.

### 7.3.2 Grain Growth Data

The measured grain sizes of samples with different Ni contents and sintering temperatures are shown in Table 7.2. As shown in Table 7.2, the grain growth is almost negligible (within the range of experimental errors) for moderate doping level (≤ 1.5 at % Ni) or at low temperatures (≤ 1300 ºC). For the regime where the grain growth is not negligible (the region that is the left-bottom corner by the red line in Table 7.2), the effects of grain growth must be considered in extracting the GB diffusivity data via fitting the sintering models. This issue will be discussed subsequently.

Table 7.1 Measured grain sizes of Ni-doped Mo samples sintered at different temperatures for different times.

| Ni at. % | Sintering temperature, ºC | 1300 ºC | 1400 ºC | 1450 ºC | 1495 ºC |
|---|---|---|---|---|---|
| | Sintering time, mins | Grain size, µm | Grain size, µm | Grain size, µm | Grain size, µm |
| 1 | 0 | 22.3 ± 7.0 | 22.3 ± 7.0 | 22.3 ± 7.0 | 22.3 ± 7.0 |
| | 180 | ---------- | ---------- | ---------- | 24.4 ± 5.3 |
| | 360 | ---------- | ---------- | ---------- | 28.0 ± 5.4 |
| 1.5 | 0 | 25.51 ± 11.0 | 25.51 ± 11.0 | 25.51 ± 11.0 | 25.51 ± 11.0 |
| | 60 | ---------- | ---------- | ---------- | 26.6 ± 5.4 |
| | 120 | ---------- | 23.0 ± 3.3 | ---------- | ---------- |
| | 240 | ---------- | ---------- | 24.2 ± 3.6 | 26.3 ± 6.2 |
| 1.75 | 0 | 26.0 ± 8.6 | 26.0 ± 8.6 | 24.0 ± 7.2 | 26.0 ± 8.6 |
| | 30 | ---------- | ---------- | ---------- | 25.9 ± 4.3 |
| | 60 | ---------- | 28.8 ± 4.1 | ---------- | 26.1 ± 6.5 |
| | 120 | ---------- | 32.6 ± 5.0 | 35.1 ± 3.6 | 40.5 ± 8.0 |
| | 240 | ---------- | 58.2 ± 12.5 | 56.5 ± 7.5 | 55.2 ± 7.0 |
| 2 | 0 | 29.6 ± 9.6 | 29.6 ± 9.6 | 29.6 ± 9.6 | 29.6 ± 9.6 |
| | 60 | ---------- | 35.5 ± 5.1 | ---------- | ---------- |
| | 120 | ---------- | 45.9 ± 8.1 | ---------- | ---------- |
| | 150 | 23.0 ± 4.1 | 52 ± 8.1 | 60.0 ± 9.8 | 64.9 ± 7.8 |
| 4 | 60 | ---------- | 33.8 ± 5.1 | ---------- | ---------- |
| | 120 | ---------- | 54.6 ± 6.0 | ---------- | ---------- |
| | 240 | ---------- | 64.7 ± 9.4 | ---------- | ---------- |

## 7.4 Determination of the Controlling Densification Mechanism

The GB diffusivity can be extracted from sintering data only if the densification is controlled by GB diffusion. We can determine whether densification is controlled by GB diffusion (vs. bulk diffusion) by obtaining the exponent *m* for the power law fitting of the initial stage densification kinetics. According to Johnson's model [2] and Kang's sintering theory [3], the linear shrinkage ($\Delta L/L_0$) in the initial stage follows a power law:

$$\frac{\Delta L}{L_0} = \left[ K \frac{\gamma_s \Omega D}{kTG^p} \right]^m t^m \quad . \tag{7.1a}$$

The experimentally-fitted exponent number *m* can be used to discriminate which sintering mechanism is in control [2]. If *m* = ~0.4-0.5, the densification is controlled by bulk diffusion, where *K* = 6, *p* = 3, and $D = D_{XL}$. Eq (7.1a) becomes

$$\frac{\Delta L}{L_0} = \left[ 6 \frac{\gamma_s \Omega D}{kTG^3} \right]^{1/2} t^{1/2}. \tag{7.1b}$$

If *m* = ~0.33, the densification is controlled by GB diffusion, where *K* = 12, *p* = 4, and $D = \delta D_{GB}$. Eq (7.1a) becomes

$$\frac{\Delta L}{L_0} = \left[ 12 \frac{\gamma_s \Omega D}{kTG^4} \right]^{1/3} t^{1/3}. \tag{7.1c}$$

The index *m* can be determined experimentally by finding the slope of the double logarithmical plot of linear shrinkage vs. time (as illustrated in Fig. 7.11) linear regression. Note that Eq. 7.1 can only be applied to the initial stage of sintering where $\Delta L/L_0 < 4\%$.

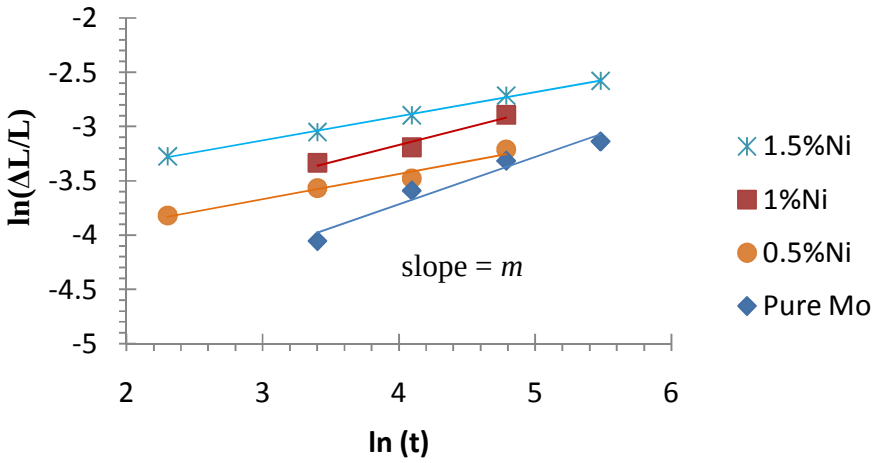


Figure 7.5 Double logarithmical plot of linear shrinkage vs. sintering time for samples with different Ni atomic percent sintering at 1495 ºC. The slopes correspond to the exponents (*m*).

The index *m*'s were calculated and listed in Table 7.2. The highlighted samples show bulk diffusion-controlled whereby GB diffusivity was not measurable; otherwise they are GB diffusion-controlled whereby determination of GB diffusivity is possible.

Table 7.2 Index *m* of sintering at different temperatures

| Ni % / Index *m* | Pure Mo | 0.25% | 0.5% | 1.0% | 1.5% |
|---|---|---|---|---|---|
| 1495 ºC | 0.44 ± 0.06 | 0.37 ± 0.02 | 0.23 ± 0.03 | 0.32 ± 0.02 | 0.22 ± 0.03 |
| 1450 ºC | 0.31 ± 0.11 | 0.23 ± 0.03 | 0.22 ± 0.03 | 0.29 ± 0.02 | 0.20 ± 0.03 |
| 1400 ºC | 0.29 ± 0.06 | 0.24 ± 0.01 | 0.26 ± 0.02 | 0.25 ± 0.04 | 0.23 ± 0.07 |
| 1350 ºC | 0.28 ± 0.03 | 0.23 ± 0.03 | 0.31 ± 0.02 | 0.36 ± 0.03 | -------- |
| 1300 ºC | 0.29 ± 0.06 | 0.23 ± 0.02 | 0.28 ± 0.07 | --------- | -------- |
| 1220 ºC | 0.29 ± 0.06 | 0.35 ± 0.03 | 0.26 ± 0.07 | 0.33 ± 0.08 | -------- |

All the experimental points are shown in Ni-Mo GB phase diagram of Fig. 7.12. The solid dots represent cases where densification is controlled by GB diffusion whereby GB diffusivities are measurable through sintering experiments, while “X” represents the cases where the densification is controlled by bulk diffusion (i.e., bulk diffusion contributes more to densification than GB diffusion) so that GB diffusivity cannot be determined. This mechanism map is consistent with prior reports [4].

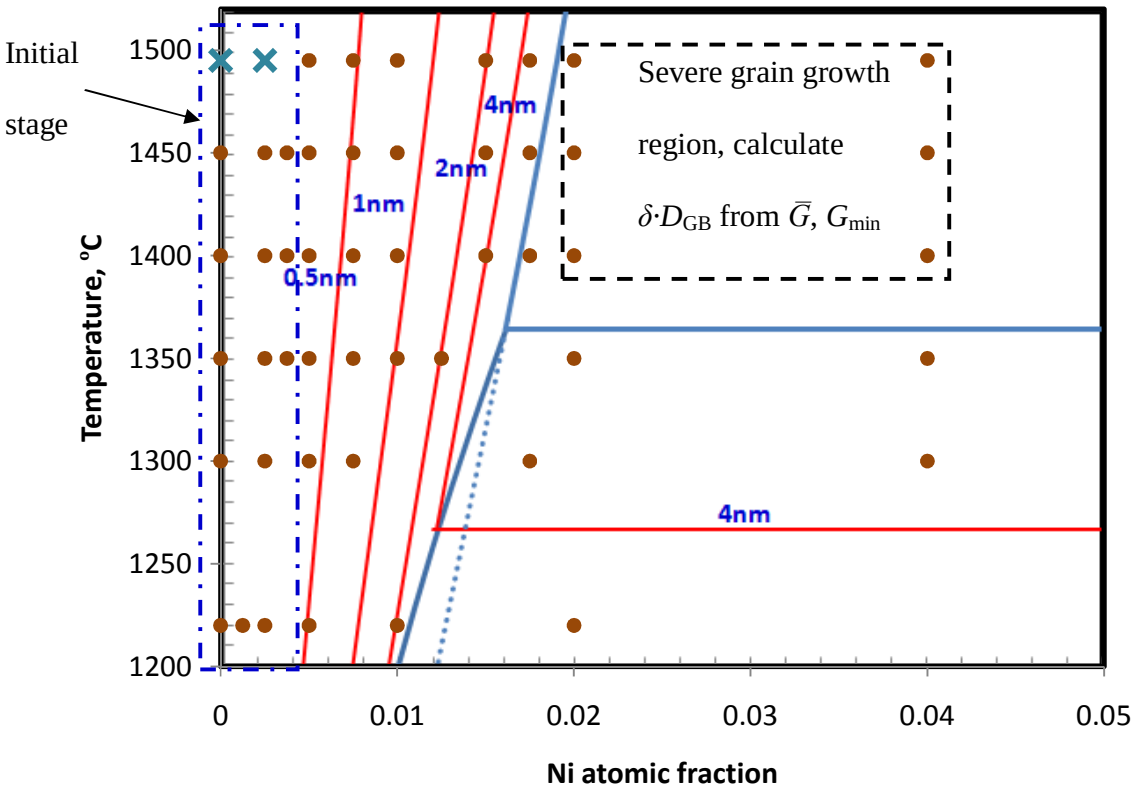


Figure 7.6 The GB diagram for Ni-doped M, in which the experimental conditions are marked. Blue crosses indicate that densification is controlled by bulk diffusion, while brown solid dots indicate that densification is controlled by GB diffusion. GB diffusivity in the solid-dashed line enclosed region is determined by the initial stage model; the rest of them are obtained from the intermediate stage model; the dashed line encloses the region where grain growth is not negligible and average grain size is adopted for calculation.

## 7.5 Determination of GB Diffusivity

The sintering models were discussed systematically in Chapter 2. In this section, we explain a detailed procedure to determine GB diffusivity. The intermediate-stage

sintering data (linear shrinkage > 4%) are used to fit the well-known Coble model (Eq. (7.2)) because the densification is significant while grain growth is limited in this stage. Consequently, the fitted GB diffusivity is more accurate (as compared with that which is obtained from the initial stage data). In the case of pure Mo and low doping level (Ni atomic % < 0.5), when the total densification is not sufficient to apply the intermediate-stage sintering model, the initial stage sintering data were fitted with the initial stage model (Eq. (7.1c)) described above to obtain GB diffusivity alternatively. This includes the following cases as labeled in Fig. 7.12.

### 7.5.1 Solid-State Sintering

In Coble's model for the intermediate stage sintering, the GB-diffusion controlled densification rate is expressed as [3,5]:

$$\frac{dP^{\frac{3}{2}}}{dt} = -1281\frac{\delta D_{GB}\gamma_s\Omega}{kTG^4}, \tag{7.2}$$

where $P$ (= 1-$\rho_r$; $\rho_r$ is the relative density) is porosity; $D_{GB}$ is GB diffusivity; $\gamma_s$ is surface energy of Mo (estimated to be ~3 J/m$^2$); $\Omega$ is atomic volume of vacancy ($1.56\times10^{-29}$); $k$ is Boltzmann constant; and $G$ is grain size. If the grain size is almost a constant during the intermediate stage sintering, integration of Eq. (7.2) leads to

$$\left(P\right)^{\frac{3}{2}} - \left(P^0\right)^{\frac{3}{2}} = -[1281\frac{\delta D_{GB}\gamma_s\Omega}{kTG^4}t]. \tag{7.3}$$

Based on Eq. 7.3, the slope ($\beta$) in $P^{3/2}$ vs. $t$ can be obtained by linear regression. Then, the GB diffusivity ($\delta \cdot D_{GB}$) is calculated to be

$$\delta \cdot D_{GB} = \frac{\beta kTG^4}{-1281\gamma_s \Omega}. \tag{7.4}$$

If grain growth cannot be neglected, we use the average grain size in the above Eq. and estimate an additional error from initial/final grain size.

As mentioned before, for pure Mo and a limited number of other cases of low doping samples, it was difficult to reach the intermediate stage within a reasonable time. Therefore, we also used Johnson's initial stage to determine GB diffusivity. Based on Eq. (7.1c) the plot of $(\Delta L/L_0)^3$ *vs.* $t$ was created and a linear regression was implemented to obtain the slope ($\beta_0$). Since Eq. (7.1c) can be rewritten as:

$$(\frac{\Delta L}{L_0})^3 = (12\frac{\gamma_S \Omega \cdot \delta D_{GB}}{kTG^4})t + (12\frac{\gamma_S \Omega \cdot \delta D_{GB}}{kTG^4})t_0 . \tag{7.6}$$

Since we applied a presintering treatment before isothermal sintering, the time $t_0$ in Eq. (7.6) accounted for any equivalent densification during presintering (based on Master Sintering Curve (MSC) theory [6]) although it was generally negligible ( < 1%). Upon knowing slope $\beta_0$, GB diffusivity is given by:

$$\delta D_{GB} = \frac{\beta_0 kTG^4}{12\gamma_S \Omega} . \tag{7.7}$$

It appeared that Eqs. (7.4) and (7.7) adopted a similar form.

In a few cases where both initial and intermediate stage sintering data are available, we compared the GB diffusivities extracted from the Johnson model (Eq. 7.7)) and the Coble model (Eq. (7.4)) in § 7.6.1, and we found the agreement to be reasonably good.

### 7.5.2 Liquid-Phase Sintering

The densification for liquid-phase sintering follows the model that was developed by Kingery [7,8] and improved by German [9]:

$$d(\frac{\Delta L}{L_0})^3 = 192\frac{\delta_L D_{GBL}\gamma_s \Omega C}{kTG^4}dt \tag{7.8}$$

where $\delta_L$ represents the thickness of the liquid film; $D_{GBL}$ is the diffusivity of solute in liquid phase that wets the GB; and $C$ is the solubility of primary element in liquid phase. Note that this Equation is conceptually the same as Eq. (7.2) except that $\delta \cdot D_{GB}$ is replaced by $\delta_L \cdot D_{GBL} \cdot C$ . Thus, in this study, we will use the same solid-state Equation to fit a nominal $\delta \cdot D_{GB}$ to ensure fair comparison. Note that this approach does not consider the effects of particle re-arrangement, which can be significant for liquid-phase sintering. Because there was grain growth during liquid sintering, we adopted average grain size as the constant and plugged it into Eq. 7.3 for simplicity. In addition, we employed the minimum and maximum grain size as the lower and upper limit to estimate error bar.

### 7.5.2 Error Estimation

According to error propagation theory [10], if $y = f(x_1, x_2)$ and $x_1$, $x_2$ have variances $\delta x_1^2$ and $\delta x_2^2$ respectively, the variance of $y$ ($\delta y^2$) can be estimated by

$$\delta y^2 = (\frac{\partial f}{\partial x_1})^2 \delta x_1^2 + (\frac{\partial f}{\partial x_2})^2 \delta x_2^2 . \tag{7.10}$$

We used the above Equation to estimate the error bars of $\delta D_{GB}$. For extracting GB diffusivity from the intermediate-stage data, the estimation gives:

$$\mathrm{var}^2(\delta D_{GB}) = \left[\frac{kTG^4}{-1281\gamma_S\Omega}\right]^2 (\Delta\beta)^2 + \left[\frac{4\beta kTG^3}{-1281\gamma_S\Omega}\right]^2 (\Delta G)^2 . \quad (7.11)$$

For extracting GB diffusivity from the initial-stage data, the estimation gives:

$$\mathrm{var}^2(\delta D_{GB}) = \left[\frac{kTG^4}{-1281\gamma_S\Omega}\right]^2 (\Delta\beta_0)^2 + \left[\frac{4\beta_0 kTG^3}{-1281\gamma_S\Omega}\right]^2 (\Delta G)^2 . \quad (7.12)$$

Here the variance of grain size is neglected due to the lesser amount of grain growth in the initial stage.

## 7.6 Experimental Results

### 7.6.1 Comparison of Johnson, Coble and German Models

For a few cases where both initial and intermediate stage sintering data exist, both Johnson (initial stage) and Coble (intermediate stage) models are used to extract GB diffusivities and the results are listed in Table 7.4. It appears that GB diffusivities determined by both models are quite consistent.

Table 7.3 GB diffusivities extracted from Johnson's initial stage model and Coble's intermediate stage model.

| *T*, ºC | 1220 | 1300 | 1350 | 1400 | 1450 | 1495 |
|---|---|---|---|---|---|---|
| Ni at. % | 0.25 | 0.5 | 0.5 | 0.5 | 0.75 | 0.5 |
| Initial stage | 1.89E-18 | 0.97E-17 | 4.81E-18 | 7.13E-18 | 1.74E-17 | 9.27E-18 |
| Intermediate stage | 1.34E-18 | 1.20E-17 | 4.96E-18 | 6.01E-18 | 2.36E-17 | 3.18E-18 |

Additionally, we compared the GB diffusivities for liquid-phase sintering determined by German's model (Eq. 7.8) and nominal value obtained through Coble's model (Eq. 7.2) in Table 7.4. In previous sections, it has been briefly discussed that these two models were essentially equivalent.

Table 7.4 GB diffusivities of liquid-phase sintering determined by using German's and Coble's model.

| Temperature, ºC | 1450 | 1450 | 1495 | 1495 |
|---|---|---|---|---|
| Ni at. % | 2 | 4 | 2 | 4 |
| German's model | 5.21E-16 | 9.69E-16 | 6.70E-16 | 1.58E-15 |
| Coble's model | 9.84E-16 | 13.7E-16 | 9.86E-16 | 1.21E-15 |

From Table 7.5, we can tell that the calculated results from these two models are consistent. It indicates that neglecting the effects of particle re-arrangement does not significantly influence the calculated results.

### 7.6.2 Dependence of $\delta \cdot D_{GB}$ on Ni Amount

It has been shown that sintering of pure Mo and lower doping level samples at 1495 ºC is bulk diffusion-controlled. Accordingly, Fig. 7.13 shows the gray area where GB diffusivity was not measurable. A discontinuous jump of GB diffusivity was spotted when the Ni atomic % increased from 0.5% to 1%. Correspondingly, the quasi-liquid nanoscale IGF was observed for 1% Ni doped Mo by HRTEM. While Ni atomic percent passed the bulk solidus line, GB diffusivity experienced another jump between 1.75% and 2% due to the GB complete wetting (Fig. 5.1(b) in Chapter. 5).

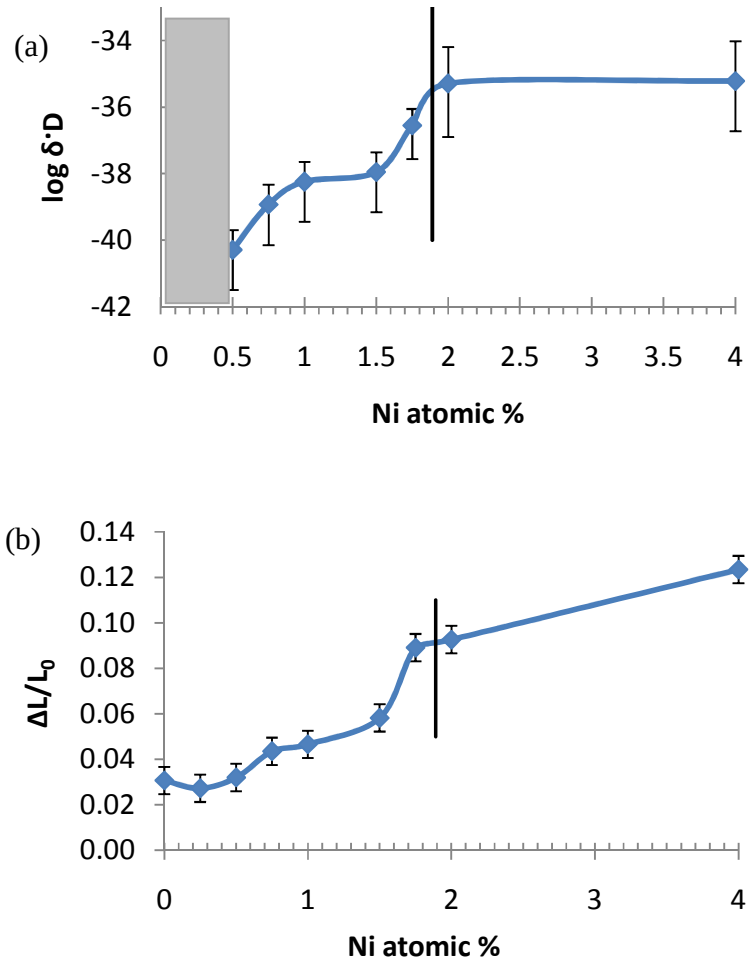


Figure 7.7 (a) Plot of GB diffusivity *vs* Ni atomic percent at 1495 ºC; (b) plot of linear shrinkage after 1 hour sintering *vs* Ni atomic percent at 1495 ºC. The black vertical lines represent bulk solidus composition.

To obtain the full range profile of dependence of GB diffusivity on Ni atomic %, lower sintering temperatures were chosen (1220 ºC, 1300 ºC, 1350 ºC, 1400 ºC and 1450 ºC, as shown in Fig. 7.6). Based on the previous observation [4], sintering of Ni-doped Mo is GB diffusion control in the temperature of 1100-1400 ºC. The indexes *m* of

sintering at these temperatures listed in Table 7.2 indicated that they are mostly GB diffusion controlled sintering.

The full range of GB diffusivity and linear shrinkage rate are plotted against Ni atomic % in Fig. 7.8-7.12 for five selected sintering temperatures.

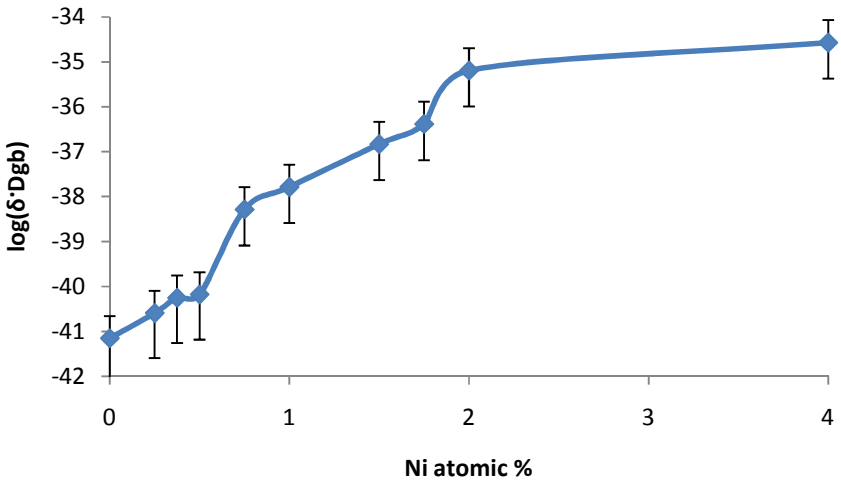


(a)

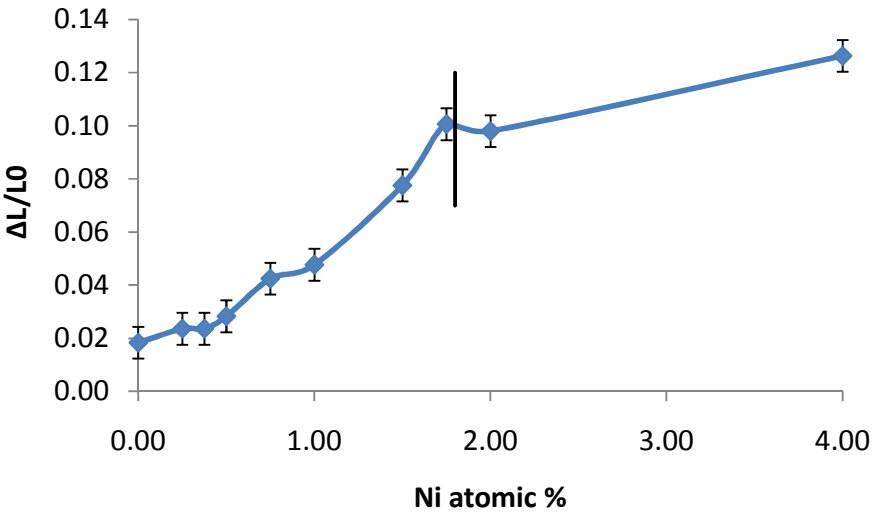


(b)

Figure 7.8 (a) GB diffusivity and (b) linear shrinkage after 1 hour sintering *vs* Ni atomic percent at 1450 ºC. The black vertical lines represent the bulk solidus composition.

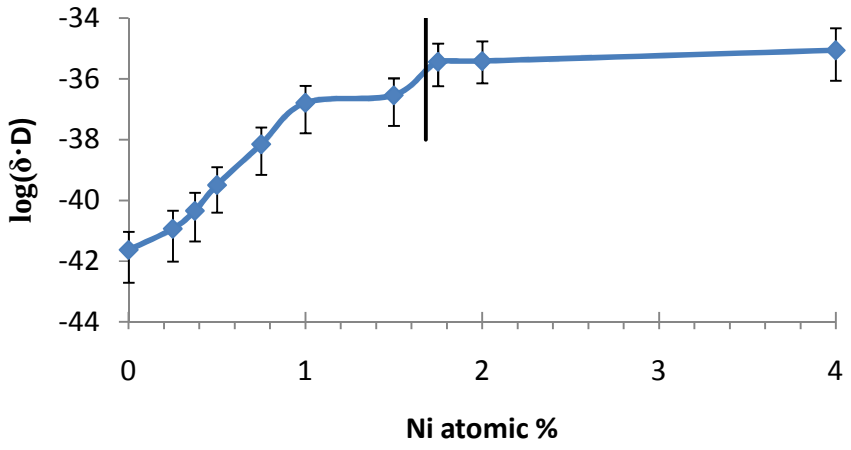


(a)

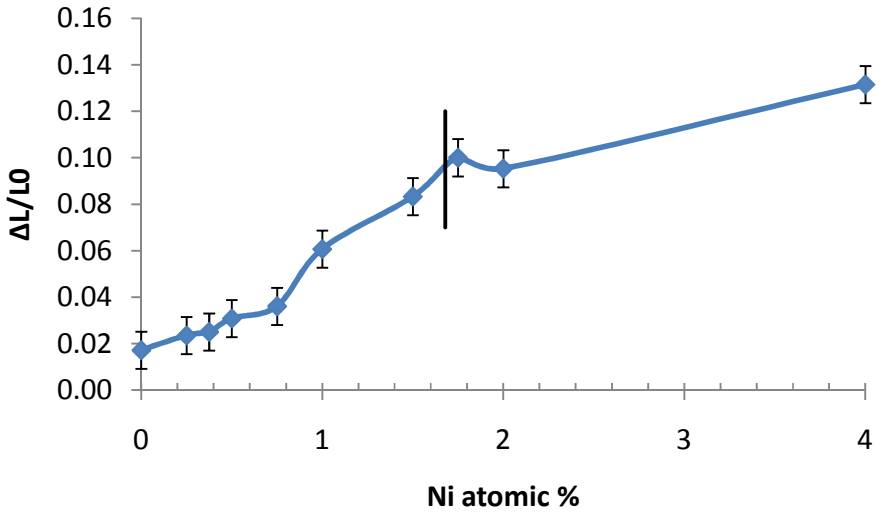


(b)

Figure 7.9 (a) Plot of GB diffusivity *vs* Ni atomic percent at 1400 ºC; (b) plot of linear shrinkage after 1 hour sintering *vs* Ni atomic percent at 1400 ºC. The black vertical lines represent bulk solidus composition.

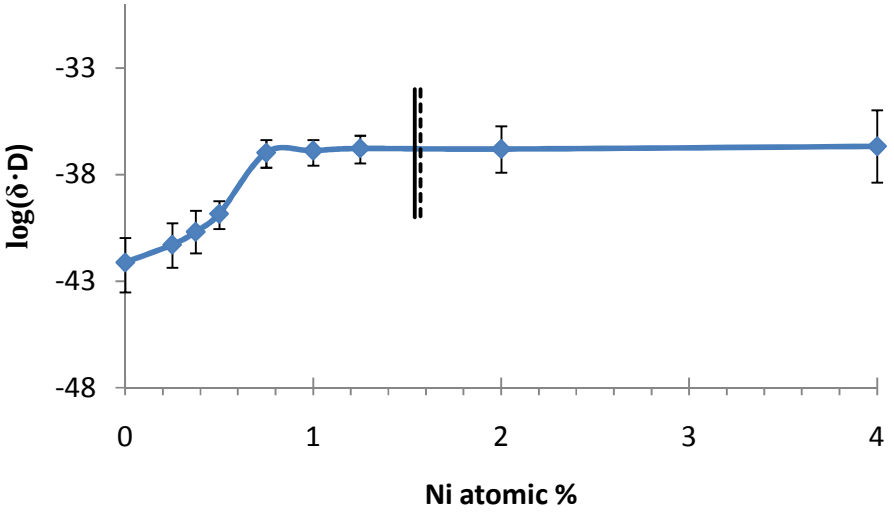


(a)

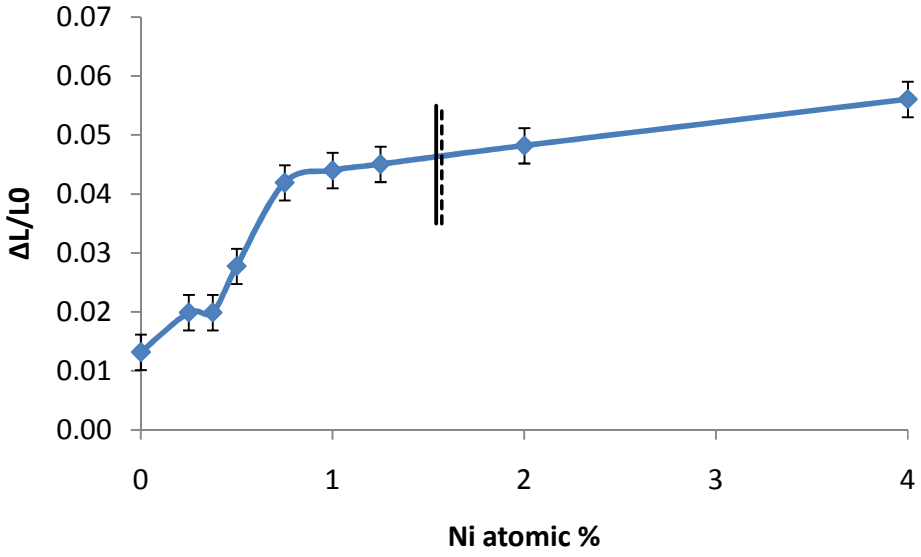


(b)

Figure 7.10 (a) Plot of GB diffusivity *vs* Ni atomic percent at 1350 ºC; (b) plot of linear shrinkage after 1 hour sintering *vs* Ni atomic percent at 1350 ºC. The solid vertical lines represent bulk solvus composition and dashed vertical lines represent metastable solidus composition.

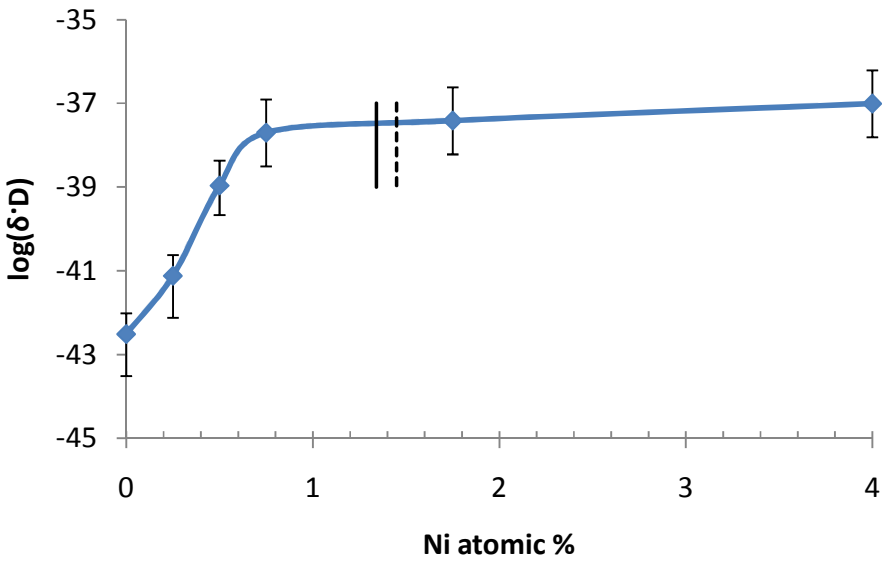


(a)

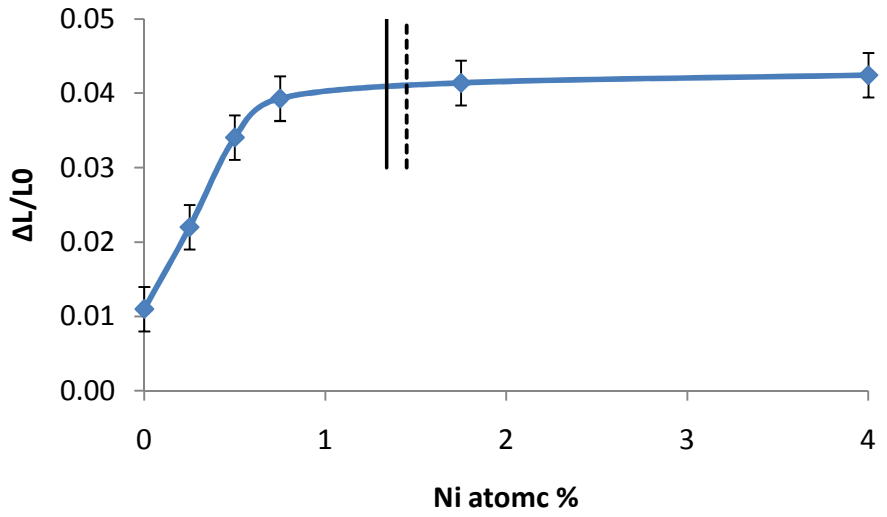


(b)

Figure 7.11 (a) Plot of GB diffusivity *vs* Ni atomic percent at 1300 ºC; (b) plot of linear shrinkage after 1 hour sintering *vs* Ni atomic percent at 1300 ºC. The solid vertical lines represent bulk solvus composition and dashed vertical lines represent metastable solidus composition.

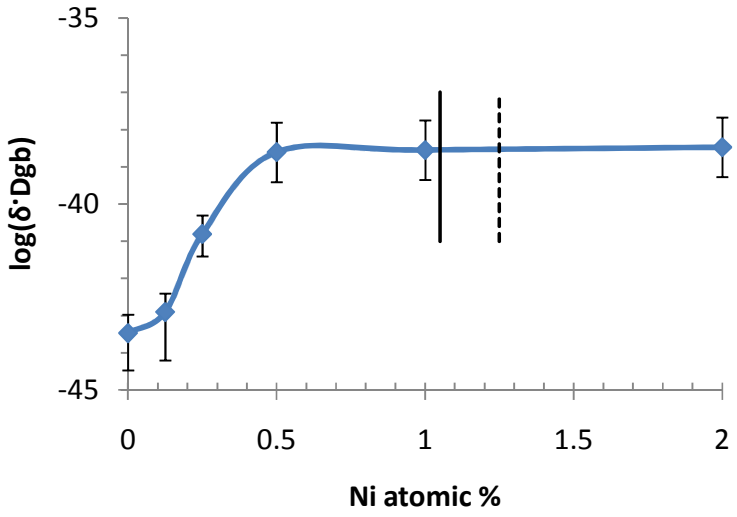


(a)

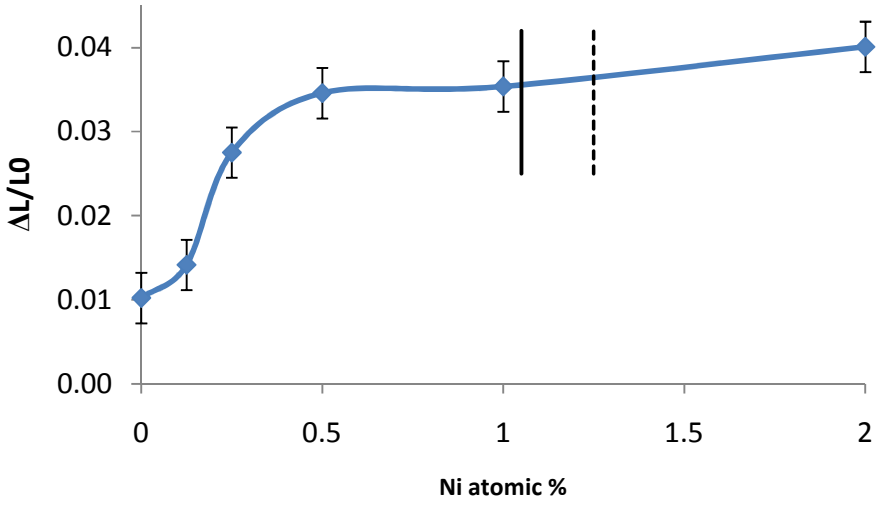


(b)

Figure 7.12 (a) Plot of GB diffusivity *vs* Ni atomic percent at 1220 ºC; (b) plot of linear shrinkage after 2 hour sintering *vs* Ni atomic percent at 1220 ºC. The solid vertical lines represent bulk solvus composition and dashed vertical lines represent metastable solidus composition.

From the above figures, several characteristics can be observed:

- The same jump of the GB diffusivities due to the formation of quasi-liquid IGF is observed in all these plots with the change of Ni atomic percent.
- For $T > T_{peritectic}$ (1400 ºC and 1450 ºC), when the Ni doping level passes the bulk solidus line, GB diffusivity shows another jump due to the GB complete wetting.
- For $T < T_{peritectic}$ (1220 ºC , 1300 ºC and 1350 ºC), when the Ni doping level passes the bulk solvus line, GB diffusivity almost levels off. Accordingly, $\lambda_L$ becomes constant in sub-peritectic two-phase regime.

Accordingly, Fig. 7.13 shows an example of how sintering correlates with modeling.

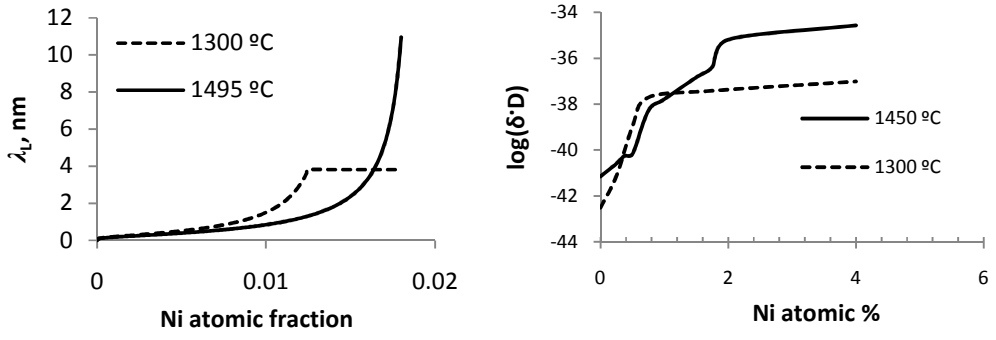


Figure 7.13 (a) Plot of $\lambda_L$ vs. Ni atomic fraction at temperature of 1300 ºC and 1495 ºC; (b) plot of GB diffusivities vs. Ni atomic fraction for sintering at the same temperatures.

### 7.6.3 Effect of Temperature on GB Diffusivity

Based on the data above, we compared the trend of GB diffusivities' change with Ni atomic percent for different temperatures. In another way, the dependence of GB diffusivities on temperature can also be investigated by comparing GB diffusivities of different temperature with same Ni atomic percent. By choosing the same Ni atomic percent, the effect of temperature on GB diffusivity can be examined in both sub-peritectic two-phase regime and subsolidus single-phase regimes.

Interestingly, in the sub-peritectic two-phase regime, it is found evidently that:

- The GB diffusivities of 2 atomic % Ni-doped Mo experiences a jump due to the GB complete wetting (Fig. 14(a)).
- The GB diffusivity becomes larger with increasing sinter temperature in range of 1100 ºC to 1350 ºC (Fig. 14(a)). This correlates well with the model prediction (Fig. 14(b)).
- At temperature lower than 1100 ºC, bulk diffusion became the dominant mechanism because index *m* switched from 0.356 to 0.495.

The first jump of GB diffusivity dependence on temperature, like what is observed in Ni atomic % dependence, cannot be determined through this controlled sintering experiment. However, in terms of our model prediction and coincidence of GB diffusivity jump with $\lambda_L$ = 0.5 nm line, the temperature where the transition would happen can be extrapolated to 750-800 ºC (Fig. 14(a)). In Chapter 4, this is defined as GB solidus temperature.

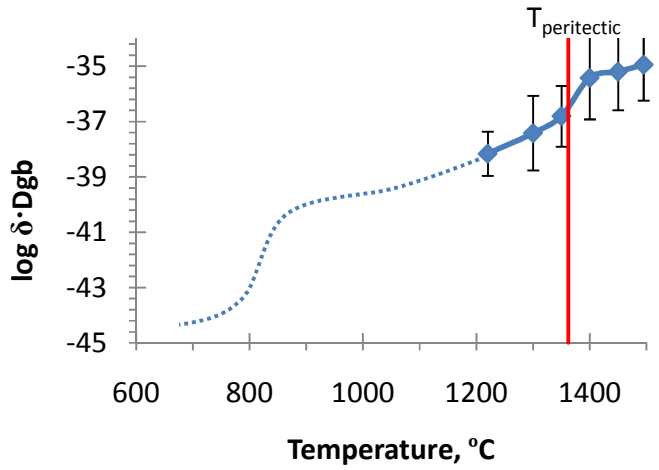


(a)

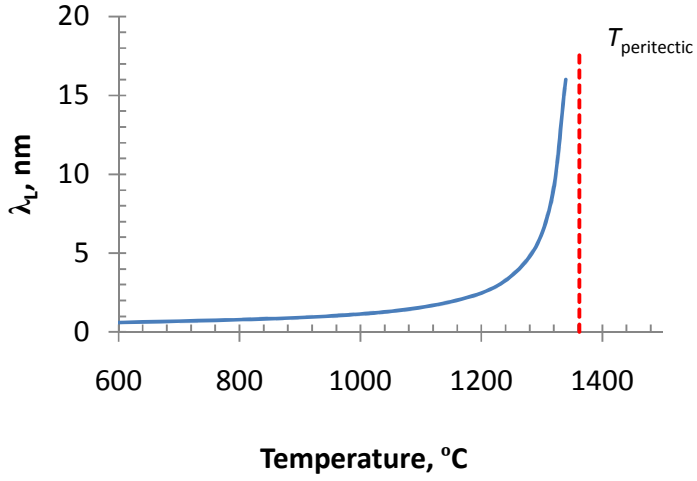


(b)

Figure 7.14 (a) Plot of GB diffusivities *vs* different sintering temperatures for the 2 at. % Ni doped Mo in the sub-peritectic and liquid two-phase regimes; (b) plot of $\lambda_L$ vs temperatures in the sub-peritectic two phase regime, it approaches infinity as Ni atomic percent close to the bulk solidus composition. This sample point is always in two-phase regime ($T < T_{peritect}$ in BCC-δ regime, $T > T_{peritectic}$ in BCC-liquid regime).

In subsolidus single-phase regime, the trend is shown as Fig. 7.15:

- For pure Mo (Fig. 7.15 (a)), GB diffusivity increases with temperature, which is consistent with Arrhenius equation ($D = D_0 \cdot e^{-\frac{G}{RT}}$).
- For Mo samples doped with 0.25 at % Ni (Fig. 7.15(b)), GB diffusivity shows an almost flat pattern.
- However, for Mo samples doped with 0.5 at % Ni (Fig. 7.15 (c)) and 1.0 at. % Ni (Fig. 21(d)), GB diffusivities show a trend of decreasing with temperature (except 1220 ºC).

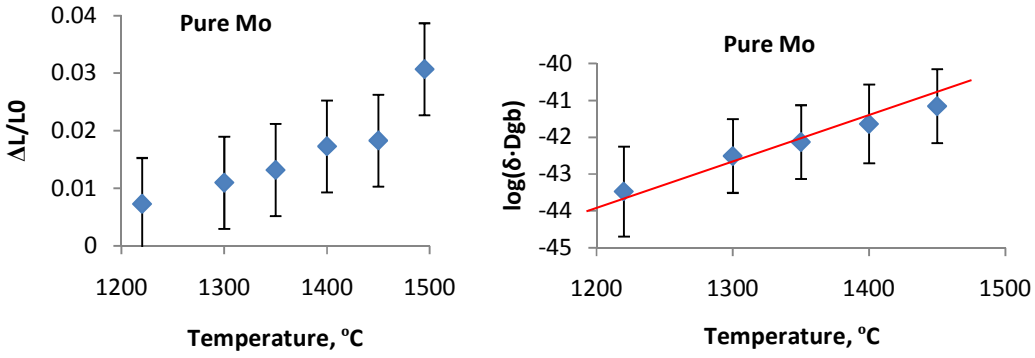


(a)

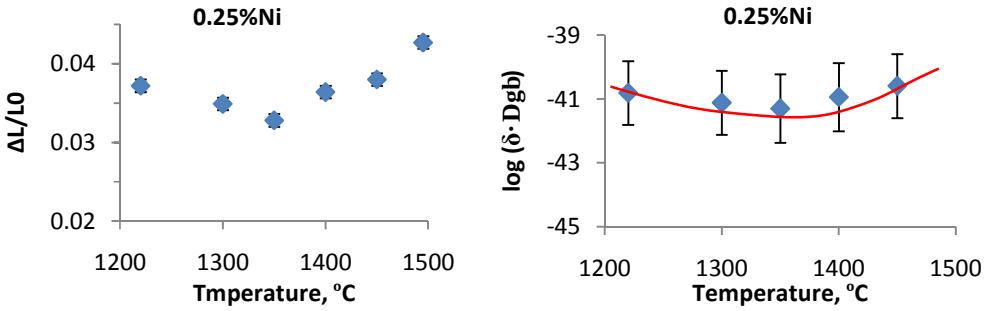


(b)

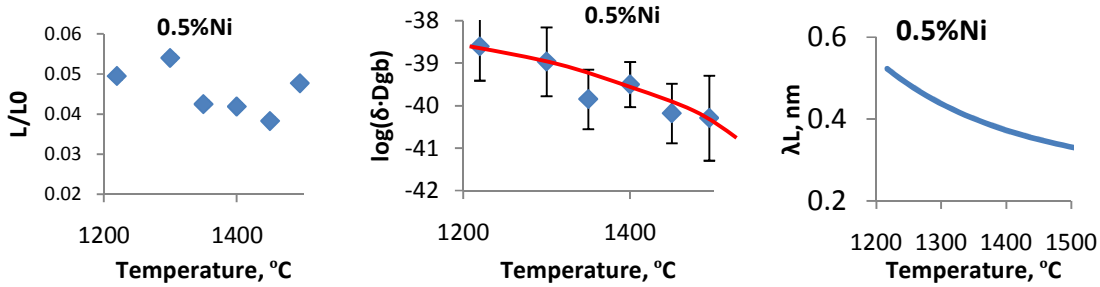


(c)

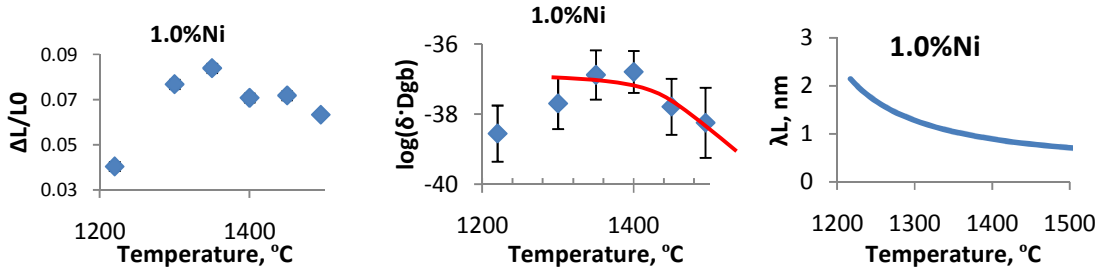


(d)

Figure 7.15 The temperature dependence of linear shrinkage (after 2 hours sintering) and GB diffusivities in subsolidus single-phase regime for pure Mo (a), Mo + 0.25 at. % Ni (b), Mo + 0.5 at. % Ni (c) and Mo + 1.00 at. %Ni (d). The plots of $\lambda_L$ vs. temperatures in subsolidus single-phase regime are also list on the side as comparison for 0.5 at. % Ni (c) and Mo + 1.00 at. % Ni (d).

Although *T*-dependence of Mo samples doped with 0.5 and 1.0 atomic % Ni seems to be in conflict with the Arrhenius equation, it can be well explained from the GB phase diagram point of view. As shown in $\lambda_L$-plot on the side in Fig. 7.15 (c) and (d), with increasing temperature, film thickness ($\lambda_L$) decreased. Moreover, as shown in Fig. 7.16, a Ni-Mo GB phase diagram, when temperature increases, the corresponding IGF decreases in film thickness. This trend can be observed especially clearly when the composition line of 0.5 intersects with isoline of 0.5 nm $\lambda_L$. Thinner film leads to lower GB diffusivity. There is no IGF in pure Mo. So this interesting trend is not found in the sintering of pure Mo, whereby only Arrhenius equation dominated.

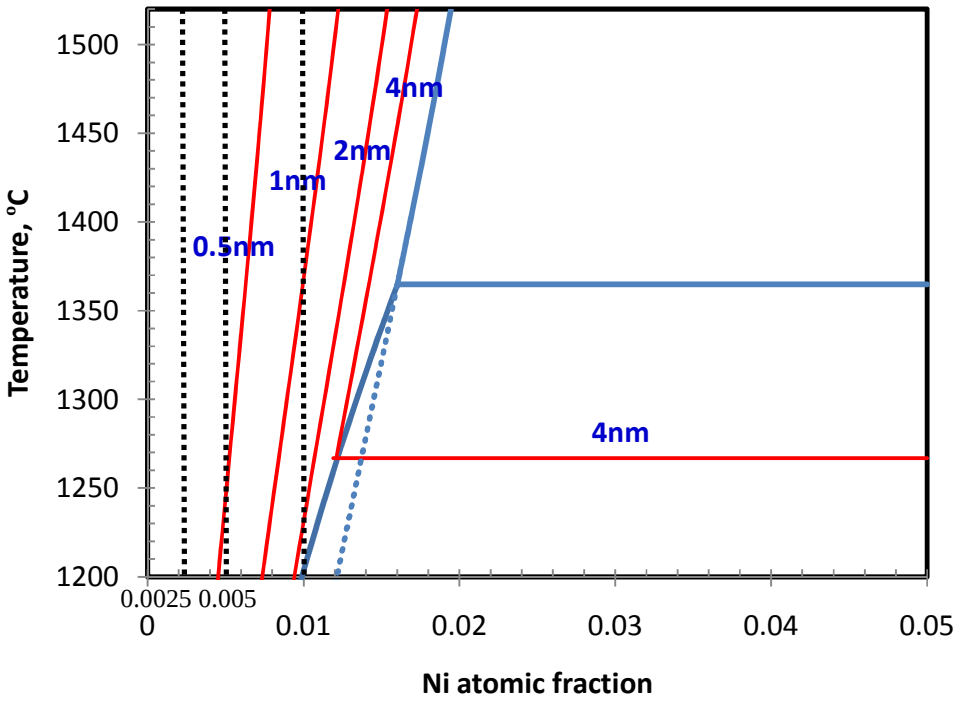


Figure 7.16 GB phase diagram of Ni-Mo binary system and correlation with sintering. The three vertical dashed lines represent three different Ni atomic fractions respectively from left to right: 0.0025, 0.005 and 0.01 (equivalent to 0.25, 0.5 and 1.0 at. %).

## 7.7 Correlation between GB Diagram and GB Diffusivities

In Fig. 7.17, which is an enlarged region of Ni-Mo GB diagram, the upper-left corner was the regime whereby bulk diffusion took the control of sintering; the rest of single-phase regime indicated GB diffusion controlled sintering.

There are several key points worthy of being noted:

- A grey thick line, which corresponded to the range of compositions where GB diffusivity jumps happened in various sintering temperatures, was drawn in

single-phase regime. It is close and parallel with isoline of computed $\lambda_L$ = 0.5 nm. The right side of this line showed the existence of nanoscale quasi-liquid IGF and enhanced sintering; otherwise, the left side of it exhibited much less improvement of sintering.

- In the sub-peritectic two-phase regime, IGFs exhibited constant films at a certain temperature. Comparably in sintering experiment, the GB diffusivities almost leveled off in this sub-peritectic regime (1220 ºC, 1300 ºC and 1350 ºC in Fig. 7.16-18).
- At temperature above $T_{peritectic}$, IGFs show complete wetting and macroscopic film when Ni atomic fractions enter into liquid-phase regime. Accordingly, GB diffusivity has another jump.

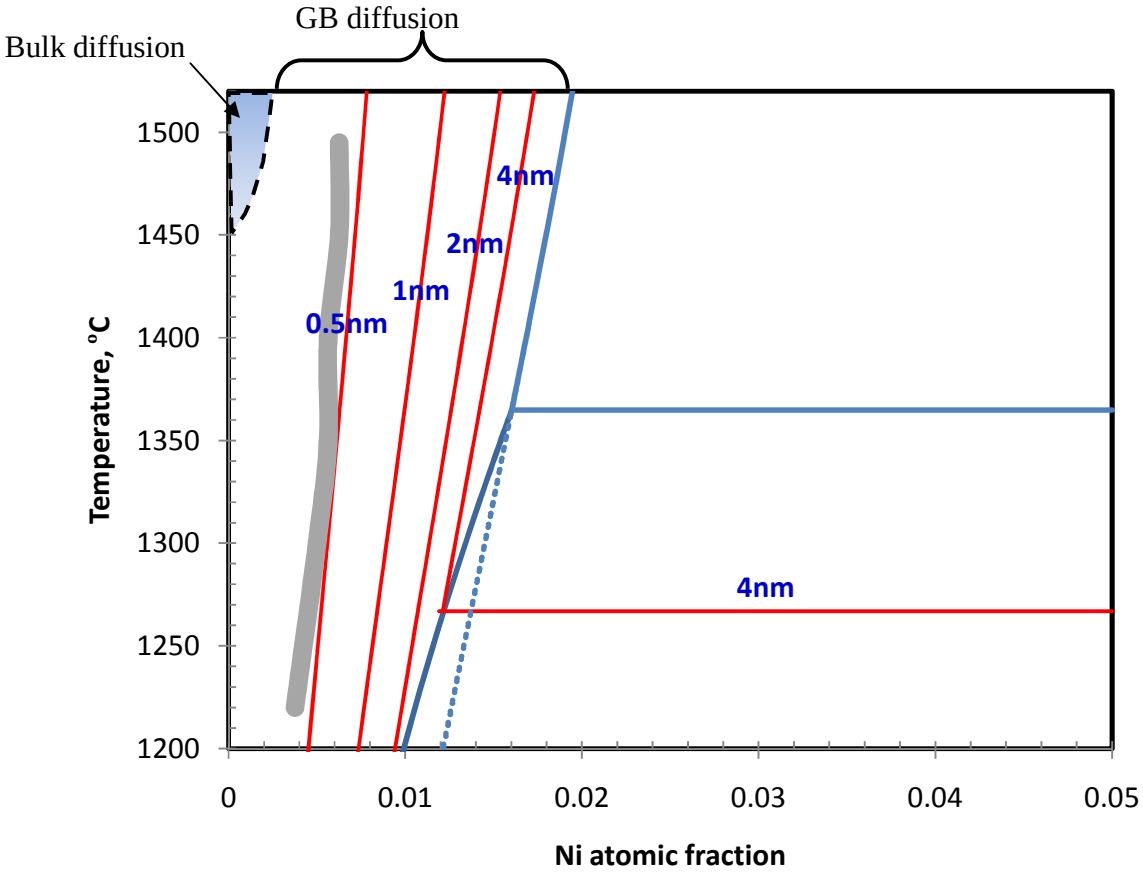


Figure 7.17 Enlarged GB phase diagram of Ni-Mo binary system labeled with correlation with activated sintering.

## 7.8 Summary and Discussion

This correlation between GB diffusivity and calculated $\lambda_L$ clearly revealed that the promoted sintering was attributed to the enhanced GB transport due to the quasi-liquid

IGF. This observation reconfirmed the previously proposed mechanism of subsolidus activated sintering for $Bi_2O_3$-ZnO [11] and Ni-W [12] systems.

In single-phase regime, the dependence of GB diffusivity on Ni amount and temperature are fairly consistent with the dependence of model-predicted IGF on Ni amount and temperature. Especially, the abnormal decrease of GB diffusivity with increasing temperature can be well-explained using GB phase diagram. Therefore, the regular rule that increasing temperature can boost sintering is not always true.

In sub-peritectic two-phase regime, quasi-liquid IGF can persist well below peritectic temperature whereby activated sintering can possibly happen (up to 1200 ºC has been demonstrate by sintering experiments); consequently, bulk phase diagram is not adequate to guide the heat treatment recipe at this point. In addition, film thickness is independent of Ni atomic fraction in sub-peritectic two-phase regime. It is consistent with flat GB diffusivity in this regime.

This GB phase diagram which had been demonstrated can serve as a new tool to predict GB related phenomena, *e.g.* grain growth, GB embrittlement, corrosion and oxidation resistance and creeping, as only bulk phase diagram is no longer adequate.

## 7.9 Appendix – Raw Densification Data

Table 7.5a Measured densification data of specimens of various Ni contents that were isothermally sintered at 1495 ºC.

| Linear shrinkage, $\Delta L/L_0$ | | | | | | |
|---|---|---|---|---|---|---|
| Time, mins | 0 | 10 | 30 | 60 | 120 | 240 |
| Pure Mo, ΔL/L0 | 0.0031 | 0.0105 | 0.0204 | 0.0307 | 0.0393 | 0.0464 |
| 0.25%Ni, ΔL/L0 | 0.0126 | 0.0204 | 0.0235 | 0.0272 | 0.0314 | 0.0377 |
| 0.50%Ni, ΔL/L0 | 0.0000 | 0.0199 | 0.0288 | 0.0320 | 0.0377 | 0.0477 |
| 0.75%Ni, ΔL/L0 | 0.0047 | 0.0372 | 0.0419 | 0.0435 | 0.0451 | 0.0514 |
| 1.00%Ni, ΔL/L0 | 0.0078 | 0.0351 | 0.0413 | 0.0466 | 0.0529 | 0.0633 |
| 1.50%Ni, ΔL/L0 | 0.0031 | 0.0414 | 0.0503 | 0.0582 | 0.0687 | 0.0786 |
| 1.75%Ni, ΔL/L0 | 0.0031 | 0.0713 | 0.0781 | 0.0891 | 0.0959 | 0.1101 |
| 2.00%Ni, ΔL/L0 | 0.0047 | | 0.0801 | 0.0926 | 0.1091 | 0.1179 |
| 4.00%Ni, ΔL/L0 | 0.0031 | | 0.1148 | 0.1234 | 0.1344 | 0.1384 |
| Relative density, $\rho$ | | | | | | |
| Pure Mo, $\rho$ | 0.620 | 0.631 | 0.643 | 0.649 | 0.660 | 0.666 |
| 0.25%Ni, $\rho$ | 0.616 | 0.629 | 0.634 | 0.641 | 0.649 | 0.661 |
| 0.50%Ni, $\rho$ | 0.588 | 0.621 | 0.638 | 0.645 | 0.656 | 0.674 |
| 0.75%Ni, $\rho$ | 0.615 | 0.673 | 0.682 | 0.685 | 0.688 | 0.702 |
| 1.00%Ni, $\rho$ | 0.613 | 0.661 | 0.674 | 0.684 | 0.696 | 0.717 |
| 1.50%Ni, $\rho$ | 0.599 | 0.667 | 0.683 | 0.696 | 0.716 | 0.738 |
| 1.75%Ni, $\rho$ | 0.605 | 0.727 | 0.747 | 0.772 | 0.789 | 0.819 |
| 2.00%Ni, $\rho$ | 0.586 | | 0.727 | 0.751 | 0.792 | 0.816 |
| 4.00%Ni, $\rho$ | 0.581 | | 0.803 | 0.839 | 0.862 | 0.874 |

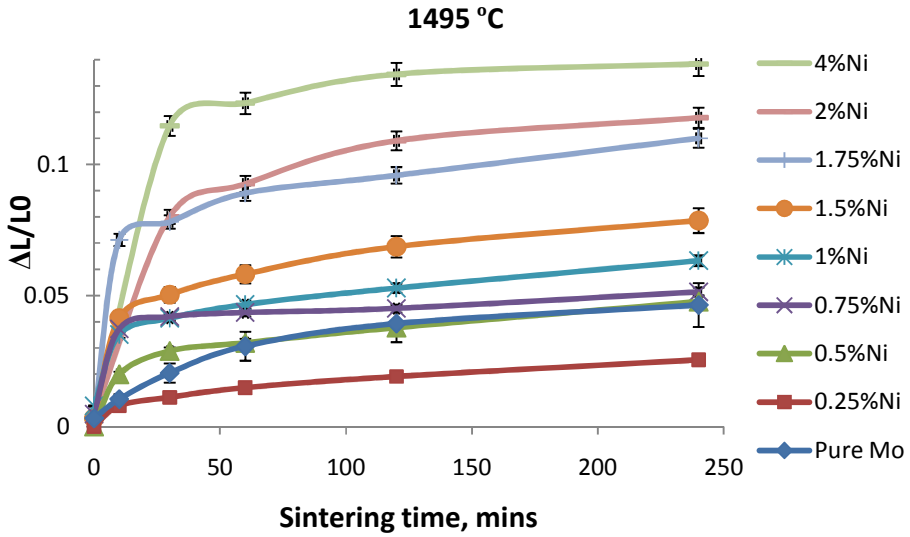


(a)

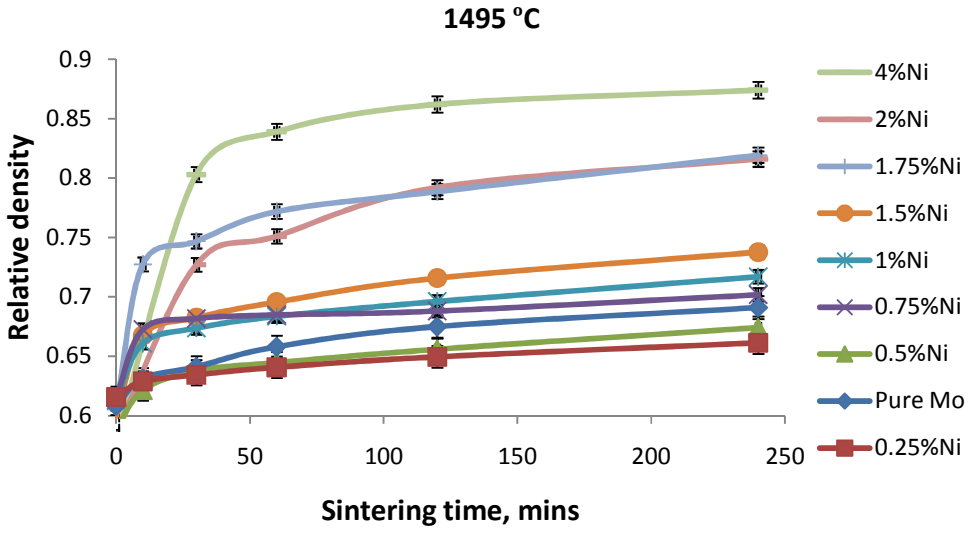


(b)

Figure 7.17 Densification rate data for specimens isothermally sintered at 1495 °C: (a) linear shrinkage and (b) relative density vs. sintering time.

Table 7.5b Measured densification data of specimens of various Ni contents that were isothermally sintered at 1450 ºC.

| Linear shrinkage, $\Delta L/L_0$ | | | | | | |
|---|---|---|---|---|---|---|
| Time, mins | 0 | 10 | 30 | 60 | 120 | 240 |
| Pure Mo | 0.0031 | 0.0110 | 0.0142 | 0.0183 | 0.0236 | 0.0283 |
| 0.25%Ni | 0.0094 | 0.0162 | 0.0189 | 0.0236 | 0.0273 | 0.0330 |
| 0.375%Ni | 0.0031 | 0.0162 | 0.0194 | 0.0236 | 0.0288 | 0.0367 |
| 0.50%Ni | 0.0094 | 0.0215 | 0.0241 | 0.0283 | 0.0325 | 0.0383 |
| 0.75%Ni | 0.0047 | 0.0288 | 0.0325 | 0.0425 | 0.0461 | 0.0571 |
| 1.00%Ni | 0.0047 | 0.0356 | 0.0388 | 0.0477 | 0.0519 | 0.0718 |
| 1.50%Ni | 0.0031 | 0.0540 | 0.0660 | 0.0776 | 0.0833 | 0.0894 |
| 1.75%Ni | 0.0031 | 0.0692 | 0.0854 | 0.1006 | 0.1127 | 0.1242 |
| 2.00%Ni | 0.0031 | 0.0655 | 0.0833 | 0.0980 | 0.1111 | 0.1237 |
| 4.00%Ni | 0.0047 | 0.0949 | 0.1127 | 0.1263 | 0.1357 | 0.1426 |
| Relative density, $\rho$ | | | | | | |
| Pure Mo | 0.616 | 0.630 | 0.636 | 0.643 | 0.653 | 0.661 |
| 0.25%Ni | 0.613 | 0.622 | 0.627 | 0.634 | 0.642 | 0.652 |
| 0.375%Ni | 0.602 | 0.624 | 0.629 | 0.636 | 0.646 | 0.660 |
| 0.50%Ni | 0.625 | 0.642 | 0.645 | 0.652 | 0.660 | 0.672 |
| 0.75%Ni | 0.609 | 0.650 | 0.657 | 0.673 | 0.683 | 0.706 |
| 1.00%Ni | 0.623 | 0.664 | 0.668 | 0.687 | 0.694 | 0.736 |
| 1.50%Ni | 0.601 | 0.698 | 0.720 | 0.746 | 0.757 | 0.777 |
| 1.75%Ni | 0.607 | 0.732 | 0.767 | 0.803 | 0.834 | 0.868 |
| 2.00%Ni | 0.605 | 0.724 | 0.762 | 0.798 | 0.830 | 0.865 |
| 4.00%Ni | 0.606 | 0.782 | 0.828 | 0.866 | 0.892 | 0.911 |

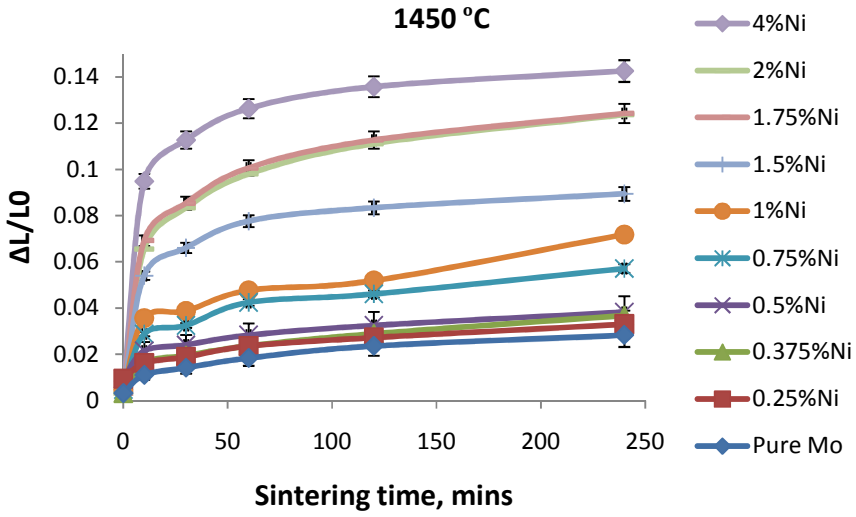


(a)

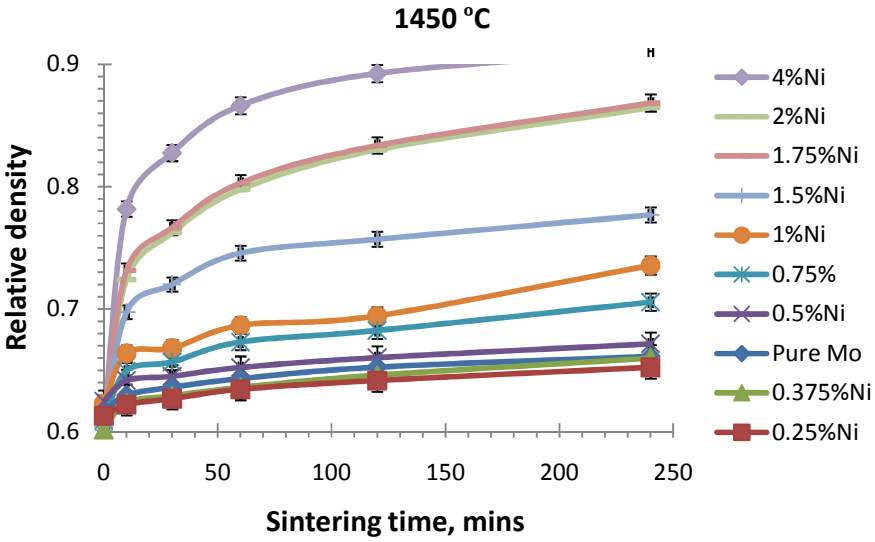


(b)

Figure 7.18 Densification rate data for specimens isothermally sintered at 1450 ºC: (a) linear shrinkage and (b) relative density vs. sintering time.

Table 7.5c Measured densification data of specimens of various Ni contents that were isothermally sintered at 1400 ºC.

| Linear shrinkage, $\Delta L/L_0$ | | | | | | | | |
|---|---|---|---|---|---|---|---|---|
| Time, mins | 0 | 10 | 30 | 60 | 120 | 240 | 480 | 960 |
| Pure Mo | 0.0016 | 0.0094 | 0.0142 | 0.0173 | 0.0200 | 0.0241 | 0.0294 | 0.0346 |
| 0.25%Ni | 0.0079 | 0.0157 | 0.0189 | 0.0236 | 0.0272 | 0.0314 | 0.0377 | 0.0451 |
| 0.375%Ni | 0.0031 | 0.0157 | 0.0200 | 0.0252 | 0.0303 | 0.0357 | 0.0404 | 0.0477 |
| 0.50%Ni | 0.0079 | 0.0220 | 0.0241 | 0.0309 | 0.0362 | 0.0419 | 0.0482 | 0.0556 |
| 0.75%Ni | 0.0047 | 0.0299 | 0.0330 | 0.0362 | 0.0430 | 0.0519 | 0.0618 | 0.0781 |
| 1.00%Ni | 0.0031 | 0.0383 | 0.0461 | 0.0608 | 0.0645 | 0.0708 | --------- | -------- |
| 1.50%Ni | 0.0031 | 0.0550 | 0.0671 | 0.0833 | 0.0980 | 0.1132 | --------- | -------- |
| 1.75%Ni | 0.0031 | 0.0671 | 0.0875 | 0.1001 | 0.1132 | 0.1268 | --------- | -------- |
| 2.00%Ni | 0.0031 | 0.0629 | 0.0797 | 0.0954 | 0.1101 | 0.1242 | --------- | --------- |
| 4.00%Ni | 0.0031 | 0.0928 | 0.1174 | 0.1316 | 0.1405 | 0.1520 | --------- | --------- |
| Relative density, $\rho$ | | | | | | | | |
| Pure Mo | 0.618 | 0.632 | 0.641 | 0.647 | 0.651 | 0.659 | 0.668 | 0.679 |
| 0.25%Ni | 0.619 | 0.630 | 0.635 | 0.644 | 0.650 | 0.657 | 0.670 | 0.684 |
| 0.375%Ni | 0.607 | 0.628 | 0.637 | 0.646 | 0.656 | 0.665 | 0.675 | 0.689 |
| 0.50%Ni | 0.624 | 0.645 | 0.648 | 0.659 | 0.669 | 0.680 | 0.693 | 0.709 |
| 0.75%Ni | 0.623 | 0.656 | 0.661 | 0.667 | 0.680 | 0.699 | 0.720 | 0.754 |
| 1.00%Ni | 0.621 | 0.671 | 0.682 | 0.712 | 0.721 | 0.733 | --------- | --------- |
| 1.50%Ni | 0.602 | 0.699 | 0.723 | 0.759 | 0.794 | 0.834 | -------- | --------- |
| 1.75%Ni | 0.601 | 0.723 | 0.765 | 0.799 | 0.830 | 0.869 | --------- | --------- |
| 2.00%Ni | 0.606 | 0.718 | 0.754 | 0.790 | 0.827 | 0.866 | --------- | --------- |
| 4.00%Ni | 0.577 | 0.743 | 0.804 | 0.841 | 0.869 | 0.904 | --------- | --------- |

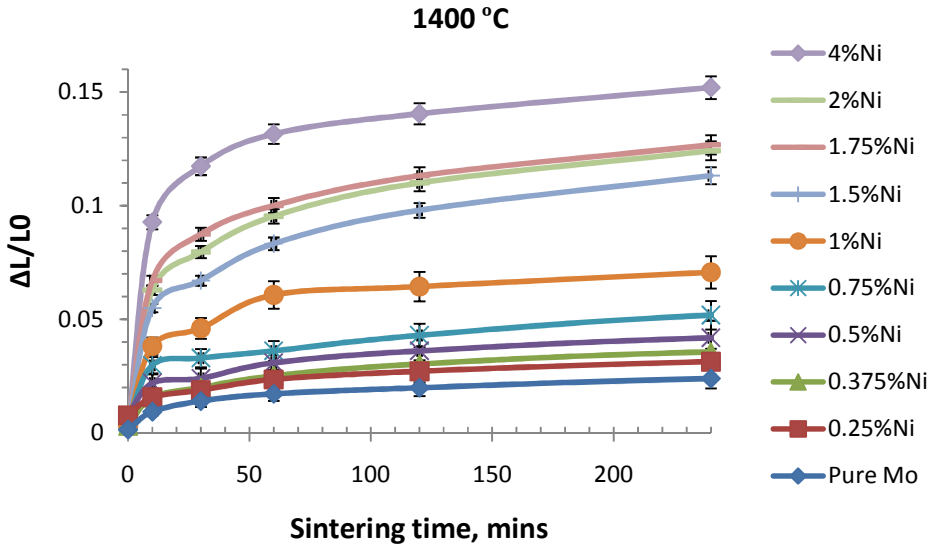


(a)

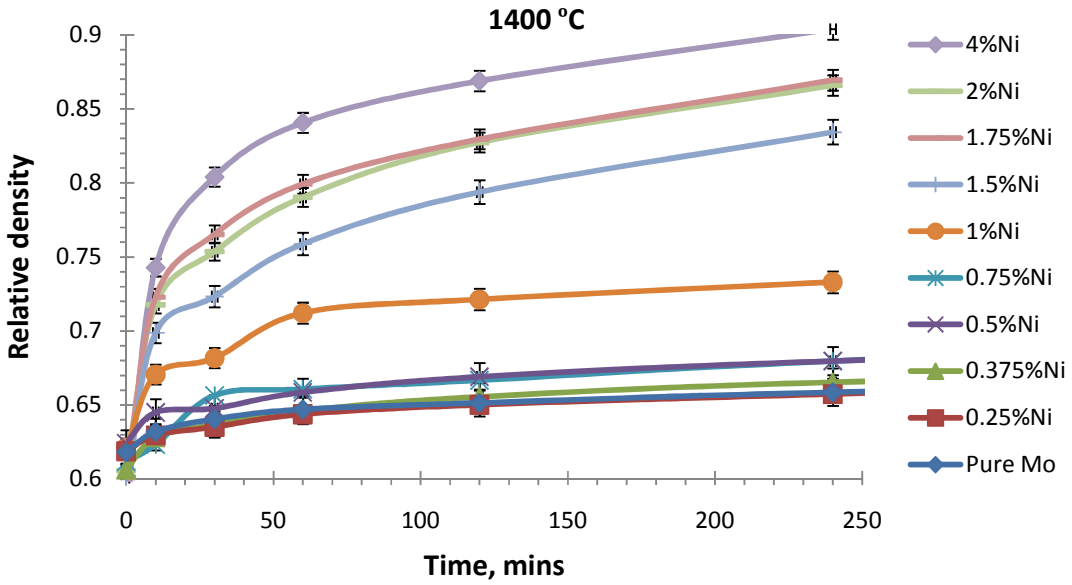


(b)

Figure 7.19 Densification rate data for specimens isothermally sintered at 1400 ºC: (a) linear shrinkage and (b) relative density vs. sintering time.

Table 7.5d Measured densification data of specimens of various Ni contents that were isothermally sintered at 1350 ºC.

| Linear shrinkage, $\Delta L/L_0$ | | | | | | | |
|---|---|---|---|---|---|---|---|
| Time, mins | 0 | 20 | 60 | 120 | 240 | 480 | 940 |
| Pure Mo | 0.0047 | 0.0083 | 0.0132 | 0.0168 | 0.0220 | 0.0247 | 0.0288 |
| 0.25%Ni | 0.0110 | 0.0162 | 0.0199 | 0.0225 | 0.0278 | 0.0335 | 0.0383 |
| 0.375%Ni | 0.0031 | 0.0157 | 0.0199 | 0.0241 | 0.0320 | 0.0404 | 0.0451 |
| 0.50%Ni | 0.0079 | 0.0220 | 0.0278 | 0.0341 | 0.0425 | 0.0503 | 0.0540 |
| 0.75%Ni | 0.0063 | 0.0262 | 0.0419 | 0.0618 | 0.0734 | 0.0802 | --- |
| 1.00%Ni | 0.0031 | 0.0294 | 0.0440 | 0.0681 | 0.0839 | 0.0959 | --- |
| 1.25%Ni | 0.0063 | 0.0288 | 0.0451 | 0.0723 | 0.0922 | 0.1085 | --- |
| 2.00%Ni | 0.0031 | 0.0330 | 0.0482 | 0.0749 | 0.0970 | 0.1116 | --- |
| 4.00%Ni | 0.0031 | 0.0346 | 0.0561 | 0.0828 | 0.1053 | 0.1216 | --- |
| Relative density, $\rho$ | | | | | | | |
| Pure Mo | 0.611 | 0.617 | 0.625 | 0.632 | 0.641 | 0.647 | 0.655 |
| 0.25%Ni | 0.627 | 0.633 | 0.640 | 0.645 | 0.655 | 0.666 | 0.675 |
| 0.375%Ni | 0.611 | 0.633 | 0.641 | 0.649 | 0.664 | 0.680 | 0.690 |
| 0.50%Ni | 0.631 | 0.650 | 0.658 | 0.671 | 0.687 | 0.702 | 0.710 |
| 0.75%Ni | 0.612 | 0.646 | 0.677 | 0.717 | 0.743 | 0.758 | --- |
| 1.00%Ni | 0.603 | 0.650 | 0.678 | 0.729 | 0.766 | 0.792 | --- |
| 1.25%Ni | 0.612 | 0.651 | 0.683 | 0.739 | 0.787 | 0.826 | --- |
| 2.00%Ni | 0.612 | 0.666 | 0.694 | 0.753 | 0.804 | 0.842 | --- |
| 4.00%Ni | 0.603 | 0.661 | 0.702 | 0.761 | 0.815 | 0.854 | --- |

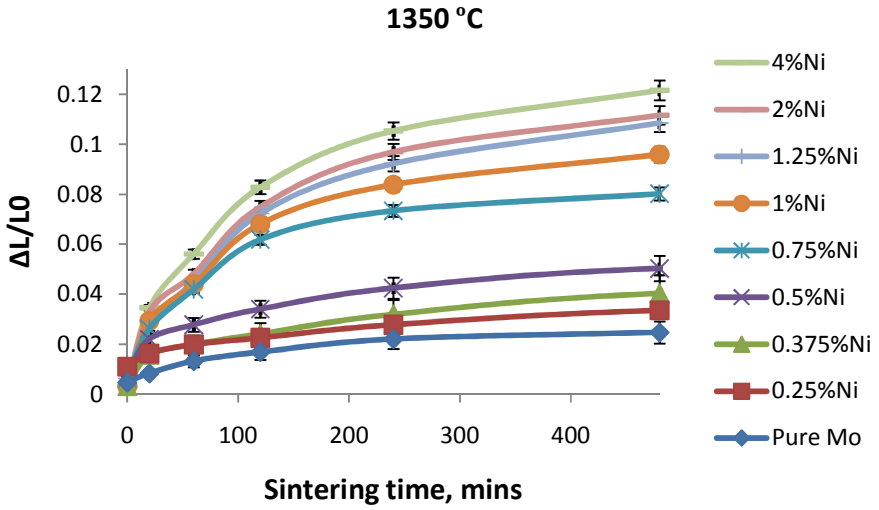


(a)

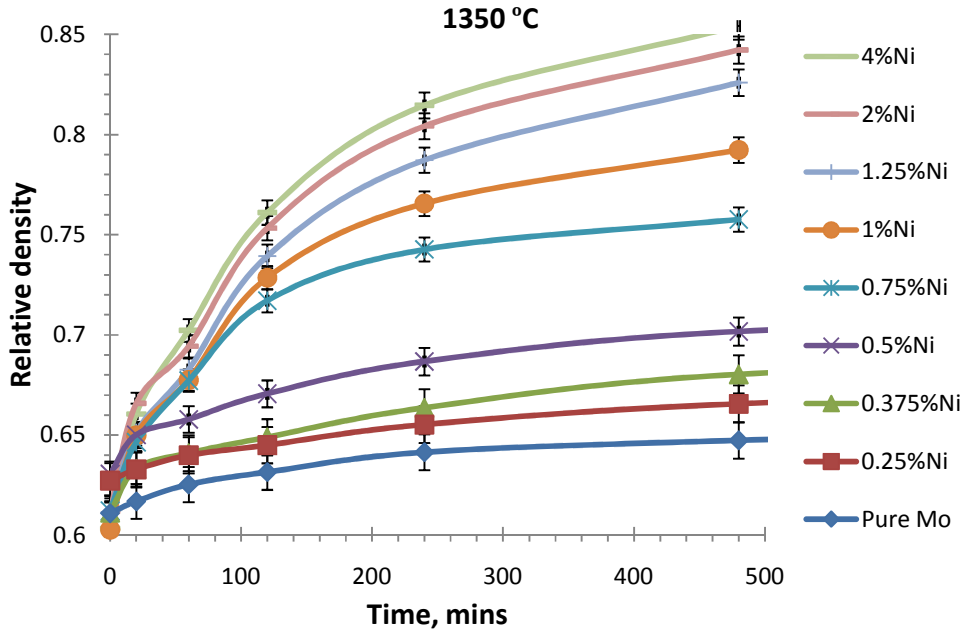


(b)

Figure 7.20 Densification rate data for specimens isothermally sintered at 1350 °C: (a) linear shrinkage and (b) relative density vs. sintering time.

Table 7.5e Measured densification data of specimens of various Ni contents that were isothermally sintered at 1300 ºC.

| Linear shrinkage, $\Delta L/L_0$ | | | | | | | |
|---|---|---|---|---|---|---|---|
| Time, mins | 0 | 20 | 60 | 120 | 240 | 480 | 960 |
| Pure Mo | 0.0031 | 0.0094 | 0.0110 | 0.0142 | 0.0173 | 0.0236 | 0.0278 |
| 0.25%Ni | 0.0110 | 0.0178 | 0.0220 | 0.0252 | 0.0299 | 0.0362 | 0.0419 |
| 0.50%Ni | 0.0094 | 0.0215 | 0.0341 | 0.0425 | 0.0540 | 0.0660 | 0.0729 |
| 0.75%Ni | 0.0047 | 0.0225 | 0.0393 | 0.0550 | 0.0760 | 0.0922 | --------- |
| 1.75%Ni | 0.0031 | 0.0262 | 0.0414 | 0.0561 | 0.0791 | 0.0975 | --------- |
| 4.00%Ni | 0.0047 | 0.0262 | 0.0425 | 0.0597 | 0.0828 | 0.1038 | --------- |
| Relative density, $\rho$ | | | | | | | |
| Pure Mo | 0.623 | 0.634 | 0.637 | 0.643 | 0.650 | 0.660 | 0.669 |
| 0.25%Ni | 0.619 | 0.631 | 0.637 | 0.643 | 0.652 | 0.664 | 0.674 |
| 0.50%Ni | 0.619 | 0.640 | 0.656 | 0.673 | 0.696 | 0.708 | 0.717 |
| 0.75%Ni | 0.606 | 0.637 | 0.668 | 0.699 | 0.743 | 0.782 | --------- |
| 1.75%Ni | 0.601 | 0.642 | 0.672 | 0.700 | 0.749 | 0.793 | --------- |
| 4.00%Ni | 0.584 | 0.620 | 0.651 | 0.684 | 0.733 | 0.779 | --------- |

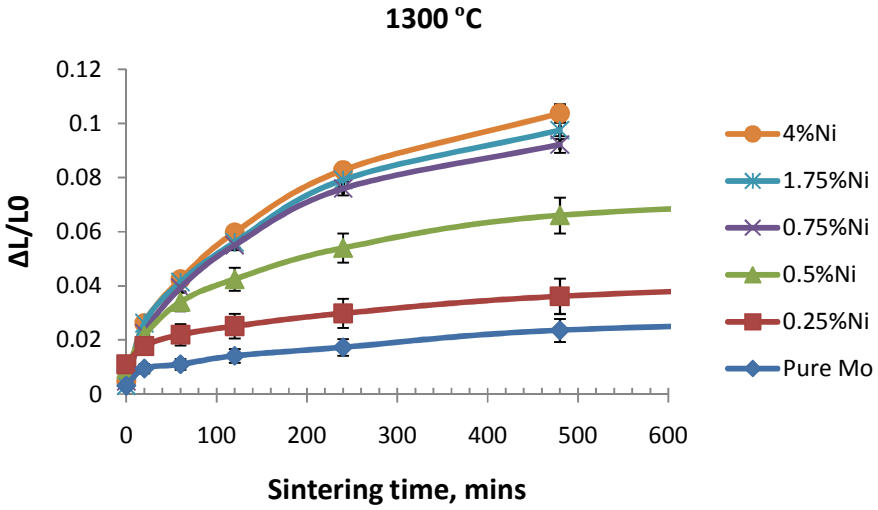


(a)

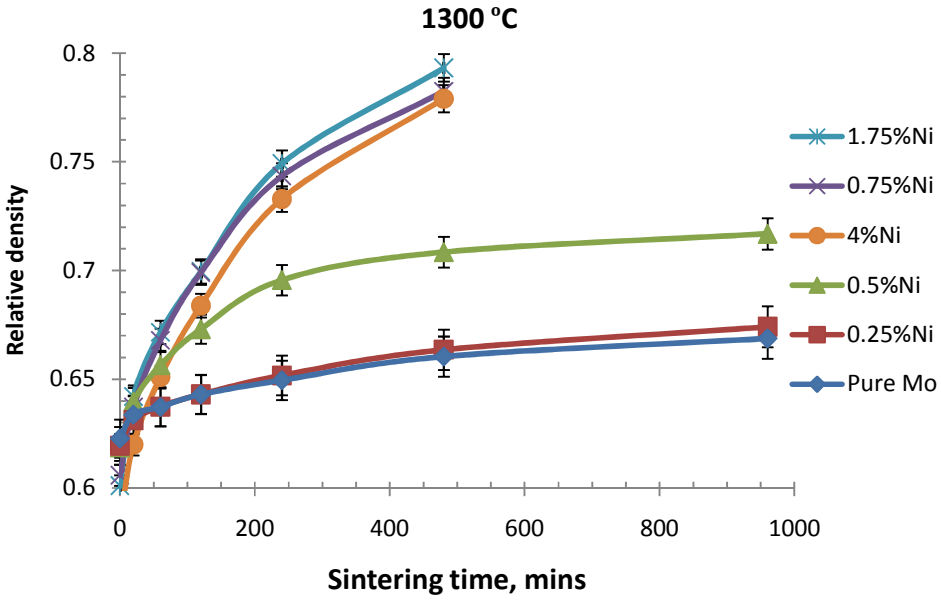


(b)

Figure 7.21 Densification rate data for specimens isothermally sintered at 1300 °C: (a) linear shrinkage and (b) relative density vs. sintering time.

Table 7.5f Measured densification data of specimens of various Ni contents that were isothermally sintered at 1220 ºC.

| Linear shrinkage, $\Delta L/L_0$ | | | | | | | |
|---|---|---|---|---|---|---|---|
| Time, mins | 0 | 10 | 40 | 120 | 240 | 480 | 1440 |
| Pure Mo | 0.0063 | 0.0063 | 0.0063 | 0.0102 | 0.0118 | 0.0181 | 0.0236 |
| 0.125%Ni | 0 | 0.0032 | 0.0105 | 0.0142 | 0.0168 | 0.0231 | 0.0262 |
| 0.25%Ni | 0.0094 | 0.0110 | 0.0157 | 0.0275 | 0.0322 | 0.0398 | 0.0487 |
| 0.50%Ni | 0.0094 | 0.0110 | 0.0157 | 0.0346 | 0.0495 | 0.0692 | 0.0891 |
| 1.00%Ni | 0.0063 | 0.0110 | 0.0173 | 0.0354 | 0.0404 | 0.0634 | 0.0818 |
| 2.00%Ni | 0.0047 | 0.0142 | 0.0236 | 0.0401 | 0.0542 | 0.0713 | -------- |
| Relative density, $\rho$ | | | | | | | |
| Pure Mo | 0.614 | 0.614 | 0.615 | 0.623 | 0.626 | 0.637 | 0.647 |
| 0.125%Ni | 0.602 | 0.607 | 0.618 | 0.624 | 0.629 | 0.640 | 0.646 |
| 0.25%Ni | 0.617 | 0.620 | 0.627 | 0.651 | 0.659 | 0.672 | 0.688 |
| 0.50%Ni | 0.623 | 0.625 | 0.633 | 0.669 | 0.698 | 0.739 | 0.783 |
| 1.00%Ni | 0.598 | 0.605 | 0.615 | 0.649 | 0.661 | 0.704 | 0.743 |
| 2.00%Ni | 0.591 | 0.610 | 0.625 | 0.656 | 0.684 | 0.720 | --------- |

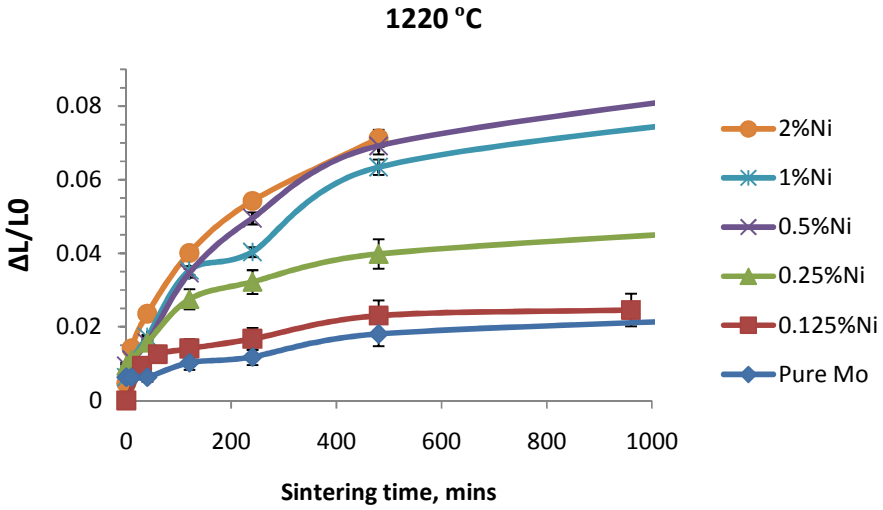


(a)

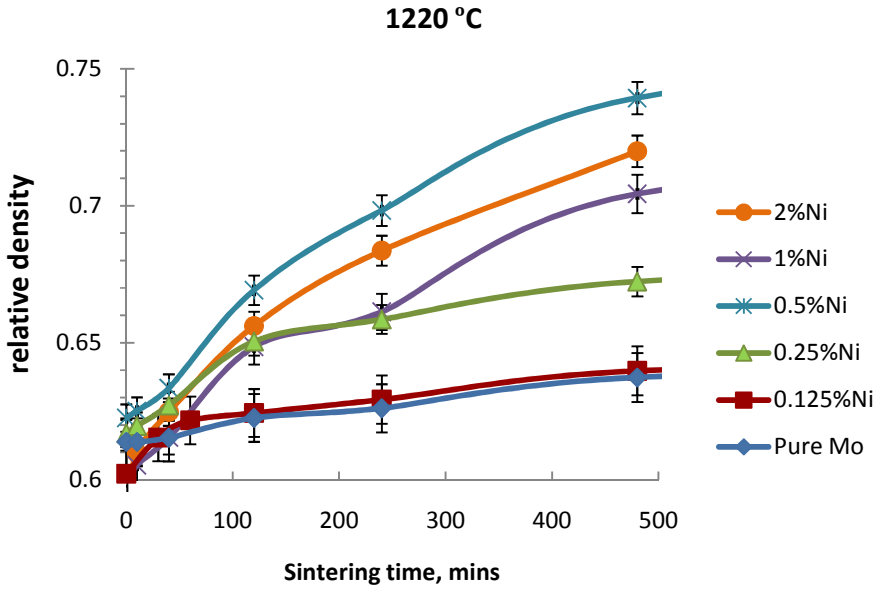


(b)

Figure 7.22 Densification rate data for specimens isothermally sintered at 1220 °C: (a) linear shrinkage and (b) relative density vs. sintering time.

Table 7.5g Measured densification data of specimens of various Ni contents that were isothermally sintered at 1160 ºC.

| Linear shrinkage, $\Delta L/L_0$ | | | | | | | |
|---|---|---|---|---|---|---|---|
| Time, mins | 0 | 30 | 60 | 150 | 290 | 600 | 1080 |
| 2.00%Ni | 0.0047 | 0.0126 | 0.0168 | 0.0194 | 0.0304 | 0.0456 | 0.0577 |
| 4.00%Ni | 0.0047 | 0.0115 | 0.0162 | 0.0194 | 0.0278 | 0.0409 | 0.0535 |
| Relative density, $\rho$ | | | | | | | |
| 2.00%Ni | 0.615 | 0.630 | 0.637 | 0.641 | 0.662 | 0.691 | 0.717 |
| 4.00%Ni | 0.602 | 0.615 | 0.622 | 0.629 | 0.643 | 0.669 | 0.694 |

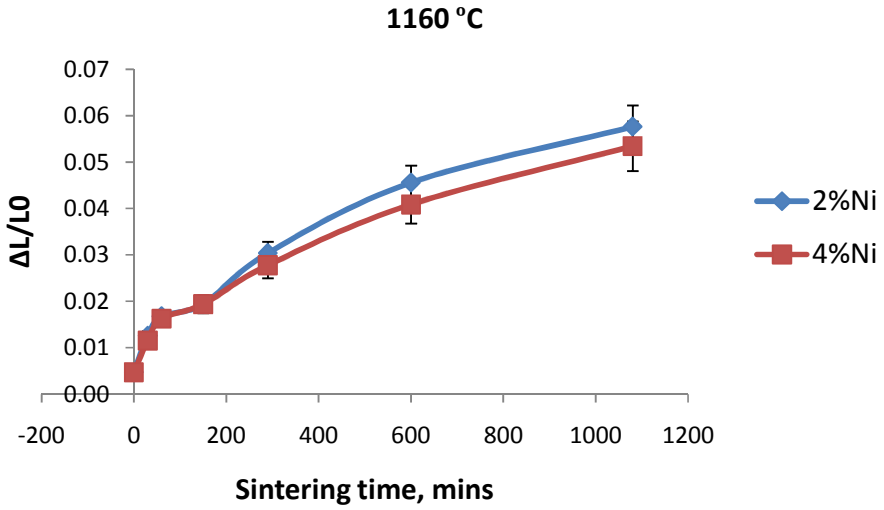


(a)

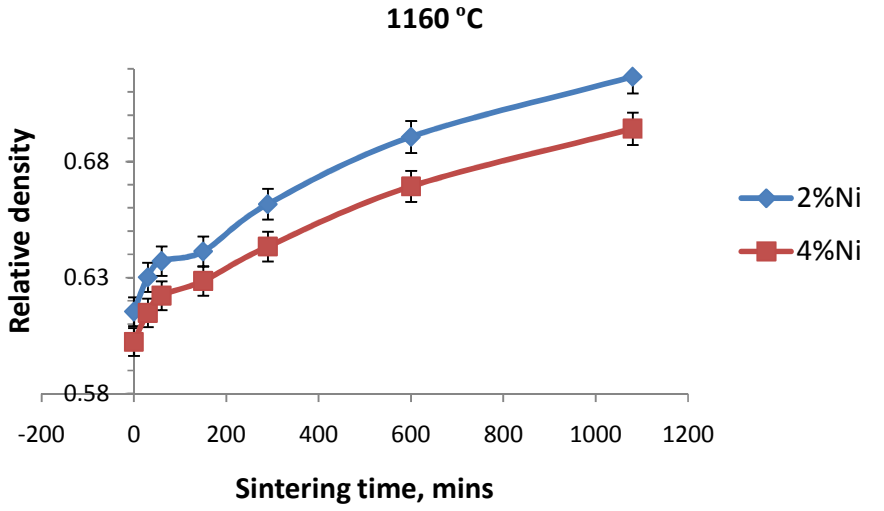


(b)

Figure 7.23 Densification rate data for specimens isothermally sintered at 1160 ºC: (a) linear shrinkage and (b) relative density vs. sintering time.

Table 7.5h Measured densification data of specimens of various Ni contents that were isothermally sintered at 1100ºC.

| Linear shrinkage, $\Delta L/L_0$ | | | | | | | |
|---|---|---|---|---|---|---|---|
| Time, mins | 0 | 60 | 120 | 240 | 480 | 960 | 1620 |
| 2.00%Ni | 0.0047 | 0.0101 | 0.0121 | 0.0220 | 0.0278 | 0.0393 | 0.0478 |
| Relative density, $\rho$ | | | | | | | |
| 2.00%Ni | 0.608 | 0.618 | 0.622 | 0.640 | 0.651 | 0.674 | 0.690 |

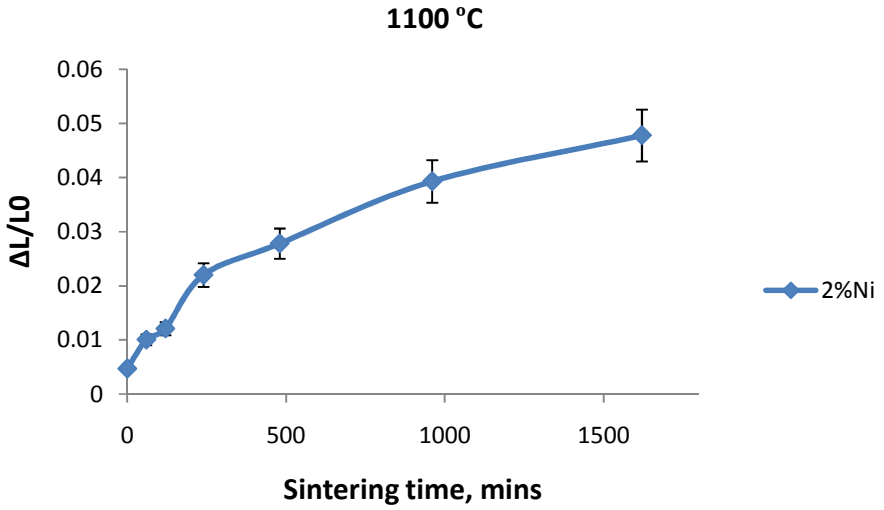


(a)

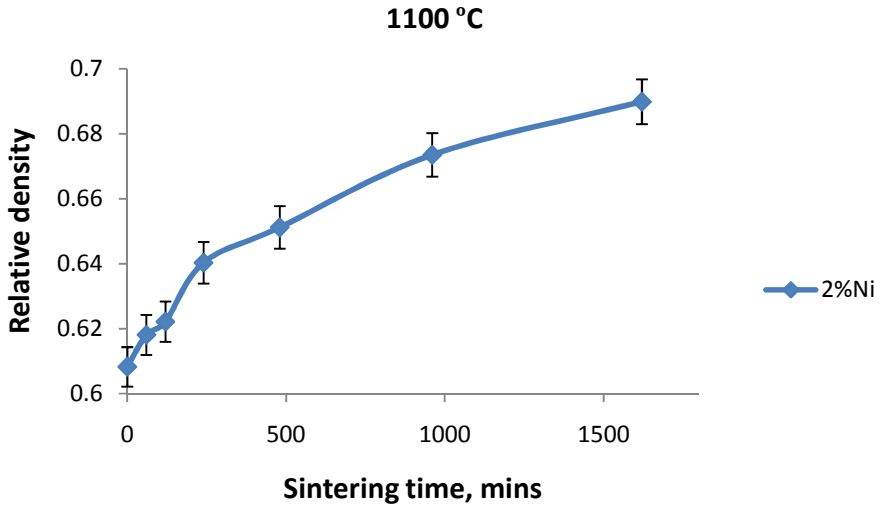


(b)

Figure 7.24 Densification rate data for specimens isothermally sintered at 1100 ºC: (a) linear shrinkage and (b) relative density vs. sintering time.

References

[1] J Luo. Stabilization of Nanoscale Quasi-Liquid Interfacial Films in Inorganic Materials: A Review and Critical Assessment Critical Reviews in Solid State and Material Sciences 32 (2007) 67.

[2] DL Johnson. New method of obtaining volume, grain-boundary, surface diffusion coefficients from sintering data J.Appl.Phys. 40 (1969) 192.

[3] SL Kang. Sintering, Butterworth-Heinemann, 2004.

[4] JT Smith. Diffusion Mechanism for the Nickel-Activated Sintering of Molybdenum J. App. Phys. 36 (1965) 595.

[5] RL Coble. Sintering Crystalline Solids I. Intermediate and Final State Diffusion Models J. App. Phys. 32 (1961) 787.

[6] SJ Park, SH Chung, JM Martin, JL Johnson, RM German. Master sintering curve for densification derived from a constitutive equation with consideration of grain growth: Application to tungsten heavy alloys Metall Mat Trans A Phys Metall Mat Sci 39 (2008) 2941.

[7] WD Kingery, MD Narasimhan. Densification during sintering in presence of liquid phase J.Appl.Phys. 30 (1959) 301.

[8] WD Kingery. Densification during Sintering in the Presence of a Liquid Phase I. Theory Journal of Applied Physics 30 (1959) 301.

[9] RM German. Liquid Phase Sintering, Plenum Press, New York, 1985.

[10] AA Clifford. Multivariate Error Analysis, Applied Science Publishers LTD, London, 1973.

[11] J Luo, H Wang, Y- Chiang. Origin of Solid State Activated Sintering in Bi2O3-Doped ZnO Journal of the American Ceramic Society 82 (1999) 916.

[12] VK Gupta, DH Yoon, HM Meyer III, J Luo. Thin Intergranular Films and Solid-State Activated Sintering in Nickel-Doped Tungsten Acta Materialia 55 (2007) 3131.

# CHAPTER EIGHT

# A PRELIMINARY SINTERING STUDY OF MO-SI-B BASED ALLOYS

## 8.1 Significance of Mo-Si-B

Mo-Si-B based alloys have potential applications in oxidizing atmospheres at > 1200 ºC as turbine-engine materials. Mo-based alloys, such as TZM (Ti and Zr doped Mo) [1,2,3,4,5,6], are superior high-T structural materials in inert atmospheres, but they exhibit poor oxidation resistance in air because $MoO_3$ is evaporative [3,4,5]. Since 1990's, researchers found that Mo-Si-B alloys can exhibit an excellent oxidation-resistance due to the formation of protective boron silicate glass layers. The oxidation resistance stems from the same principle that $MoSi_2$ can be used as oxidization-resistant heating elements for high-T furnaces. In Mo-Si-B alloys, Si is added as a glass former and B as a fluxing agent. As Ni-based superalloy reach their limits, Mo-Si-B based alloys that contain three phases – Mo solid solution ($Mo_{SS}$), $Mo_3Si$ (A15) and $Mo_5SiB_2$ (T2) – are examined as a leading candidate for application at even higher temperatures (potentially 300-400 ºC higher that superalloys can achieved).

## 8.2 Motivation

Mo-Si-B based alloys are selected for this preliminary study, because we perceive opportunities to control their microstructures and resultant properties via utilizing high-T

interfacial thermodynamics (by extending the work that we have done for Mo-Ni to more complex multicomponent alloys). Perepezko *et al*. [7,8,9] pointed out that the absence of the solid-state phase transformation and low diffusivities in this system limit conventional metallurgical methods of the adjusting microstructures. In this regard, this system behaves like a ceramic. Thus, solid-state sintering (powder metallurgy) methods potentially offer a superior way to control microstructures and resultant properties than conventional melt-based methods.

In addition, using Mo-Si-B as another model system, it offers us an opportunity to extend the interfacial thermodynamic model that established for binary Mo-based alloys in Chapter 6 and Chapter 7 to more complex and practically useful multicomponent alloys. Using GB phase diagrams as a guide, we can employ different dopants (generally, Ni, Fe/Co, Ti, Nb) to improve sintering rates (via forming liquid-like GBs) and mitigate GB embrittlement and creep (via utilizing GB transitions). Our goal is to achieve sintered samples with high density, fine microstructure and excellent mechanical properties. This enables us to further extend our interfacial thermodynamic theories, and to explore the potential applications of “GB diagrams” as a new tool for materials science.

## 8.3 Experimental Results

By using the experimental procedures described in Chapter 3, the samples were prepared for density, crystal structure and microstructure analysis. The purpose for this

preliminary study was to explore the effects of sintering temperature, sintering time, dopant and the use of oxygen getter on final density and microstructure.

### 8.3.1 Solid-State Reaction During Sintering

Instead of using pure Si and B as the starting materials, we employed $Si_3N_4$ and BN as the precursor powder to mix with Mo powders following a procedure developed by Middlemas *et al.* [8]. Two kinds of Mo powders with different average particle sizes (1~2 μm and 80 nm, respectively) were tested. In our preliminary study, we focused on one composition, Mo-3Si-B (Mo + 5 at. % Si and 1 % B). Table 8.1 lists the vol% and mol% of three phases in this composition alloy.

Table 8.1 Volume and molar percentage of three phases in Mo-3Si-B alloy from phase diagram.

| Three phases | wt% | vol% | mol% | Density |
|---|---|---|---|---|
| ($Mo_{SS}$) | 63.3 | 56.8 | 56.0 | 10.070 |
| $Mo_3Si$ (A15) | 14.6 | 16 | 15.7 | 8.253 |
| $Mo_5SiB_2$ (T2) | 22.1 | 27.2 | 28.3 | 7.336 |

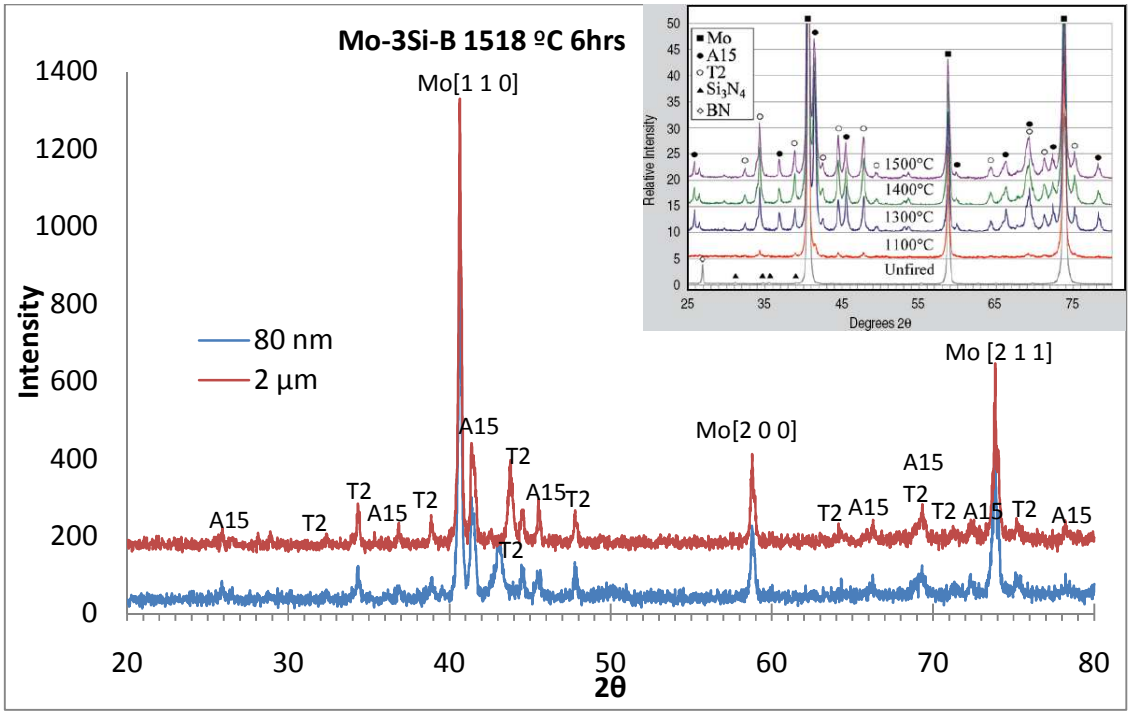


Figure 8.1 XRD results of sintered Mo-Si-B samples. The inset is the XRD of sintered Mo-Si-B from ref. [8]

The XRD results of sintered samples (at 1518 ºC for 6 hours) are shown in Fig. 8.1.

After 6 hours sintering at temperature 1518 ºC, the solid state reactions had been completed, resulting in a $Mo_{SS}$-A15-T2 three-phase microstructure:

$3Mo + 1/3Si_3N_4 \rightarrow Mo_3Si$ (A15 phase) $+ 2/3N_2$ (g)

$5Mo + 1/3Si_3N_4 + 2BN \rightarrow Mo_5SiB_2$ (T2 phase) $+ 5/3N_2$ (g).

These three phases are thermodynamically stable from room temperature to > 2000 °C. Thus, no additional phase transformation is expected when it is sintered at a higher temperature (< 2000 °C) or for longer time. The phase stability is in fact one reason that

this Mo-Si-B is a superior high-T alloy. The effect of temperature and sintering time on the final density and microstructures are examined in next sections.

### 8.3.2 The Effect of Sintering Temperature

In this section, three sintering temperatures, 1518 ºC, 1563 ºC and 1606 ºC, were chosen to study the effect of sintering temperature on densification. The sintering time was fixed to 6 hours. The measured densities are shown in Fig. 8.2.

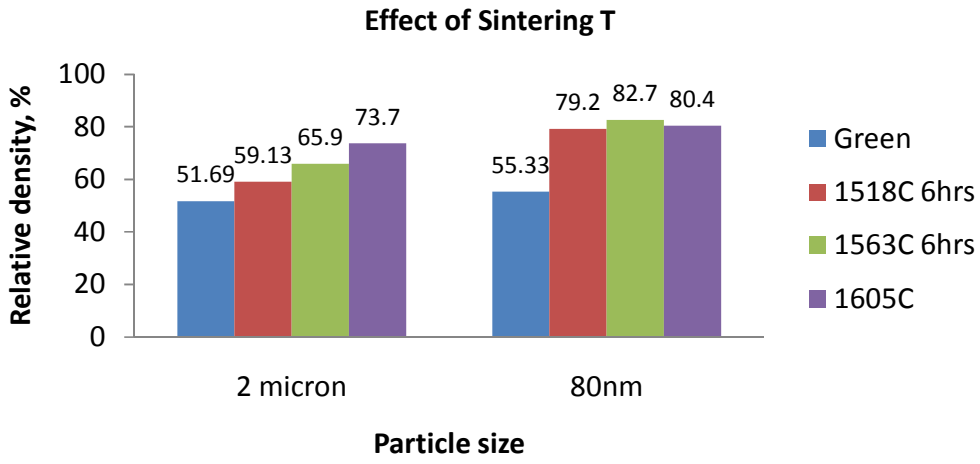


Figure 8.2 The effects of sintering temperatures on the densification.

With the increase of sintering temperature, the final density went up for the samples prepared using 2 μm Mo powder. Interestingly, the density of sample with 80 nm particle size increased less significantly with the sintering temperature, and a

maximum is reached for sintering at 1563 °C. This was, in part, related to agglomeration of nanoparticles, which was discussed in a later section (with a microstructure study).

### 8.3.3 The Effects of Dopants

Two dopants (Ni and Nb) were selected to examine the effects of doping on densification. Fig. 8.3 shows the measured final densities.

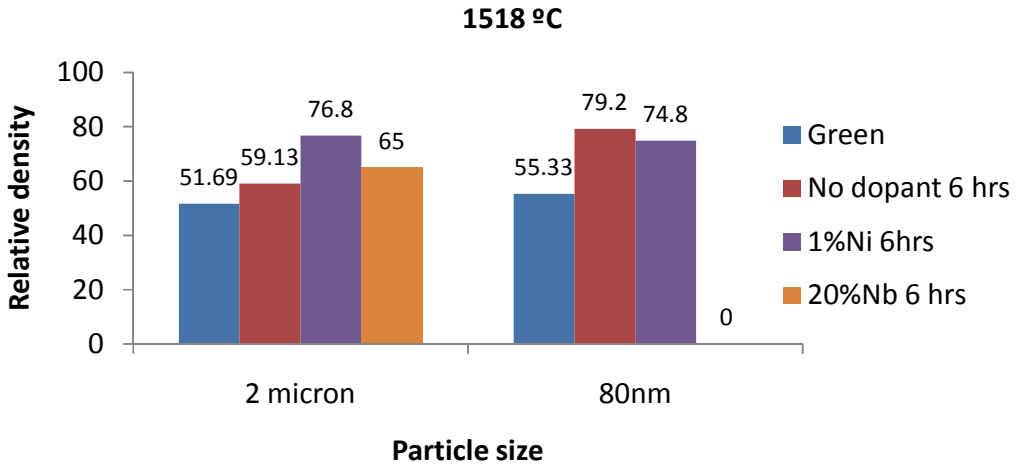


(a)

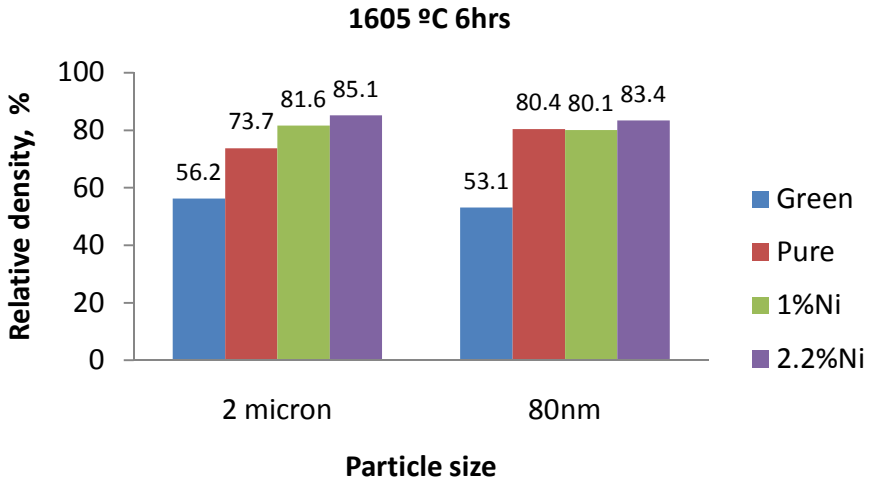


(b)

Figure 8.3 The effect of added dopants on the densification.

In general, Ni appeared to be a more effective sintering aid (Fig. 8.3 (a)), and the densification was enhanced further with a high Ni content or using a higher sintering temperature. The enhanced effects were more pronounced for coarse-grain specimens.

An exception was that addition of 1 at% of Ni reduced the densification for a specimen prepared with 80 nm Mo and sintered at 1518 °C. Liquid-phase sintering may actually occur with 2.2 at % Ni, although the exact phase diagram for Mo-Si-B-Ni system has not been established.

It is known that addition of Nb can significantly improve the plasticity of Mo-Si-B alloy [10]. Apparently, Nb can also improve the sintering rates moderately (Fig. 8.3 (a)). Note that Nb and Mo forms continuous solid solution (while Ni only has very limited solid solubility in Mo).

### 8.3.4 The Effect of Sintering Time

Generally, we adopted 6 hours from ref [8] as the "standard" sintering time. But it is worthy to check if 6 hours is enough and whether longer sintering can boost density higher. Fig. 8.4 shows the effects of sintering time. As a general observation, the further enhancement of densification is not significant after 6 hours. This is presumably due to the inhomogeinity of the specimens, and it may be improved by using a better way to prepare the green specimens. This issue is further discussed in the next section with microstructure analysis.

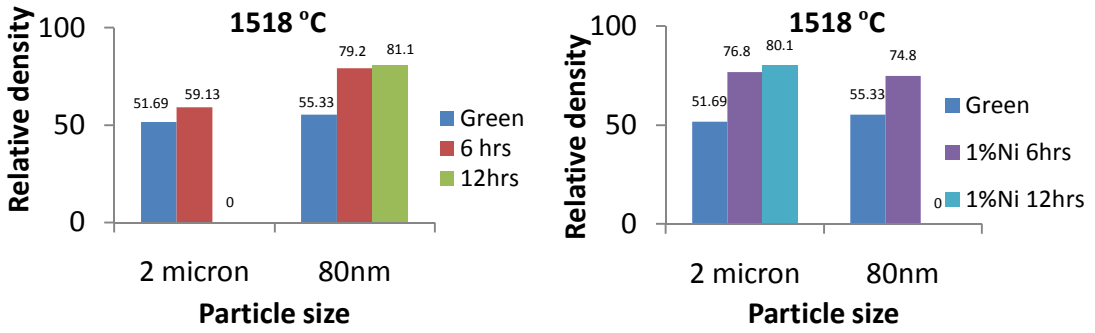


(a) (b)

Figure 8.4 The effects of sintering time on the densification for (a) un-doped and (b) 1 at % Ni doped specimens

### 8.3.5 Effect of $O_2$ Getter

According to Ellingham Diagram, to reduce all the possible oxide formation, Ti and Zr are effective $O_2$ getter. Fig. 8.5 shows equilibrium $O_2$ partial pressure vs. temperature. Ti and Zr lines are under all the other metal/oxide lines.

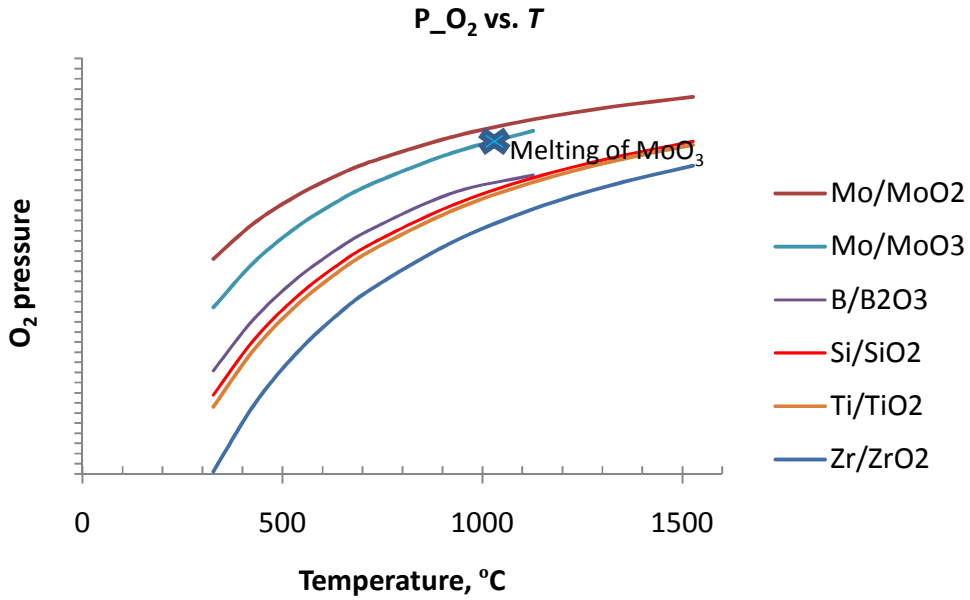


Figure 8.5 Plot of equilibrium $O_2$ partial pressure vs. temperature for different metal/oxide reactions.

As shown in Fig. 8.6, $O_2$ getters don't significantly improve sintering.

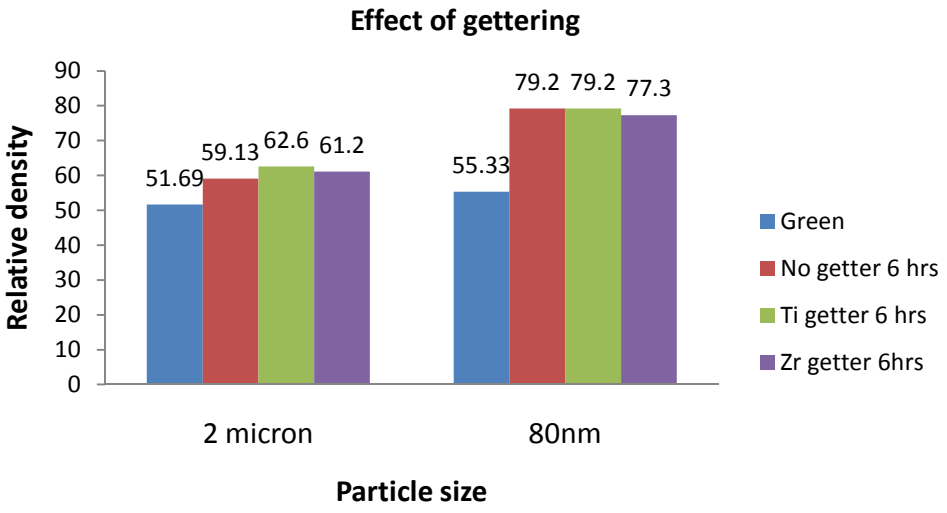


Figure 8.6 The effect of $O_2$ getter on the densification.

### 8.3.6 Microstructures of Sintered Samples

The microstructures of sintered samples were examined by SEM. Three phases can be clearly identified in back-scattering images due to their density difference. In general, the Mo-Si-B samples made out of the 80 nm Mo powder showed finer and more homogeneous structures than those of 2 µm Mo (Fig. 8.7). The 80 nm samples showed smaller Mo grain size (1-2 µm) than 2 µm sample (8-10 µm). However, it is clear that significant grain growth/coarsening occurred in both cases.

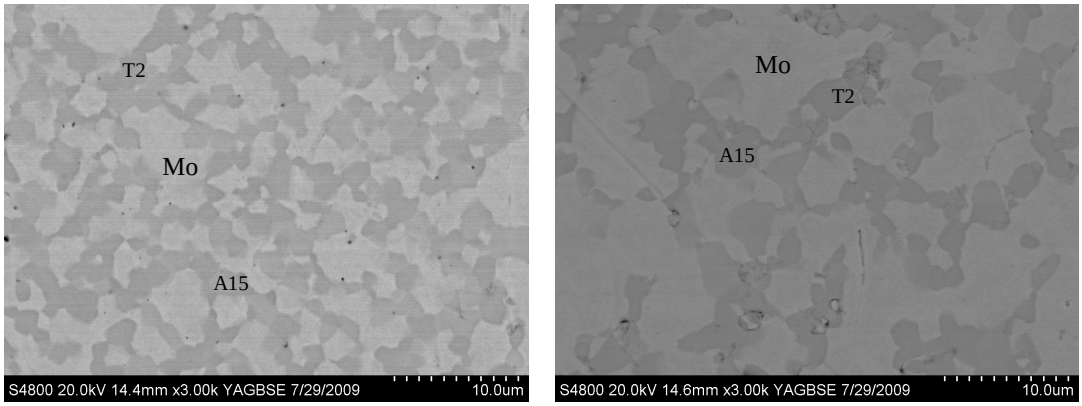


Figure 8.7 SEM images of Mo-Si-B specimens sintered at 1605 ºC for 6 hours, which are made from (a) 80 nm and (b) 2 µm Mo powders. The three phases are labeled.

Significant inhomogeneity is observed for specimens that were made by either 80 nm or 2 µm powders. In either case, there are regions that are almost fully dense (as shown in Fig. 8.7); in the same specimens, there are regions with large pores (as shown in Fig. 8.8). This is presumably due to the inhomegeneity and agglomeration during powder processing and pressing. So far it seems that the powder treatment step is one of the

limiting factors to prevent us from achieving high density. To overcome that, we need to optimize our powder processing and pressing procedure to obtain better green specimens.

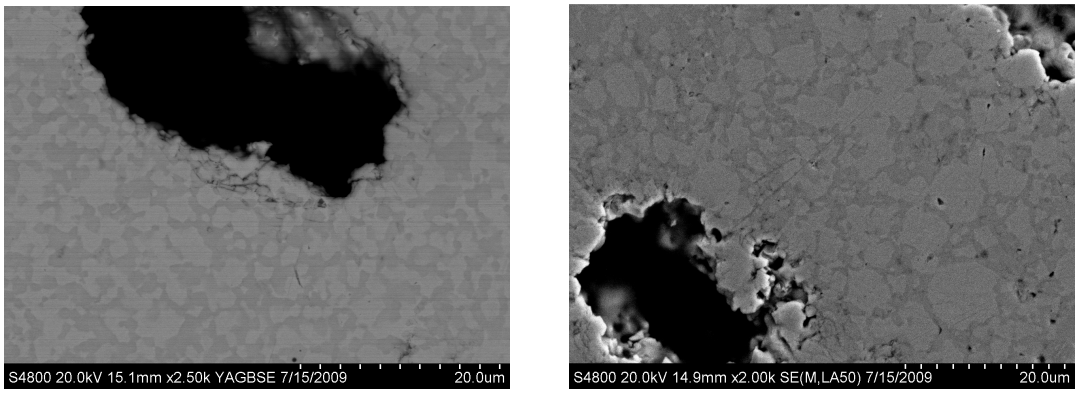


(a) (b)

Figure 8.8 Regions with large pores and inhomogeneity are identified in SEM images of Mo-Si-B samples that were sintered at 1518 ºC for 6 hours using either (a) 80 nm or (b) 2 µm Mo powders.

The introduction of Ni as dopant into Mo-Si-B didn't change the microstructure significantly. The similar three phases were also identified in doped samples. However, EDX analysis showed that all these three phases appear to contain some Ni, though a more careful examination should be carried out to exclude the artifacts due to beam smear. Additionally, some round particles were observed in all the 2.2 at. % Ni doped samples as well as part of 1.0 at. % Ni doped samples, implying the formation of glass/liquid phase. EDX analysis indicated that it contained Si, O and Mo. However, the round particles didn't appear in some 1.0 at. % Ni doped 2 µm Mo samples (Fig. 8.10(c)).Further study may be needed to clarify the nature of this phase.

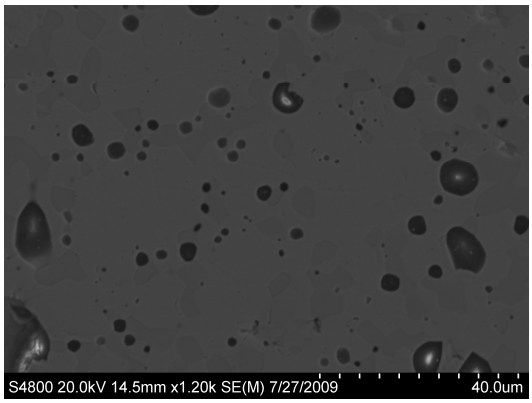


(a)

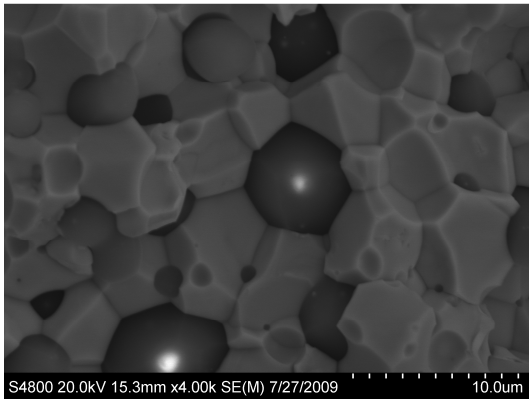


(b)

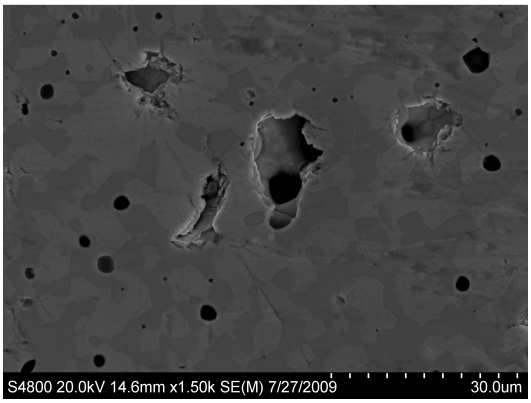


(c)

Figure 8.9 SEM images of 2.2 at % Ni-doped Mo-Si-B samples that were made using (a, b) 80 nm and (c) 2 µm Mo powders by sintering at 1605 ºC for 5 hours. Panel (b) is an observation of a fractured surface, while other specimens are polished.

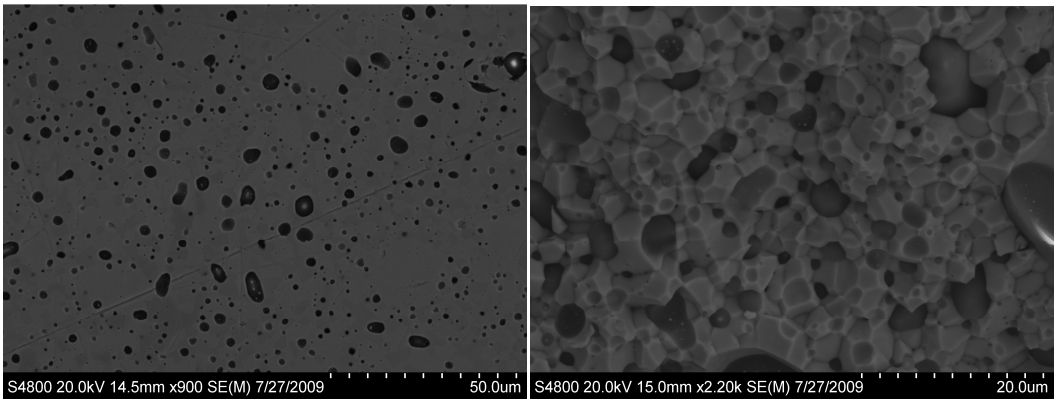


(a) (b)

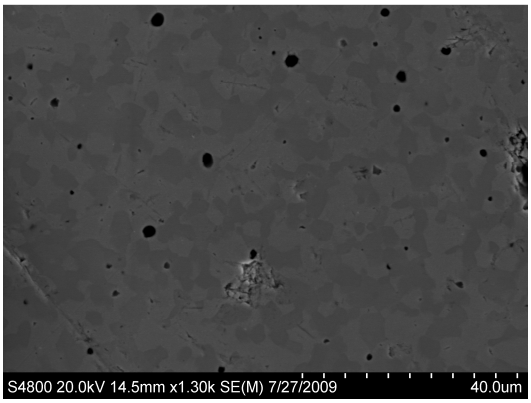


(c)

Figure 8.10 SEM images of 1.0 at % Ni-doped Mo-Si-B samples that were made using (a, b) 80 nm and (c) 2 µm Mo powders by sintering at 1605 ºC for 5 hours. Panel (b) is an observation of a fractured surface, while other specimens are polished. (c) shows no existence of round particle.

## 8.4 Conclusions

- Mo-Si-B can be made by sintering procedure following Middlemas *et al*. method [8]
- Ni is an effective sintering aid for enhancing densification rates in general.

- Fine Mo powder leads to better densification rates.
- However, adding Ni is less effective to enhance densification in specimens with fine powder. It appears to be difficult to achieve > 85% theoretical density with current method. SEM characterization showed almost full-densified regions with large pores, indicating the problem lies in the inhomogeneity in the green specimens.
- To achieve better density, we need to first optimize the processing to make better green specimens.

References

[1] S Majumdar, R Kapoor, S Raveendra, H Sinha, I Samajdar, P Bhargava et al. A study of hot deformation behavior and microstructural characterization of Mo-TZM alloy J.Nucl.Mater. 385 (2009) 545.

[2] M El-Genk, J Tournier. A review of refractory metal alloys and mechanically alloyed-oxide dispersion strengthened steels for space nuclear power systems J.Nucl.Mater. 340 (2005) 93.

[3] IV Gorynin, VA Ignatov, VV Rybin, SA Fabritsiev, VA Kazakov, VP Chakin et al. Effects of neutron irradiation on properties of refractory metals J.Nucl.Mater. 191-94 (1992) 421.

[4] BN Singh, JH Evans, A Horsewell, P Toft, GV Muller. Effects of neutron irradiation on microstructure and deformation behaviour of mono- and polycrystalline molybdenum and its alloys J.Nucl.Mater. 258-263 (1998) 865.

[5] H Kurishita, Y Kitsunai, T Shibayama, H Kayano, Y Hiraoka. Development of Mo alloys with improved resistance to embrittlement by recrystallization and irradiation J.Nucl.Mater. 233-237A (1996) 557.

[6] J Fan, M Lu, H Cheng, J Tian, B Huang. Effect of alloying elements Ti, Zr on the property and microstructure of molybdenum International Journal of Refractory Metals and Hard Materials 27 (2009) 78.

[7] JH Perepezko. The hotter the engine, the better [jet engines] Science 326 (2009) 1068.

[8] MR Middlemas, JK Cochran. Dense, fine-grain Mo-Si-B alloys from nitride-based reactions JOM 60 (2008) 19.

[9] DM Dimiduk, JH Perepezko. Mo-Si-B alloys: Developing a revolutionary turbine-engine material MRS Bull 28 (2003) 639.

[10] P Jehanno, M Heilmaier, H Saage, H Heyse, M Boning, H Kestler et al. Superplasticity of a multiphase refractory Mo-Si-B alloy Scr.Mater. 55 (2006) 525.

# CHAPTER NINE

# CONCLUSIONS

This dissertation study systematically investigated segregation-induced GB disordering in W and Mo based binary alloys through combined experimental and modeling methods. The specific conclusions are summarized as follows.

A quantitative thermodynamic model (with no adjustable parameters) had been built to predict GB disordering in binary W based alloys. This model predicted onset GB disordering temperatures that were coincident with the experimentally observed onset activated sintering temperatures for all five systems: W-Pd, W-Ni, W-Co, W-Fe and W-Cu. In conjunction with a recent HRTEM study, it was concluded that subsolidus activated sintering of doped W was due to short-circuit diffusion in impurity-based premelting-like IGFs (i.e., segregation-induced GB structural disordering). Moreover, this thermodynamic model can have broad applications, *e.g.*, in understanding and controlling creep and liquid metal embrittlement.

For Ni-Mo binary system, both experiments and thermodynamic models showed that δ-NiMo did not wet Mo GBs in the solid state. This clarified a controversy in the literatures where there were repeated claims of solid-state GB wetting in this system. Above the peritectic temperature, the Ni-rich liquid phase does completely wet Mo GBs. Furthermore, HRTEM and Auger electron spectroscopy characterization of well-quenched specimens showed the thermodynamic stabilization of quasi-liquid IGFs in the single-phase region of Ni-doped Mo, where the liquid phase is no longer stable bulk

phase. In this region, the free energy penalty for forming a nanoscale meta-stable liquid film is presumably more than compensated by the reduction in the total interfacial energies upon replacing one GB with two crystal-liquid interfaces.

Furthermore, the thermodynamic model for predicting the stability of subsolidus quasi-liquid IGFs in binary alloys was refined and elaborated. This model employed and modified a Miedema type statistical model to estimate interfacial energies. The free energy of amorphization was assessed by using computational thermodynamics (CalPhaD methods). Then, we defined and quantified thermodynamic variable, $\lambda_L$, to represent the thermodynamic tendency for a GB to disorder. This $\lambda_L$ was defined as the maximum thickness of an undercooked IGF with a uniform composition on the liquidus line or its meta-stable extension. Thereafter, this model was applied to Ni-doped Mo GBs and a "GB diagram" was computed.

Subsequently, GB diffusivities for Ni-doped Mo alloys were obtained by controlled sintering experiments. The correlation between measured GB diffusivities and calculated "GB diagram" validated the proposed thermodynamic model critically. In addition, this correlation re-confirmed that the previously proposed mechanism of solid-state activated sintering, where the increased densification rates was attributed to the enhanced GB transport in the premelting-like IGFs. A preliminary study of sintering Mo-Si-B based alloys has been documented, representing an initial effort to extend this work from binary to multi-component alloys.

Our model for simpler metallic systems may serve as a basis to develop the more complex models for ceramic systems.

This dissertation study, along with a few earlier studies [1,2,3], clearly shows that bulk phase diagrams are not adequate for selecting sintering aids or predicting optimal activated sintering protocols because liquid-like IGFs can form at ~60-85% of bulk solidus temperatures, which results in subsolidus activated sintering with phenomenological similarities to liquid-phase sintering.

This study represents an initial step towards a long-range scientific goal of developing “GB diagrams” as a new materials science tool [4,5]. These “GB diagrams”, as well as more sophisticated (rigorous) GB “phase” or complexion diagrams (to be developed in future studies) [5], can be used to design fabrication pathways to utilize desired GB structures during processing to control microstructural evolution. “Since these impurity-based IGFs can be retained upon cooling and critically affect a variety of mechanical and physical properties, such GB diagrams can be used to devise heat treatment recipes to adjust the final GB structures to improve properties or performance.” Finally, such GB diagrams can forecast various high-temperature materials properties.

References

[1] J Luo, H Wang, Y- Chiang. Origin of Solid State Activated Sintering in Bi2O3-Doped ZnO Journal of the American Ceramic Society 82 (1999) 916.

[2] J Luo, VK Gupta, DH Yoon, HM Meyer. Segregation-Induced Grain Boundary Premelting in Nickel-doped Tungsten Applied Physics Letters 87 (2005) 231902.

[3] VK Gupta, DH Yoon, HM Meyer III, J Luo. Thin Intergranular Films and Solid-State Activated Sintering in Nickel-Doped Tungsten Acta Materialia 55 (2007) 3131.

[4] J Luo. Liquid-like interface complexion: from activated sintering to grain boundary diagrams Current Opinion in Solid State & Materials Science 12 (2008) 81.

[5] SJ Dillon, MP Harmer, J Luo. Grain boundary complexions in ceramics and metals: An overview JOM 61 (2009) 38.